One and two-dimensional propagation of waves in periodic heterogeneous media: transient effects and band-gap tuning

ONE AND TWO-DIMENSIONAL PROPAGATION OF WAVES IN PERIODIC HETEROGENEOUS MEDIA: TRANSIENT EFFECTS AND BAND-GAP TUNING

A thesis submitted to the University of Manchester
for the degree of Doctor of Philosophy
in the Faculty of Engineering and Physical Sciences

2015

Ellis Guy Barnwell
School of Mathematics

Contents

Word count 54416

The University of Manchester

Ellis Guy Barnwell
Doctor of Philosophy
One and two-dimensional propagation of waves in periodic heterogeneous media: transient effects and band-gap tuning
March 19, 2015

In this thesis, the propagation of transient waves in heterogeneous media and the tuning of periodic elastic materials are studied. The behaviour of time harmonic waves in complex media is a well understood phenomenon. The primary aim of this text is to gain a deeper understanding into the propagation of transient waves in periodic media. The secondary aim is to explore the time harmonic behaviour of two dimensional pre-stressed elastic media and investigate the plausibility of band gap tuning.

We begin this text by investigating the reflection of pulses from a semi-infinite set of point masses (we call "beads") on a string. The reflected pulse is formulated using Fourier transforms which involve the harmonic reflection coefficient. We find that the reflected amplitude of a harmonic wave depends on its frequency. We then ask whether it is possible to find an effective reflection coefficient by assuming the beaded portion of the string is given by some effective homogeneous medium. An effective reflection coefficient is found by assuming the homogeneous medium has the wavenumber given by the infinite beaded string. This effective reflection coefficient is compared to the exact reflection coefficient found using the Wiener-Hopf technique.

The results from studying the reflection problem gave inspiration to chapter 4, which focuses on the time dependent forcing of an infinite beaded string that is initially at rest. We again use the Fourier transform to find a time dependent solution. The z transform is then used, after sampling the solution at the bead positions. We impose a sinusoidal loading which is switched on at a specified time. In doing this we are able to explore how the system behaves differently when excited in a stop band, a pass band and at a frequency on the edge between the two.

An exact solution for the infinite beaded string is found at any point in time by expanding the branch points of the solution as a series of poles. We compare this exact solution to the long time asymptotics. The energy input into the system is studied with the results from the exact solution and long time approximation showing agreement. Interesting behaviour is discovered on the two edges between stop and pass bands.

In chapter 5 the effect of a nonlinear elastic pre-stress on the wave band structure of a two dimensional phononic crystal is investigated. In this chapter we restrict ourselves to incompressible materials with the strain energy functions used being the neo-Hookean, Mooney-Rivlin and Fung. The method of small-on-large is used to derive the equation for incremental elastic waves and then the plane wave expansion method is used to find the band structure.

Finally, chapter 6 focuses on the same geometry with a compressible elastic material. The strain energy function used is the one suggested by Levinson and Burgess. We use the theory of small-on-large to derive the incremental equations for coupled small amplitude pressure and shear waves in this material. In both compressible and incompressible materials we show how it is possible to control the stop bands in a material by applying a large elastic pre-stress.

Declaration

No portion of the work referred to in the thesis has been submitted in support of an application for another degree or qualification of this or any other university or other institute of learning.

Copyright Statement

Acknowledgements

I would first like to acknowledge the support which has kindly been given to me by my supervisors William Parnell and David Abrahams. Throughout the course of my PhD they have both been very patient and helpful. They have always remained positive even during hard times. Without their help, completing my PhD would have been an arduous task but, whilst it was difficult, they made it highly enjoyable at the same time.

I would also like to thank all of the members of the waves in complex continua (WICC) group both old and new. With this extremely friendly group of people I have enjoyed many laughs and good times. I hasten to say, it's been WICCed.

Thanks also goes out to all my kind friends and family. Everybody has been very supportive and have always offered to help me out where they can. Particular thanks goes to Alex MacDonald who has been especially understanding and has kept my spirits up over the past years.

Finally, I would like to acknowledge the Leverhulme trust (project grant FA/00 120/CC) for their financial support.

Chapter 1

Introduction

Wave mechanics has been a very rich area of study in mathematics and physics for centuries. Interest in the mathematics of waves can be dated back to Pythagoras, who used mathematics to understand the harmony (or dissonance) experienced when playing different notes on vibrating strings. Since then, the mathematics of waves has arisen in many areas including the study of water and ocean waves, the acoustics of rooms, seismology, structural acoustics, nondestructive testing and quantum mechanics to name but a few.

Waves have been important to us even long before we began studying them. For instance, the pressure waves in the air have allowed us to communicate with each other since well before humans had a concept of the sound wave. In the modern age waves form an integral part of our lives. For example electromagnetic waves are used by our phones to transmit communications, ocean waves are beginning to be used for power generation and sound waves are used to entertain us through music.

The topic of this thesis is the propagation of pulses and waves in heterogeneous media, with a particular focus on waves in materials which exhibit a periodic structure. Interest in waves travelling in periodic structures arose from quantum mechanics. When it was found that electrons act like waves as well as particles, the mechanics of waves was used to explain how they behaved in the periodic electric potential supplied by the protons of a solid. This theory is used to explain the allowed energy bands of electrons in metals and semi-conductors. In other subject areas, a similar theory has been used to model elastic waves in solids, electromagnetic waves in dielectrics and water waves with periodically spaced obstacles.

In the present-day, complex periodic structures are ubiquitous in science and engineering. For instance, over the last two decades the subject of materials science has experienced an increased emphasis on composite materials exhibiting periodic microstructure. Examples of such materials currently in use include fibre reinforced composites, diffraction gratings and laminate materials. Potential future applications include photonic circuits, improved wave guides, active soundproofing and selective wave filtering.

Understanding the wave properties of these materials is key to their design, testing and application. One of the crucial areas to understand is the band gap structure of these materials and how transient waves interact with the periodic geometry. A deeper understanding of the stop and pass band structure allows us to select frequencies for filtering, and guide waves around sharp corners. The ability to tune materials in real time gives the possibility of having dynamic devices, the properties of which can be controlled post production.

1.1 Literature Review

Here we will give a general overview of the relevant literature in the topic of wave mechanics in periodic structures. The list given here is by no means exhaustive; papers that relate to specific areas will be discussed at the beginning of each chapter.

The study of periodic structures goes back many years. Floquet covered the general theory of differential equations with periodic coefficients in his paper in 1883 [18]. Later work was heavily influenced by the study of quantum mechanics and the investigation of electron behaviour in solid state physics. In this case, the structures can be assumed to be almost exactly periodic with a very precise microstructure. The seminal paper by Bloch [6] paved the way for a lot of modern research which has branched into a huge number of different areas of science. In the current day, the study of waves in periodic structures is much more broad and incorporates macroscopic materials [88, 16].

In one dimension the most common quantum mechanical model was developed by Kronig and Penney [45]. This model is influenced by the example of an electron in a crystal lattice. The basis of the Kronig-Penney model is to treat each ion in the crystal lattice as a rectangular potential. In some cases these rectangular potentials

are taken to be vanishingly thin but infinite in magnitude. In this case, the model is directly analogous to the situation of point masses on a string, an application which will be studied in detail in chapters 3 and 4. This analogy has been noted by Griffiths [30] and Oseguera [63].

The reflection of harmonic waves by semi-infinite and finite thickness layered media was considered by Levine [48]. In his work he considers an incoming electromagnetic wave which is scattered by periodically spaced planes. Once again, this geometry is analogous to point masses on a string which was studied recently by Martin [54]. In this paper, Martin looks at finite periodic rows of masses with a defect as well as a perturbation of the masses from their periodic structure. The effective propagation in a perturbed structure was previously studied by Maurel et al. [56]. The problem of reflection and transmission from a finite crystal was also studied by Rorres [73]. In this paper, it was shown how the semi-infinite case is reached by taking an increasingly large crystal.

Periodic structures that exhibit stop and pass band behaviour are typically called photonic crystals in electromagnetism and phononic crystals in elasticity. Modern research efforts into the area of photonic (and subsequently phononic) crystals was inspired by two papers published in 1987. The first by Yablonovitch [96] investigated the problem from a solid-state physics perspective, looking at the band-gaps of electrons in a solid. The second by Sajeev [74] focused on the propagation of photons through a periodic lattice. These two papers have led to a substantial body of research which is still very active today.

Determination of the band-gap structure of heterogeneous periodic media requires advanced mathematical techniques in order to find the dispersion diagrams. There are a number of different techniques that may be used, but one has come to fore due to its computational efficiency and flexibility - the plane-wave expansion method [31]. This method has been used to find band diagrams of periodic structures in many different fields, including acoustics, elasticity and electromagnetism. For example, in elasticity work in the two-dimensional context has been carried out by Sigalas and Economou [81], Kushwaha [47, 46] and Vasseur [85] and in three dimensions by Suzuki [82]. In their book, Joannopolous et al. [37] use the plane-wave expansion method to explore

the practical applications of photonic crystals, laying the pathway to producing photonic circuits. More recently, progress has been made on photonic-phononic crystals [53]. An alternative technique for producing band diagrams is the high-frequency homogenisation approach [3]. This technique is based on finding asymptotic expressions for the wave frequency close to the standing wave modes.

For further reading on the topic of waves, see the book by Graff [28] for a general introduction to waves in solids. The book by Brillouin [8] gives an excellent summary of waves in one-dimensional periodic media. This book explores the stop and pass band structure of periodic systems in detail. Related to the transient problems that will be of interest later, an in-depth discussion of pulse propagation in elastic half spaces and wave guides is given by Miklowitz [57]. A recent modern review of wave propagation in periodic media is given in [22]. In this paper, periodic structures are discussed for electronic, photonic and phononic crystals. These structures are studied both in the spatial and Fourier domains.

Although a significant amount of work has been carried out in the frequency domain (i.e. time-harmonic) very little has been done in the time domain. The work that has been done in the time domain largely consists of computational modelling, lacking the insight that analytical methods can offer.

Through the course of this thesis, we develop the necessary mathematical tools to study periodic problems in the time domain. We derive both exact and approximate reflection coefficients from a semi-infinite array of point masses and highlight the problems associated with homogenisation techniques. For an infinite array of point masses we derive the general solution for a prescribed transient force acting on a single bead. Both the short and long-time behaviour is explored and new results on the energy input into periodic systems are presented.

With regards to periodic band-gap materials, these are usually considered as being static devices. They may be designed and built to exhibit certain properties that remain unchanged after construction. As discussed in the later chapters, recent work has started to focus on the active tuning of band-gap devices, altering the properties of materials in real time. Of this work only a handful of studies have considered the effect of elastic deformation.

In this thesis we consider a form of deformation not previously studied for the

application of tunable band-gap structures. We derive the governing equation for the coupled pressure and shear wave mode in a pre-stressed composite material. For a number of strain energy functions we study the dispersion diagram of this novel structure for different modes of propagation. The possibility of stop-band tuning via application of elastic pre-stress is explored. The results presented show a lot of potential for creating tunable elastic band-gap structures.

1.2 Thesis structure

In the first part of this thesis, we aim to study the transient behaviour of waves in periodic media. The key questions we wish to answer in this area are

- can we represent a semi-infinite heterogeneous medium by a semi-infinite homogeneous effective medium?
- can this effective medium be used to reconstruct reflected pulses?
- what happens when we excite waves in an infinite periodic medium at particular frequencies?
- when we force a system at a frequency that is in a stop band, does the solution grow indefinitely?

In the second part of this thesis we focus on the effect of nonlinear elastic pre-stress on the band structure of two-dimensional periodic elastic materials. The questions we aim to answer in these chapters are

- how is the band structure of a material affected by applying an elastic pre-stress?
- is it practically possible to switch stop bands on and off by applying an elastic pre-stress?

The structure of this thesis will be as follows. In chapter 2 we cover the background material. This is all well known material that will set the scene for the subsequent chapters and supply us with the necessary tools. For waves on strings we cover d'Alembert's solution to the wave equation, reflection from density discontinuities and derive the dispersion relation for an infinite string with periodically spaced

point masses. We then introduce wave propagation in two-dimensional elastic media, including an introduction to the plane-wave expansion method and the derivation of the band diagram. Finally, we give a very brief overview of the important aspects of nonlinear elasticity and the theory of small-on-large, a theory used later in the thesis to study the band-gaps of pre-stressed media.

In chapter 3 we study the problem of a prescribed incoming pulse reflected from a semi-infinite array of point masses on an infinite string. The masses will be spaced periodically on one half of the string. The motivation for studying this geometry is the fact that in the time-harmonic case the reflection coefficient can be found exactly. In this chapter we find an effective reflection coefficient and compare this to the exact one.

We follow on from chapter 3 with the study of transient excitation of an infinite array of point masses on a string in chapter 4. For this geometry, the dispersion relation for harmonic waves is known exactly. A sinusoidal forcing that is switched on at a specified time is imposed on one of the masses. We study forcing frequencies which are in stop and pass bands to see how the system behaves differently.

We begin our study of tunable stop bands in chapter 5 by considering an incompressible nonlinearly elastic pre-stressed medium. The two-dimensional structure will be made up of a periodic array of pre-stressed cylinders embedded in a host. The theory of small-on-large is used to find the governing equation for linear waves superposed on top of the nonlinear pre-stress. In this chapter we restrict our study to waves that are polarised along the axes of the cylinders. We refer to this as the SH mode. We investigate the tuning of the band diagrams and the switching on and off of stop bands.

Finally, in chapter 6 we extend the tunable stop band work to compressible materials. A numerical solution to the initial finite deformation is obtained. Once again, the small-on-large theory is used to find the incremental equation for linear waves. In this chapter we derive the governing equations for coupled pressure and shear waves that are polarised in the plane perpendicular to the cylinder axes. We refer to this as the P-SV mode. We explore the tunability of band diagrams for both the SH mode and the coupled P-SV modes. Finally, in chapter 7 we conclude by summarising the key results and discussing areas for further research.

Chapter 2

Background

In this chapter, we aim to cover all of the basic background knowledge that is necessary to understand the following chapters of this thesis. Clearly it is not possible to cover everything so references to instructive texts have been given where necessary. The subject of wave mechanics spans a number of different fields of study. These include acoustics, electromagnetism, fluid dynamics, elasticity and quantum mechanics. For the purpose of this thesis, primarily for ease of exposition, we have chosen to study waves in the context of strings of changing density in one-dimension and elastic solids in two-dimensions. The majority of the ideas presented are transferable to different disciplines, usually in a straightforward manner.

2.1 Waves on strings

We begin our exploration of wave mechanics with the humble example of waves on a string. The equations outlined here will be used in chapters 3 and 4 when discussing periodic one-dimensional heterogeneous media. We commence by deriving the wave equation on a string and then move on to discuss the reflection from boundaries and point masses. We end this discussion by deriving the wavenumber for a string with periodically spaced point masses.

In order to derive the equation for the string, we look at the forces acting on an infinitesimal element of string as pictured in figure 2.1. For the time being, we assume that the string is of infinite extent and homogeneous, in order to avoid any end effects. The string is kept taught and maintained at a constant tension τ. The density per

unit length of the string will be given by ρ_0 and the displacement of the string from the equilibrium position is given by $u(x,t)$.

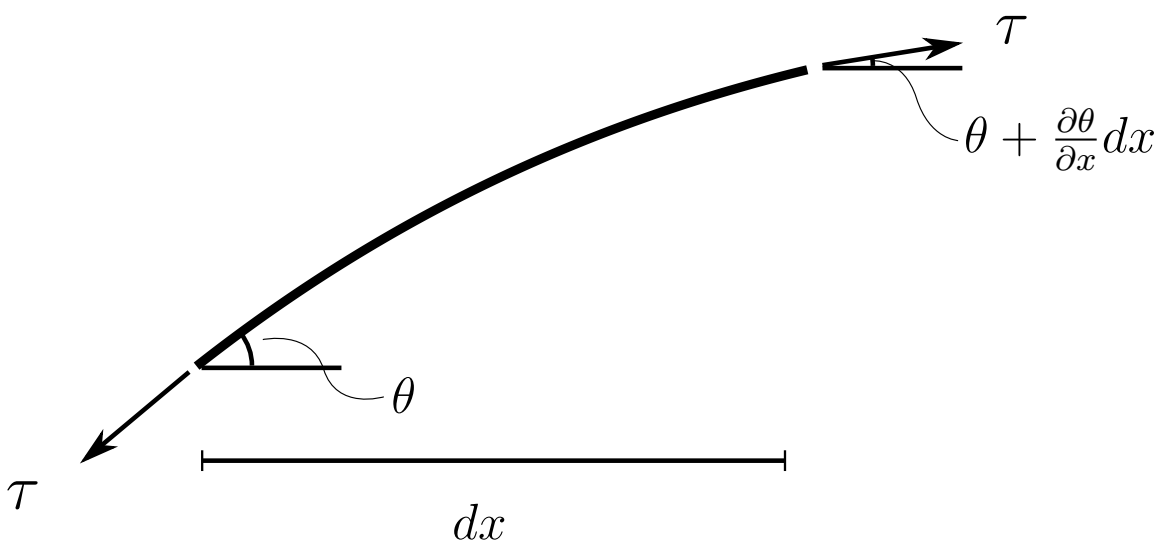

Figure 2.1: A string segment of length dx where the string tension, τ, is pulling equally in opposite directions

The force acting vertically upward on the string element due to the tension in the string at both ends is given by

$$dF = \tau \sin\left(\theta + \frac{\partial\theta}{\partial x}dx\right) - \tau\sin(\theta).$$

By assuming that the slope of the string never gets too steep, we can use the small angle approximation that $\sin(\theta) \approx \theta$ for $\theta \ll 1$ to give

$$dF = \tau\left(\theta + \frac{\partial\theta}{\partial x}dx - \theta\right) = \tau\frac{\partial\theta}{\partial x}dx. \tag{2.1}$$

We can approximate the angle of the string element by noting that

$$\theta \approx \tan(\theta) = \frac{\partial u}{\partial x}. \tag{2.2}$$

This gives the upward force on the string element to be

$$dF = \tau\frac{\partial^2 u}{\partial x^2}dx. \tag{2.3}$$

We now apply Newton's second law to the string element of mass $\rho_0\,dx$ to get

$$\tau\frac{\partial^2 u}{\partial x^2} = \rho_0\frac{\partial^2 u}{\partial t^2}, \tag{2.4}$$

where ρ_0 is the density, i.e. mass per unit length of string. Defining the wave speed of the string to be $c_0 = \sqrt{\tau/\rho_0}$, we obtain the familiar form of the linear wave equation

$$c_0^2\frac{\partial^2 u}{\partial x^2} = \frac{\partial^2 u}{\partial t^2}. \tag{2.5}$$

It can easily be shown that a travelling wave solution to this equation is

$$u(x,t) = \Re(e^{i(kx-\omega t)}), \tag{2.6}$$

where $k = 2\pi/\lambda$ is the wavenumber and is related to the reciprocal of the wavelength, λ. The angular frequency of the wave is given by ω and is related to the reciprocal of the time period. The $\Re$ symbol implies that we are taking the real part of the exponential in order to get a physical solution. For notational convenience, it will be implied from now on that when we write a wave in exponential form without this symbol, we will subsequently take the real part. Also, by convention, we shall always take a negative exponent in time ($e^{-i\omega t}$) in this thesis. In the case of an infinite string, k and ω can take any value, provided the following relation holds

$$c_0 = \frac{\omega}{k}. \tag{2.7}$$

The value c_0 is known as the phase speed and tells us how fast a peak (or trough) of the wave will travel along the string. In this example it is a constant dependent only on the material properties.

2.1.1 Nondimensionalisation

At this point, we choose to introduce a nondimensionalisation scheme that will be followed throughout the thesis. We will scale the spatial variable on some characteristic length dependent on the problem at hand, ℓ, and the time on ℓ/c_0 (the time taken to travel the distance ℓ). Introducing these nondimensional variables with the use of hats, we have

$$\hat{x} = \frac{x}{\ell}, \qquad \hat{t} = \frac{c_0}{\ell}t. \tag{2.8}$$

Applying this nondimensionalisation to the wave equation (2.5), we get

$$\frac{\partial^2 u}{\partial \hat{x}^2} = \frac{\partial^2 u}{\partial \hat{t}^2}. \tag{2.9}$$

The travelling wave solution, (2.6), becomes

$$u(\hat{x}, \hat{t}) = e^{i\left(k\ell\hat{x} - \frac{\omega\ell}{c_0}\hat{t}\right)}. \tag{2.10}$$

We define a new parameter ϵ to be

$$\epsilon = k\ell = \frac{2\pi\ell}{\lambda} = \frac{\omega\ell}{c_0}. \tag{2.11}$$

The parameter ϵ can be thought of as either the nondimensional frequency or wavenumber. During this text we usually relate ϵ to time so we refer to it as the nondimensional frequency.

The travelling wave solution now has the form

$$u(\hat{x}, \hat{t}) = e^{i\epsilon(\hat{x} - \hat{t})}. \tag{2.12}$$

In general, the choice of ℓ will depend on the specific problem at hand. When we are considering periodic problems, ℓ will normally be chosen as the period of the system. For the case of a wave travelling on an infinite string, it is convenient to choose $\ell = \lambda/2\pi$, giving $\epsilon = 1$ and the travelling wave solution to be

$$u(\hat{x}, \hat{t}) = e^{i(\hat{x} - \hat{t})}. \tag{2.13}$$

From now on, we will drop the hats on nondimensional variables, but the relations given here still hold.

2.1.2 Integral and series transforms

We will now define the conventions adopted for the transforms used later in this thesis. By far the most commonly used transform in wave mechanics is the Fourier transform. In terms of the nondimensional parameters introduced above, the Fourier transform is given by

$$\hat{u}(\epsilon) = \int_{-\infty}^{\infty} u(x) e^{i\epsilon x} dx, \tag{2.14}$$

and the inverse transform by

$$u(x) = \frac{1}{2\pi} \int_{-\infty}^{\infty} u(\epsilon) e^{-i\epsilon x} d\epsilon. \tag{2.15}$$

We also make use of the z transform, which is essentially a Fourier transform applied to discrete systems. The z transform of a discrete function $u(m)$ (for $m \in \mathbb{Z}$) is defined as [38]

$$v(z) = \sum_{m=-\infty}^{\infty} z^m u(m) \tag{2.16}$$

and its inverse by

$$u(p) = \frac{1}{2\pi i} \oint_C v(z) z^{-p-1} dz. \tag{2.17}$$

2.1.3 D'Alembert's solution

The general solution to the wave equation is d'Alembert's solution. This solution gives travelling pulses of any shape and as we will see, is very useful in building solutions to problems involving heterogeneous media of finite size. To derive d'Alembert's solution, we first factorise the operator in the wave equation given by (2.9) as

$$\left(\frac{\partial}{\partial x} - \frac{\partial}{\partial t}\right)\left(\frac{\partial}{\partial x} + \frac{\partial}{\partial t}\right) u(x,t) = 0. \tag{2.18}$$

This leads naturally to the change of variables

$$\mu = x - t\ , \quad \eta = x + t. \tag{2.19}$$

The reason behind this choice becomes clear when we consider the derivatives of the new variables. For μ we have

$$\begin{aligned} \frac{\partial}{\partial \mu} &= \frac{\partial x}{\partial \mu}\frac{\partial}{\partial x} + \frac{\partial t}{\partial \mu}\frac{\partial}{\partial t} \\ &= \frac{1}{2}\left(\frac{\partial}{\partial x} - \frac{\partial}{\partial t}\right). \end{aligned} \tag{2.20}$$

and for η we have

$$\frac{\partial}{\partial \eta} = \frac{1}{2}\left(\frac{\partial}{\partial x} + \frac{\partial}{\partial t}\right). \tag{2.21}$$

After this change of variables, the wave equation becomes

$$\frac{\partial^2 u}{\partial \mu \partial \eta} = 0. \tag{2.22}$$

The general solution to this is quite clearly

$$u(\mu, \eta) = f(\mu) + g(\eta), \tag{2.23}$$

where $f(\mu)$ and $g(\eta)$ are arbitrary functions, which give the displacement of the string at a given point in space and time.

Substituting (2.19) into the solution we get

$$u(x,t) = f(x-t) + g(x+t). \tag{2.24}$$

This is a standard and well recognised result: $f(x-t)$ and $g(x+t)$ represent two moving signals travelling in the positive and negative x directions respectively. These disturbances travel without modification in shape, they are simply translated in space as time passes. This is to be expected since the classical wave equation (2.9) is nondispersive implying that all frequencies travel at the same speed. The form of this solution tells us that we can choose any disturbance travelling to the left or right and it will satisfy the wave equation provided it does not change its shape.

In general, the forms of $f(x-t)$ and $g(x+t)$ are dictated by the initial conditions. If we want to specify the disturbances it is possible to set the initial displacement and velocity of the string to give these functions whatever form that we choose. For further reading in this area, see [5] and [10].

Implementation of initial conditions

In order to give $f(x-t)$ and $g(x+t)$ specific forms for a string initially at rest we must impose the initial displacement and velocity of the string. These initial conditions are given by

$$u(x,t)\big|_{t=0} = u_0(x), \quad \text{and} \quad \left.\frac{\partial u(x,t)}{\partial t}\right|_{t=0} = v_0(x), \tag{2.25}$$

where $u_0(x)$ and $v_0(x)$ are prescribed functions. We now substitute the solution (2.24) into these initial conditions to give

$$f(x) + g(x) = u_0(x) \tag{2.26}$$

and

$$-f'(x) + g'(x) = v_0(x). \tag{2.27}$$

We integrate (2.27) from 0 to x, giving

$$-f(x) + g(x) = \int_0^x v_0(\xi)\, d\xi. \tag{2.28}$$

Solving equations (2.26) and (2.28) simultaneously gives

$$\begin{aligned} f(x) &= \frac{u_0(x)}{2} - \frac{1}{2}\int_0^x v_0(\xi)\ d\xi, \\ f(x-t) &= \frac{u_0(x-t)}{2} - \frac{1}{2}\int_0^{x-t} v_0(\xi)\ d\xi \\ &= \frac{u_0(x-t)}{2} + \frac{1}{2}\int_{x-t}^0 v_0(\xi)\ d\xi \end{aligned} \tag{2.29}$$

and

$$\begin{aligned} g(x) &= \frac{u_0(x)}{2} + \frac{1}{2}\int_0^x v_0(\xi)\ d\xi, \\ g(x+t) &= \frac{u_0(x+t)}{2} + \frac{1}{2}\int_0^{x+t} v_0(\xi)\ d\xi. \end{aligned} \tag{2.30}$$

The final solution is therefore

$$u(x,t) = \frac{u_0(x-t)}{2} + \frac{u_0(x+t)}{2} + \frac{1}{2}\int_{x-t}^{x+t} v_0(\xi)\ d\xi. \tag{2.31}$$

Note that we are able to get a wave travelling in just one direction by careful choice of the initial conditions. If we desire to only have a right-travelling wave, we set $g(x) = 0$ which, from (2.30), gives the restriction that

$$u_0(x) = -\int_0^x v_0(\xi)d\xi. \tag{2.32}$$

Our solely right-travelling wave is thus given by

$$f(x) = u_0(x) = -\int_0^x v_0(\xi)d\xi. \tag{2.33}$$

Equally, we can obtain a purely left-travelling wave by imposing $f(x) = 0$ which gives

$$u_0(x) = \int_0^x v_0(\xi)d\xi. \tag{2.34}$$

2.1.4 Reflection and transmission from boundaries

We now consider what happens when a disturbance travelling along a string hits an interface with a different density of string. This situation, which is depicted in figure 2.2, signals the start of our discussion of heterogeneous media. On the left-hand side, the string has density ρ_0 and wavespeed c_0. On the right-hand side, the string has density ρ_1 and wavespeed c_1. We will impose an incoming wave from the left, given by $u_0(x) = f_{\text{In}}(x)$. We then determine the reflected and transmitted signals. This is

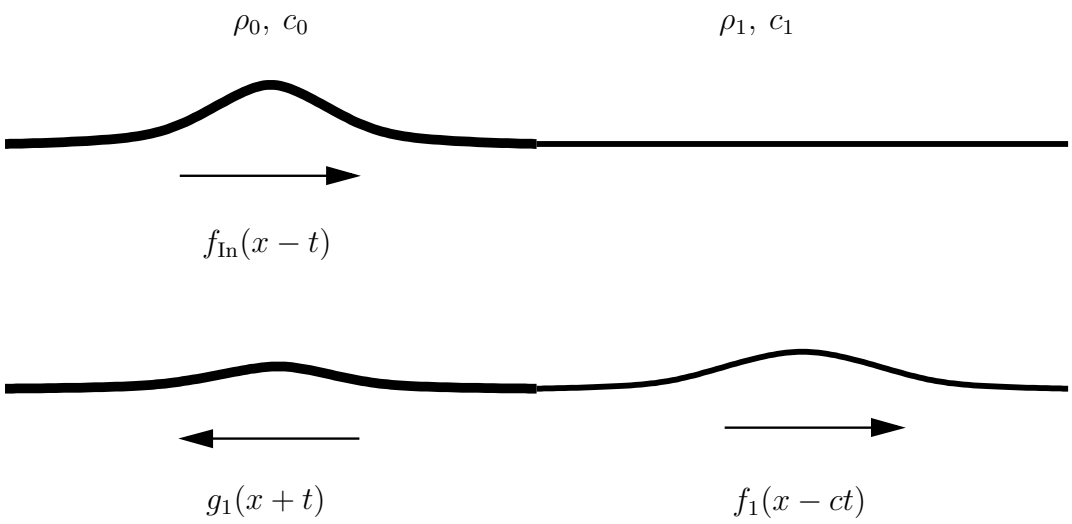

Figure 2.2: Reflection and transmission of a pulse at an interface between two different densities of string. We have nondimensionalised using the wave speed in the left half of the string. The ratio of the wave speeds is given by $c = c_1/c_0$.

done by imposing the condition that the displacement, $u(x,t)$, and the vertical force are continuous across the boundary.

By applying the same scaling as before, given by equation (2.8), the nondimensional wave equation in the right half of string is

$$c^2\frac{\partial^2 u}{\partial x^2} = \frac{\partial^2 u}{\partial t^2}, \tag{2.35}$$

where $c = c_1/c_0$ is the ratio of the wavespeeds in the two halves of the string. Following a similar procedure to section 2.1.3 we can show that the solution in the right half of the string is given by

$$u_+(x,t) = f(x-ct) + g(x+ct). \tag{2.36}$$

We know from (2.24) that the displacement in the left-hand side of the string is given by

$$u_-(x,t) = f(x-t) + g(x+t). \tag{2.37}$$

To these two solutions, we impose the condition that, apart from the prescribed input, we only have outgoing waves, giving

$$u_+(x,t) = f_1(x-ct), \tag{2.38}$$

$$u_-(x,t) = f_{\text{In}}(x-t) + g_1(x+t). \tag{2.39}$$

The boundary condition of continuity of displacement is given by

$$u_-(x,t)|_{x=0} = u_+(x,t)|_{x=0}. \tag{2.40}$$

Given that we assume the vertical force is proportional to the slope of the string, the force continuity condition translates to

$$\left.\frac{\partial u_-(x,t)}{\partial x}\right|_{x=0} = \left.\frac{\partial u_+(x,t)}{\partial x}\right|_{x=0}. \tag{2.41}$$

Applying these conditions to the two solutions, (2.38) and (2.39), we get

$$f_{\text{In}}(-t) + g_1(t) = f_1(-ct), \tag{2.42}$$

$$f'_{\text{In}}(-t) + g'_1(t) = f'_1(-ct), \tag{2.43}$$

We now integrate the second condition with respect to time which gives

$$-f_{\text{In}}(-t) + g_1(t) = -\frac{1}{c}f_1(-ct) + C. \tag{2.44}$$

We set $C = 0$ since at $x = 0, t = 0$ we can safely assume that $f_{\text{In}}(0) = g_1(0) = f_1(0) = 0$ (this simply states that initially the prescribed incoming pulse has zero displacement at the origin).

We can solve the pair of equations, (2.42) and (2.44), to find the reflected and transmitted pulses to be

$$g_1(t) = \frac{c-1}{c+1}f_{\text{In}}(-t),$$
$$f_1(t) = \frac{2c}{c+1}f_{\text{In}}\left(\frac{t}{c}\right).$$

Since this is true for all values of x and t, we can replace the argument by either $x+t$ or $x-ct$ as appropriate, giving

$$g_1(x+t) = \frac{c-1}{c+1}f_{\text{In}}(-(x+t)),$$
$$f_1(x-ct) = \frac{2c}{c+1}f_{\text{In}}(x/c-t).$$

These equations state that the transmitted and reflected waves have the same form as the prescribed incoming wave. The change in argument of f_{In} causes the reflection of the pulse in the case of g_1 and the widening or shortening of the pulse given by f_1. We define the reflection and transmission coefficients when going from phase 0 to 1 as

$$R_{01} = \frac{c-1}{c+1},$$
$$T_{01} = \frac{2c}{c+1}. \tag{2.45}$$

These reflection and transmission coefficients are the same as if we set the problem up with harmonic waves. What is interesting to note is that when $c < 1$ ($c_0 > c_1$), R is negative and the reflected wave exhibits negative displacement. This corresponds to a pulse hitting a portion of heavier string. As we take the string to be heavier, the limiting case is that of a string that is pinned at the discontinuity. In this case, the pulse has the same amplitude as the input but is simply flipped.

We can go one step further, and place multiple boundaries on the string. The situation in figure 2.3 shows three regions of different density. In this case, we have the wave transmitted from the first boundary being reflected inside the strip an infinite number of times. Each time it reflects, a small portion of its energy will radiate outward, but there will always remain a finite amount of energy reflected in that portion of string. In reality, dissipation due to heat for example will eventually dampen the wave.

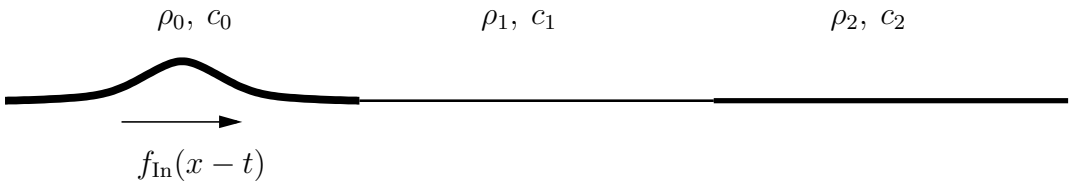

Figure 2.3: Three separate sections of string with different properties.

We can solve this problem by matching the boundary conditions on both boundaries in the same way as the single one. Reflection and transmission coefficients from phase 1 to 2 can clearly be obtained in a similar manner to R_{01} and T_{01}, and are given by

$$R_{12} = \frac{c_2 - c_1}{c_2 + c_1}, \tag{2.46}$$

$$T_{12} = \frac{2c_2}{c_2 + c_1}. \tag{2.47}$$

The solution for a pulse hitting a strip is visualised in figure 2.4 at various points in time. We can see that the initial pulse travels through without any effect other than a reduction in amplitude. A portion of the pulse bounces back and forth inside the strip being trapped in between the two interfaces. This portion supplies a train of pulses in both the positive and negative x directions. Since each phase is nondispersive, all of these pulses have the same shape as the input but have lower amplitude. It is also

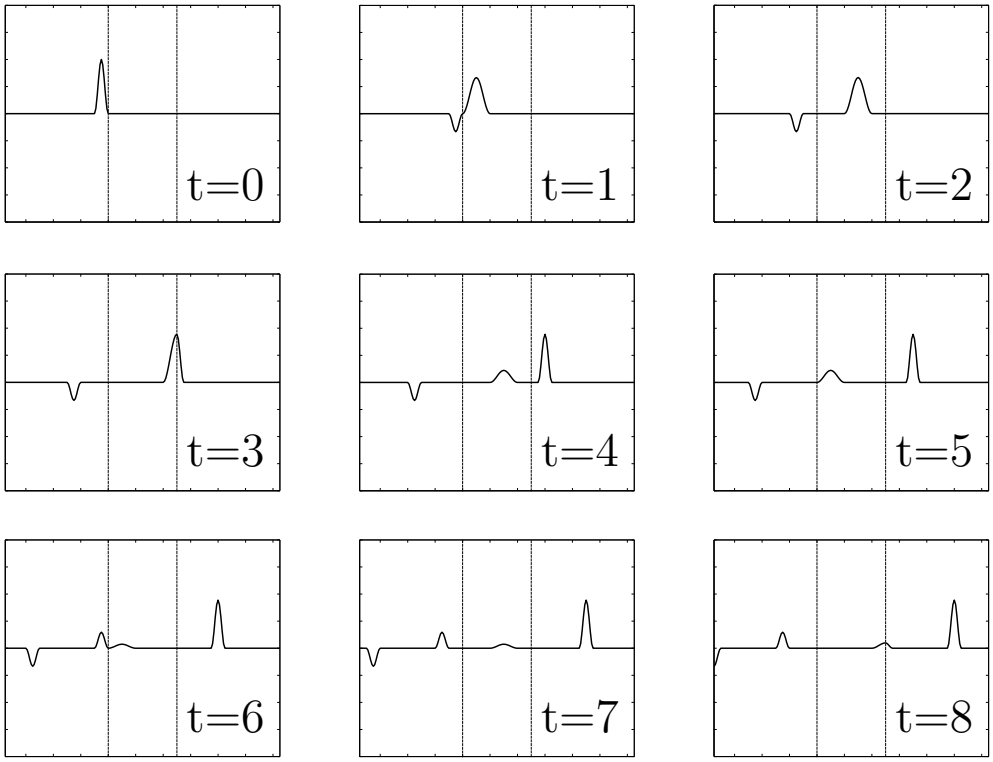

Figure 2.4: A pulse travelling through a strip. The wave speed in the first and last sections of the string are $c_0 = c_2 = 1$ and the wave speed in the middle section is $c_1 = 2$. Part of the pulse is trapped in the strip as it rebounds between the two interfaces.

interesting to note that the pulse in the strip is wider. This is because the wavespeed is greater here than it is in the host phase.

We may extend this method to as many layers as we like. Each time we add another layer, we simply have another interface that will reflect and transmit. By adding up this scattering, we can find the exact solution of a pulse travelling through a layered composite. The downside of this method is that as we add more layers, the amount of computing power required grows rapidly. Having said that, this method can be extremely useful for comparison with approximate solutions in regions where we have enough layers to make the approximate solutions valid, but not too many so that the exact solution can be found in a reasonable amount of time.

This method has been discussed in the book by Fouque et al. [19]. In considering a multilayer slab, they find what are called the propagator and scattering matrices. This approach offers a convenient way to deal with modelling wave propagation in layered media with a large number of layers, without having to determine the exact

fields within the layers.

2.1.5 Reflection and transmission from a point mass

We will briefly cover the case of reflection and transmission from a single point mass, which we refer to as a "bead". The single bead problem leads on to later sections, which involve an infinite number of beads. We will assume a travelling wave solution and look purely at the spatial variation to the left and right of the bead. Our bead will be placed at position $x = 1$ (due to our scaling, this relates to a bead at a general position ℓ).

To find the reflection and transmission coefficients from the bead, we will apply the conditions of continuity of displacement and continuity of force. Displacement continuity is given by

$$u^-(x,t)|_{x=1} = u^+(x,t)|_{x=1}, \tag{2.48}$$

where the $u^-(x,t)$ is the solution for $x < 1$ and $u^+(x,t)$ is the solution for $x > 1$. Imposing force balance across the bead, we equate the difference in slope to the force exerted on the bead due to Newton's law. In other words, we have

$$\left.\frac{\partial u^+(x,t)}{\partial x}\right|_{x=1} - \left.\frac{\partial u^-(x,t)}{\partial x}\right|_{x=1} = M\left.\frac{\partial^2 u(x,t)}{\partial t^2}\right|_{x=1}, \tag{2.49}$$

where $M = m/\rho_0\ell$ is the nondimensional bead mass, scaled on the mass of the section of string between the origin and bead position.

In order to find the reflection and transmission coefficients, we set the incoming wave amplitude to unity and the outgoing amplitudes to R and T for the reflected and transmitted waves. In this case, our ansatz is

$$u^-(x,t) = e^{i\epsilon(x-t)} + Re^{-i\epsilon(x+t)}, \tag{2.50}$$

$$u^+(x,t) = Te^{i\epsilon(x-t)}. \tag{2.51}$$

If we so wish, we can construct solutions for many beads by extending this definition to include a separate ansatz in each section of the string separated by beads. The rest of the analysis works in much the same way.

Using the ansatz given in (2.50) and (2.51) in the condition of displacement continuity at $x = 1$ gives

$$e^{i\epsilon} + Re^{-i\epsilon} = Te^{i\epsilon}. \tag{2.52}$$

Doing the same for the force continuity gives

$$Te^{i\epsilon} - e^{i\epsilon} + Re^{-i\epsilon} = iM\epsilon Te^{i\epsilon}. \tag{2.53}$$

These two equations may be solved to get the reflection and transmission coefficients

$$R = \frac{iM\,\epsilon\, e^{2i\epsilon}}{2 - iM\epsilon}, \tag{2.54}$$

$$T = \frac{2}{2 - iM\epsilon}. \tag{2.55}$$

There are two interesting facts to note. Firstly, the reflection and transmission coefficients are complex numbers. When written in polar form we have

$$R = |R|e^{i\phi_R}, \tag{2.56}$$

$$T = |T|e^{i\phi_T}, \tag{2.57}$$

where ϕ_R and ϕ_T are the arguments of the complex reflection and transmission coefficients. It is clear that the complex part of the coefficients cause a phase shift in the solution. This comes from the fact that (unlike with density discontinuities), we no longer have continuity of slope at the discontinuity point. The slope either side of the bead will be whatever is required to keep the force balanced. This causes the observed phase shift.

The second interesting point to note is that these coefficients depend on the chosen frequency of oscillation ϵ. For low frequency waves (corresponding to long wavelengths) $|R| \to 0$ and $|T| \to 1$, implying that the wave travels through the bead as if it were not there. For high-frequency waves (corresponding to short wavelengths) $|R| \to 1$ and $|T| \to 0$, implying that all of the wave is reflected back from the bead as if the string were pinned at this point. We can make sense of this by thinking about the acceleration of the bead. For low frequencies, the acceleration of the bead is very low, and there is very little resistive force from its motion. For higher frequencies, the acceleration of the bead is much greater, implying that there is more inertial force required and the bead acts almost like a solid boundary.

2.2 Bloch waves in periodic media

Thus far we have considered isolated inhomogeneities. It is common to use ordered inhomogeneities in order to guide waves in specific ways. Often this ordering consists

of periodic spacing of the inhomogeneities.

We now consider a periodic system with an infinite number of beads spaced evenly along a string. This section will give us insight into how waves behave in periodic heterogeneous media. We use the ideas first discussed by Bloch [6] in the field of quantum mechanics. We will not give too much detail here, but instead refer the reader to the notes of Abrahams [1].

In order to add an isolated mass onto the string, we alter the density in the wave equation. For example, to add a bead with nondimensional mass M at the origin, the wave equation becomes

$$\frac{\partial^2 u}{\partial x^2} = (1 + M\,\delta(x))\,\frac{\partial^2 u}{\partial t^2}, \tag{2.58}$$

where $\delta(x)$ is the Dirac delta function, given for example by the limit

$$\delta(x) = \lim_{a\to 0} \frac{1}{a\sqrt{\pi}} e^{-x^2/a^2}. \tag{2.59}$$

The Dirac delta function exhibits the property that the area underneath the curve is equal to one, or more formally

$$\int_{0-\eta}^{0+\eta} \delta(x)dx = 1. \tag{2.60}$$

By integrating equation (2.58) over a vanishingly small region $x \in (0-\eta, 0+\eta)$ for $\eta \to 0$ we find the jump condition over the bead, given by

$$\left.\frac{\partial u}{\partial x}\right|_{x=\eta} - \left.\frac{\partial u}{\partial x}\right|_{x=-\eta} = M\frac{\partial^2 u}{\partial t^2}. \tag{2.61}$$

This is in agreement with the force balance given in equation (2.49), which was constructed on physical grounds. Using this jump condition and considering a time-harmonic wave, such that $u(x,t) = U(x)e^{-i\epsilon t}$, we find the Green's function associated with (2.58) to be

$$U(x) = \frac{iM\epsilon}{2}\,U(0)\,e^{i\epsilon|x|}. \tag{2.62}$$

This is found by taking the Fourier transform of (2.58) and ensuring that waves are outgoing at infinity.

For an infinite number of masses spaced periodically a distance of unity apart (i.e. a distance ℓ apart in dimensional coordinates, see (2.8)) we simply add the contribution from the additional masses onto the right-hand side of (2.58), giving

$$\frac{\partial^2 u}{\partial x^2} = \left(1 + M\sum_{n=-\infty}^{\infty} \delta(x-n)\right)\frac{\partial^2 u}{\partial t^2}. \tag{2.63}$$

The displacement on a string with an infinite number of periodically spaced masses is now given by the sum of the Green's function response for each individual mass. Once again taking the solution to be time-harmonic, we have

$$U(x) = \frac{iM\epsilon}{2} \sum_{n=-\infty}^{+\infty} U(n) e^{i\epsilon|x-n|}, \tag{2.64}$$

where $U(n)$ is the displacement at the nth bead. The solution (2.64) is implicit since it depends on the displacement at the bead positions. Since the set up is periodic, we seek travelling wave solutions in a pass band in the form of Bloch waves with unit amplitude, i.e.

$$U(n) = e^{ik_* n}. \tag{2.65}$$

The quantity $k_*(\epsilon)$ is the unknown Bloch wavenumber that we are aiming to find. This ansatz states that the solution is periodic across the unit cell except for a phase shift. Since we are looking for k_* in a pass band then it will be entirely real. The effective wavenumber is found by evaluating (2.64) at bead position m with the displacement at the bead positions given by (2.65).

Using the Bloch wave solution in (2.64), we have

$$e^{ik_* m} = \frac{iM\epsilon}{2} \sum_{n=-\infty}^{+\infty} e^{ik_* n} e^{i\epsilon|m-n|}. \tag{2.66}$$

Multiplying by $e^{-ik_* m}$, we get

$$1 = \frac{iM\epsilon}{2} \sum_{n=-\infty}^{+\infty} e^{ik_*(n-m)} e^{i\epsilon|m-n|}. \tag{2.67}$$

Using the change of variables $u = n - m$ and splitting the sum into three parts, we have

$$1 = \frac{iM\epsilon}{2} \left\{ \sum_{u=1}^{\infty} e^{iu(\epsilon - k_*)} + 1 + \sum_{u=1}^{\infty} e^{iu(\epsilon + k_*)} \right\}. \tag{2.68}$$

Since k_* is real, a small positive imaginary part may be added to ϵ to ensure convergence. We now make use of the identity

$$\sum_{n=1}^{\infty} r^n = \frac{r}{1-r} \tag{2.69}$$

to give

$$1 = \frac{iM\epsilon}{2} \left\{ \frac{e^{i(\epsilon - k_*)}}{1 - e^{i(\epsilon - k_*)}} + 1 + \frac{e^{i(\epsilon + k_*)}}{1 - e^{i(\epsilon + k_*)}} \right\}. \tag{2.70}$$

This equation may be rearranged to give the dispersion relation

$$\cos(k_*) = \cos(\epsilon) - \frac{M\epsilon}{2}\sin(\epsilon). \tag{2.71}$$

Equation (2.71) may be extended into the region where k_* is complex to give the wavenumber in a stop band. In this case, the Bloch wave solution (2.65) is not well defined since it is unbounded. If instead we study the forced steady state problem, given by

$$\frac{\partial^2 u}{\partial x^2} = \left(1 + M\sum_{n=-\infty}^{\infty}\delta(x-n)\right)\frac{\partial^2 u}{\partial t^2} + \delta(x)e^{-i\epsilon_* t}. \tag{2.72}$$

then the time harmonic solution at the bead positions is given by

$$U(n) = A_*\, e^{ik_*|n|}, \tag{2.73}$$

where

$$A_* = -\frac{i\sin(\epsilon_*)}{2\epsilon_*\sin(k_*)}. \tag{2.74}$$

Equation (2.73) is well defined since the sign of k_* may be chosen such that $U(n)$ is bounded. We will discuss the forced problem in more detail in chapter 4.

The effective wavenumber for an infinite beaded string is pictured in figure 2.5. Clearly, if the modulus of the right-hand side of (2.71) is greater than one, that is

$$\left|\cos\epsilon - \frac{M\epsilon}{2}\sin\epsilon\right| > 1,$$

the wavenumber, k_* has a complex value. Both the real and imaginary parts of k_* are plotted in figure 2.5. The regions where the imaginary part is non-zero correspond to the stop bands, meaning a wave of that frequency cannot propagate. This is evident since a wave of this frequency, emanating from the origin can be written as

$$u(x,t) = Ae^{i(k_*|x|-\epsilon t)} = Ae^{-\Im(k_*)|x|}e^{i(\Re(k_*)|x|-\epsilon t)}, \tag{2.75}$$

and the wave experiences exponential decay in space. Note that we have chosen the branch of k_* such that the imaginary part is positive and waves decay away from the origin rather than grow.

The stop bands are also characterised by a flat portion of the real part implying that the decaying modes have a fixed wavelength. It is interesting to note that the stop bands become wider and closer together as ϵ gets large. This implies that as ϵ

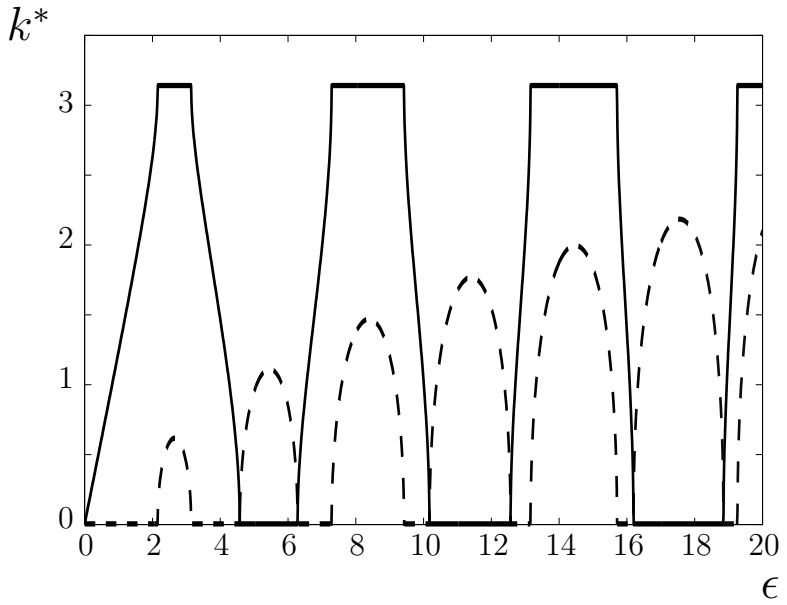

Figure 2.5: The real and imaginary parts of the dispersion curve (2.71) associated with an infinite string with beads placed periodically. The real part is given by a solid line and the imaginary part is given by a dashed line.

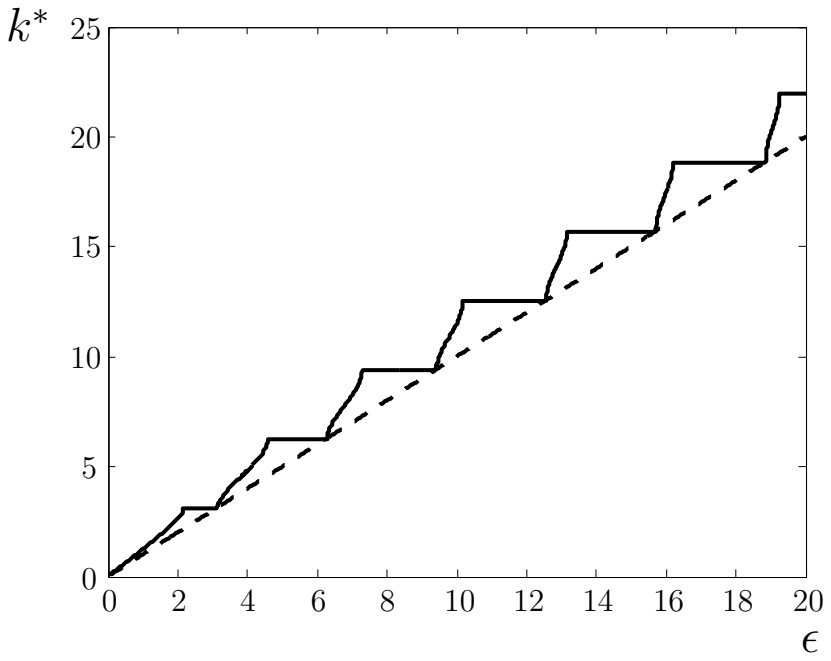

Figure 2.6: The effective wavenumber shifted upwards. The solid line gives the effective wavenumber and dashed line gives the homogeneous string wavenumber.

gets larger, only waves in narrower and narrower frequency bands can propagate. This is in agreement with the single bead case, where high frequencies are entirely reflected by the bead.

It is expected that when $M \to 0$ (vanishing bead mass) we recover the non-dispersive string. The relation for the non-dispersive case is simply

$$k^* = \epsilon. \tag{2.76}$$

The reason we see a disparity between figure 2.5 and what we expect from the small mass limit is because of the multivalued nature of the arccos function. Although we normally define arccos to be the positive branch between 0 and π, in reality it can legitimately take the values

$$\arccos(x) = \pm \arccos(x) + 2n\pi \tag{2.77}$$

for any integer n. In order to get the actual dispersion curve, we must flip and translate each branch of the dispersion curve accordingly. This modified version is pictured in figure 2.6. It is interesting to see how the dispersion curve for the beaded string returns to the nondispersive one at the end of every stop band. This implies that waves at this point travel with the same phase velocity as the string without any beads. This situation must correspond to standing waves where the beads occur at the nodes of the standing waves. The idea of standing waves is reinforced by the fact that the group velocity is zero at the edges of the stop/pass bands. This zero velocity corresponds to no energy transport, thus a standing wave.

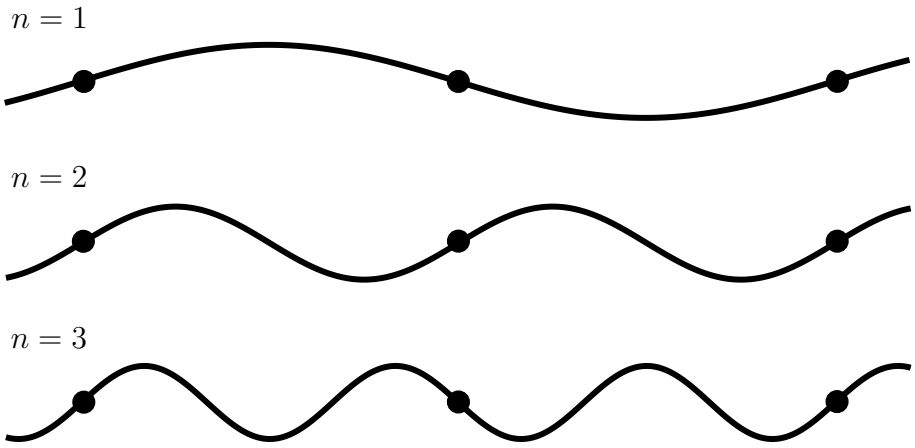

Figure 2.7: The standing waves which occur on the beaded string in the stop band. These waves are evanescent in nature and will decay exponentially away from a forcing point.

We note that the effective wavenumber of each stop band corresponds to $k^* = n\pi$, or $\lambda = 2/n$. Since the bead spacing is nondimensionalised to 1, this corresponds to the

wavelength and bead spacing exactly matching up. A schematic representation of this situation is given in figure 2.7. For a more in depth discussion on this, see reference [8]

2.3 Waves in two-dimensional periodic linearly elastic media

In this section we will outline the basic concepts used in finding band diagrams for two-dimensional periodic elastic materials. The method outlined here will be used in chapters 5 and 6. We begin by stating the basic equations of linear elasticity. Then we define the physical and reciprocal lattices. After this we introduce the plane-wave expansion method, which is used to find band diagrams.

2.3.1 Equations of linear elasticity

Here we briefly summarise the equations of motion for a linearly elastic material with spatially dependent material properties. A thorough summary of linear elasticity is given in [7]. For small deformations the strain at any point, $\mathbf{x}$, is given in index notation by

$$\varepsilon_{ij} = \frac{1}{2}\left(\frac{\partial u_i}{\partial x_j} + \frac{\partial u_j}{\partial x_i}\right), \tag{2.78}$$

where $\mathbf{u} = (u_1, u_2, u_3)$ is the displacement of the material from the state of rest and $\mathbf{x} = (x_1, x_2, x_3)$ is the position. In linear elasticity, we require that $\partial u_i/\partial x_j$ is small.

The Cauchy stress is given by the constitutive law

$$T_{ij} = C_{ijkl}\,\varepsilon_{kl}, \tag{2.79}$$

where C_{ijkl} is the fourth-order stiffness tensor. Unless otherwise stated, we assume summation over repeated indices. The stiffness tensor contains all of the information about how a specific material behaves and seemingly has 81 independent elements. However, by symmetry arguments, we must have

$$C_{ijkl} = C_{klij} = C_{jikl} = C_{ijlk}, \tag{2.80}$$

which reduces the number of independent material constants to 21. For an isotropic material these reduce to just three distinct constants, dependent on two material

parameters.

$$c_{11} = C_{1111} = C_{2222} = C_{3333} = \lambda + 2\mu, \tag{2.81}$$

$$c_{12} = C_{1122} = C_{1133} = C_{2233} = \lambda, \tag{2.82}$$

$$c_{44} = C_{2323} = C_{1313} = C_{1212} = 2\mu. \tag{2.83}$$

With the elasticity tensor written in this notation, the constitutive equation (2.79) can be written in matrix form

$$\begin{bmatrix} T_{11} \\ T_{22} \\ T_{33} \\ T_{23} \\ T_{13} \\ T_{12} \end{bmatrix} = \begin{bmatrix} c_{11} & c_{12} & c_{12} & 0 & 0 & 0 \\ c_{12} & c_{11} & c_{12} & 0 & 0 & 0 \\ c_{12} & c_{12} & c_{11} & 0 & 0 & 0 \\ 0 & 0 & 0 & c_{44} & 0 & 0 \\ 0 & 0 & 0 & 0 & c_{44} & 0 \\ 0 & 0 & 0 & 0 & 0 & c_{44} \end{bmatrix} \begin{bmatrix} \varepsilon_{11} \\ \varepsilon_{22} \\ \varepsilon_{33} \\ \varepsilon_{23} \\ \varepsilon_{13} \\ \varepsilon_{12} \end{bmatrix}. \tag{2.84}$$

The equation of motion may be found by calculating the linear momentum in an arbitrary volume of material. In the absence of body forces, the equation of motion is given by

$$\mathrm{div}\mathbf{T} = \rho\frac{\partial^2\mathbf{u}}{\partial t^2}, \tag{2.85}$$

where ρ is the density of the material. By substituting (2.79) into this equation, we get the equation of motion in terms of displacement. In index notation this is

$$\frac{\partial}{\partial x_i}\left(\lambda\left(\frac{\partial u_k}{\partial x_k}\right)\right) + \frac{\partial}{\partial x_k}\left(\mu\left(\frac{\partial u_i}{\partial x_k} + \frac{\partial u_k}{\partial x_i}\right)\right) = \rho\frac{\partial^2 u_i}{\partial t^2}, \quad \text{for } i = 1, 2, 3\,. \tag{2.86}$$

In general the material properties λ, μ and ρ are all spatially dependent.

If we are to assume that the material properties have no spatial variation, in vector notation equation (2.86) becomes

$$(\lambda + \mu)\nabla(\nabla \cdot \mathbf{u}) + \mu\nabla^2\mathbf{u} = \rho\frac{\partial^2\mathbf{u}}{\partial t^2}. \tag{2.87}$$

By writing $\mathbf{u}$ in terms of scalar and vector potentials,

$$\mathbf{u} = \nabla\phi + \nabla \times \mathbf{H}, \tag{2.88}$$

and imposing the condition that $\nabla \cdot \mathbf{H} = 0$, it is possible to show that this equation (2.87) can be converted into two wave equations

$$(\lambda + 2\mu)\nabla^2\phi = \rho\frac{\partial^2\phi}{\partial t^2}, \tag{2.89}$$

$$\mu\nabla^2\mathbf{H} = \rho\frac{\partial^2\mathbf{H}}{\partial t^2}. \tag{2.90}$$

These equations govern the propagation of pressure and shear waves respectively and are coupled by the boundary conditions at interfaces. We note here that $c_p = \sqrt{(\lambda + 2\mu)/\rho}$ gives the pressure wave speed and $c_s = \sqrt{\mu/\rho}$ gives the shear wave speed.

Decoupling of SH and P-SV waves in two-dimensional media

We make a quick note here about two-dimensional systems and the decoupling of vibrations into two distinct modes. For a two-dimensional material in a Cartesian coordinate we assume that we have no variation in material properties in the z direction and all variation occurs in the x, y plane. For the sake of illustration, assume that we have a stress-free boundary positioned in the plane defined by $y = 0$, giving the boundary conditions

$$T_{21} = T_{22} = T_{23} = 0, \quad \text{on } y = 0. \tag{2.91}$$

In this case the displacements given by (2.88) are given by

$$u_1 = \frac{\partial \phi}{\partial x} + \frac{\partial H_3}{\partial y}, \tag{2.92}$$

$$u_2 = \frac{\partial \phi}{\partial y} - \frac{\partial H_3}{\partial x}, \tag{2.93}$$

$$u_3 = -\frac{\partial H_1}{\partial y} + \frac{\partial H_2}{\partial x}. \tag{2.94}$$

From (2.84), the components of the stress tensor on the surface $y = 0$ needed for the boundary condition are

$$T_{21} = \mu \left(\frac{\partial u_1}{\partial y} + \frac{\partial u_2}{\partial x} \right), \tag{2.95}$$

$$T_{22} = (\lambda + 2\mu)\frac{\partial u_2}{\partial y} + \lambda \frac{\partial u_1}{\partial x}, \tag{2.96}$$

$$T_{23} = \mu \frac{\partial u_3}{\partial y}. \tag{2.97}$$

We can see from here that the components of displacement in plane with material variations, u_x and u_y, depend only on ϕ and H_3, which are governed by equation (2.89) and the third component of (2.90) respectively. We shall refer to this as the coupled pressure and vertically polarised shear mode (P-SV mode), since it is made up of both a pressure component and a shear component.

The component of displacement in the direction perpendicular to the plane of variation, u_z, is dependent only on H_1 and H_2, which are governed by the first and

second component of (2.90). We shall refer to this as the horizontally polarised shear mode (SH mode), since it contains only a shear component and no pressure component. This decoupling is discussed in more detail in chapter 6 of [28].

2.3.2 Periodic lattices

In order to describe a two-dimensional periodic material and use the plane-wave expansion method, we require a basic knowledge of periodic lattices and their reciprocal lattices. A general two-dimensional lattice is pictured in figure 2.8, with the periodic unit cell being shown by a dashed parallelogram. The lattice basis vectors are given by $\mathbf{a_1}$ and $\mathbf{a_2}$, with a general lattice point being given by

$$\mathbf{R} = m\,\mathbf{a_1} + n\,\mathbf{a_2} \tag{2.98}$$

for some integers m and n. The reciprocal lattice is defined by the basis vectors $\mathbf{b_1}$ and $\mathbf{b_2}$, such that

$$\mathbf{a_i} \cdot \mathbf{b_j} = 2\pi\delta_{ij}. \tag{2.99}$$

The relevance of the factor 2π will be discussed later when we define the Fourier series expansions. A lattice point in the reciprocal lattice is given by

$$\mathbf{G} = m\mathbf{b_1} + n\mathbf{b_2}, \tag{2.100}$$

for integers m and n. It is clear from the definition of the reciprocal lattice, that the vectors $\mathbf{a_i}$ and $\mathbf{b_j}$ are orthogonal, provided $i \neq j$. The parallelogram on the reciprocal lattice is known as the first Brillouin zone. A good introduction to lattices is given by Brillouin in his book on wave propagation [8].

We choose to extend the idea of crystalline lattices (with point particles at each lattice point) to more general periodic structures. The periodic cell is given by the parallelogram on the real lattice in figure 2.8. We describe the material by defining the properties of the elastic composite within this periodic cell.

In the special case of a square lattice, the lattice vector is given by

$$\mathbf{R} = \ell\left(m\hat{\mathbf{i}} + n\hat{\mathbf{j}}\right), \tag{2.101}$$

where $\hat{\mathbf{i}}$ and $\hat{\mathbf{j}}$ are the Cartesian unit basis vectors, oriented in the x and y directions respectively. The value of ℓ is the lattice constant, that is the period of the cell in

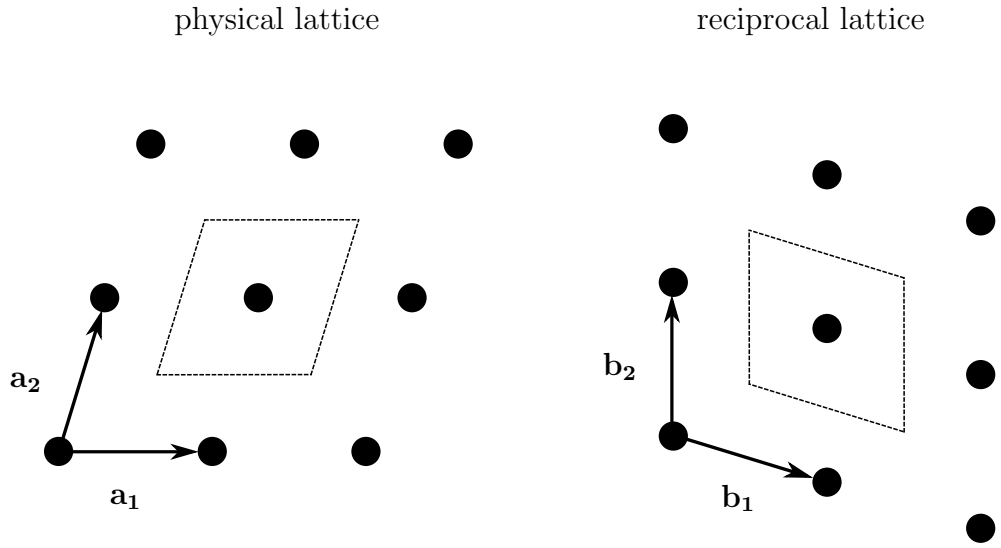

Figure 2.8: The physical lattice, defined by its basis vectors $\mathbf{a_1}$ and $\mathbf{a_2}$, and the reciprocal lattice, defined by its basis vectors $\mathbf{b_1}$ and $\mathbf{b_2}$. The parallelograms show the periodic cell in the physical lattice and the first Brillouin zone in the reciprocal lattice.

either the x or y direction. We use the nondimensionalisation given by (2.8) to give the lattice unit spacing

$$\mathbf{R} = m\hat{\mathbf{i}} + n\hat{\mathbf{j}}. \tag{2.102}$$

In this case, the reciprocal lattice vectors are given by

$$\mathbf{G} = 2\pi\left(m\hat{\mathbf{i}} + n\hat{\mathbf{j}}\right), \tag{2.103}$$

for any integers m and n.

2.3.3 The plane-wave expansion method

We are interested in studying the propagation of waves in periodic two-dimensional media with a focus on the stop bands of the system. There are a number of methods used for finding the stop bands of two-dimensional systems. For simple geometries these commonly involve multipole methods [58], in which the modal response of the scattered field from a single inclusion must be known. In situations where the modal response is not straightforward to determine, e.g. scattering from complex shapes, another alternative is to use the finite element method [98], which can be computationally expensive. More recently developed is the method of high-frequency homogenisation, used to find the asymptotic behaviour close to standing wave modes [3].

We choose to use the plane-wave expansion method to find the band structure. This method is widely used for finding the dispersion diagrams of periodic composites. As we will see in the following chapters, the method easily accommodates the inhomogeneous material properties induced by the finite nonlinear deformation.

The fundamental idea behind this method is to expand both the displacement and the material properties as a sum of plane waves. We are then able to obtain a system of linear equations, the eigenvalues of which give the frequency of oscillation. The plane-wave expansion method is a very effective tool. It works in any number of dimensions and for a variety of different geometries. For an introduction to its use in elasticity, see Kushwaha [47].

To introduce the plane-wave expansion method we give an example of the band diagram determination in antiplane elasticity. The elastic medium of interest is periodic in the x and y directions as shown in figure 2.9. There is no variation of material properties in the z direction, but all displacements are confined to this direction. As mentioned earlier, this gives a pure antiplane shear wave and there is no conversion between pressure and shear waves.

Applying the restrictions described above, the equation of motion given by (2.86) simplifies to

$$\nabla \cdot (\mu \nabla u_z) = \rho \frac{\partial^2 u_z}{\partial t^2}, \tag{2.104}$$

where u_z is the displacement in the z direction, $\rho = \rho(x, y) = \rho(\mathbf{x})$ is the density at the point $\mathbf{x}$ and $\mu = \mu(\mathbf{x}) = \rho\, c_t^2$ is the shear modulus (with c_t being the transverse (shear) wavespeed). Note that the point $\mathbf{x}$ used above is defined as $\mathbf{x} = x\,\hat{\mathbf{i}} + y\,\hat{\mathbf{j}}$ and is the two-dimensional spatial vector. We have chosen here to nondimensionalise the shear modulus and density on those in the host (μ_0 and ρ_0 respectively), as well as nondimensionalising time using equation (2.8) where $c_0 = \sqrt{\mu_0/\rho_0}$.

Since all of the material properties are periodic, we can write them as a Fourier series. The basis functions used for the Fourier series is the set of all plane waves. The wavenumbers of these plane waves are given by the reciprocal lattice vector. For the density, we have

$$\rho(\mathbf{x}) = \sum_{\mathbf{G}} \rho_{\mathbf{G}}\, e^{i\mathbf{G}\cdot\mathbf{x}}, \tag{2.105}$$

where the sum is taken over all m and n in the definition of the reciprocal lattice vector (2.103). The justification for the factor 2π in the definition of the reciprocal

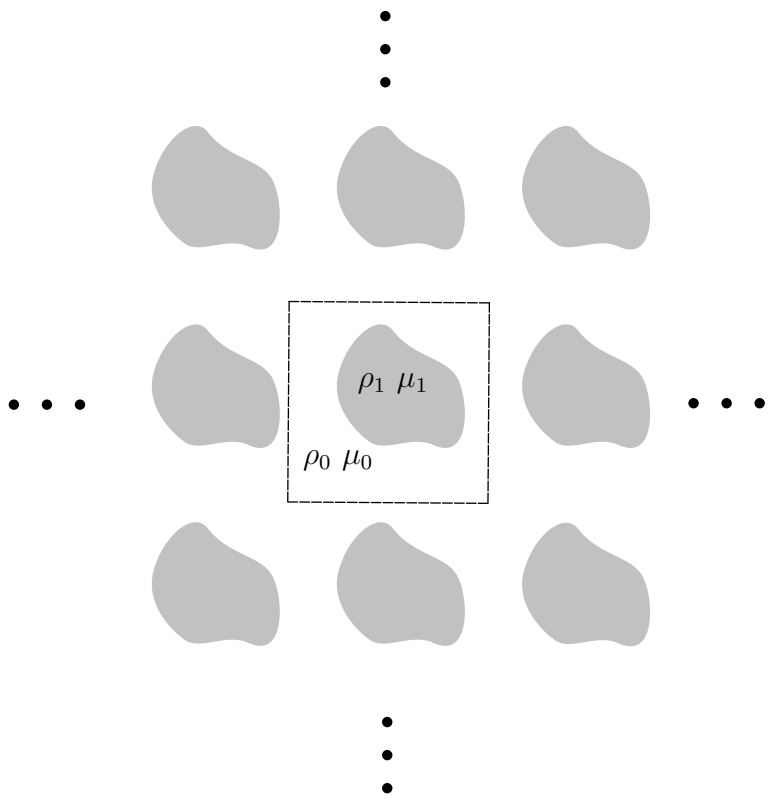

Figure 2.9: The two-phase elastic composite of interest with the unit cell outlined by a dashed line. The host phase is white and is referenced by a subscript 0, the inclusion phase is grey and is referenced by a subscript 1.

lattice vector (2.99) becomes clear if we increment the position vector by a period, i.e. $\mathbf{x} \to \mathbf{x} + \hat{\mathbf{i}}$. In this case, the density remains unchanged, since

$$\rho(\mathbf{x} + \hat{\mathbf{i}}) = \sum_{\mathbf{G}} \rho_{\mathbf{G}}\, e^{i\mathbf{G}\cdot(\mathbf{x}+\hat{\mathbf{i}})} = \sum_{\mathbf{G}} \rho_{\mathbf{G}}\, e^{i\mathbf{G}\cdot\mathbf{x}}\, e^{i2\pi m} = \rho(\mathbf{x}). \tag{2.106}$$

For the shear modulus, we have a similar expansion to (2.105)

$$\mu(\mathbf{x}) = \sum_{\mathbf{G}} \mu_{\mathbf{G}}\, e^{i\mathbf{G}\cdot\mathbf{x}}. \tag{2.107}$$

For each $\mathbf{G}$, the value of $\rho_{\mathbf{G}}$ is given by the integral

$$\rho_{\mathbf{G}} = \frac{1}{A} \iint_{\text{Cell}} \rho(\mathbf{x}) e^{-i\mathbf{G}\cdot\mathbf{x}}\, d\mathbf{x}, \tag{2.108}$$

where the integral is evaluated over the unit cell, which has an area A. Due to the chosen nondimensionalisation, this area will be unity. A similar integral is given for $\mu_{\mathbf{G}}$,

$$\mu_{\mathbf{G}} = \iint_{\text{Cell}} \mu(\mathbf{x}) e^{-i\mathbf{G}\cdot\mathbf{x}}\, d\mathbf{x}. \tag{2.109}$$

In order to factor time out of the problem, we impose a harmonic time dependence on the displacement, so $u_z(\mathbf{x},t) = w(\mathbf{x})e^{-i\omega t}$, where ω is the nondimensional frequency given by equation (2.11). Since the problem is periodic we can write the displacement $w(\mathbf{x})$ as a Fourier series in the form

$$w(\mathbf{x}) = e^{i\mathbf{K}\cdot\mathbf{x}} \sum_{\mathbf{G}} w_{\mathbf{G}} e^{i\mathbf{G}\cdot\mathbf{x}}, \tag{2.110}$$

where $\mathbf{K}$ is the Bloch wave number. The reason for introducing $e^{i\mathbf{K}\cdot\mathbf{x}}$ is to satisfy the Bloch condition that the solution is entirely periodic, except for a phase shift across the unit cell. To show this condition is satisfied, we add a generic lattice vector $\mathbf{R} = o\,\mathbf{a_1} + p\,\mathbf{a_2}$ $(o,p \in \mathbb{Z})$ to $\mathbf{x}$, giving

$$\begin{aligned} w(\mathbf{x}+\mathbf{R}) &= e^{i(\mathbf{K}\cdot(\mathbf{x}+\mathbf{R}))} \sum_{\mathbf{G}} w_{\mathbf{G}}\, e^{i\mathbf{G}\cdot(\mathbf{x}+\mathbf{R})} \\ &= e^{i\mathbf{K}\cdot\mathbf{R}}\, e^{i\mathbf{K}\cdot\mathbf{x}} \sum_{\mathbf{G}} w_{\mathbf{G}}\, e^{i\mathbf{G}\cdot\mathbf{x}}\; e^{i\mathbf{G}\cdot\mathbf{R}} \\ &= e^{i\mathbf{K}\cdot\mathbf{R}}\, e^{i\mathbf{K}\cdot\mathbf{x}} \sum_{\mathbf{G}} w_{\mathbf{G}}\, e^{i\mathbf{G}\cdot\mathbf{x}}\; e^{i2\pi(m\,o+n\,p)} \\ &= \mathrm{e}^{i\mathbf{K}\cdot\mathbf{R}} w(\mathbf{x}), \end{aligned}$$

since m, n, o and p are all integers.

We proceed by taking the spatial derivative of $w(\mathbf{x})$ as required in (2.104). We first take the gradient of w

$$\begin{aligned} \nabla w &= \frac{\partial w}{\partial x}\,\hat{\mathbf{i}} + \frac{\partial w}{\partial y}\,\hat{\mathbf{j}} \\ &= \sum_{\mathbf{G}} i\left((K_x+G_x)\,\hat{\mathbf{i}} + (K_y+G_y)\,\hat{\mathbf{j}}\right) w_{\mathbf{G}}\, e^{i(\mathbf{K}+\mathbf{G})\cdot\mathbf{x}}\,. \end{aligned}$$

Using the form of $\mu(\mathbf{x})$ from (2.107), we have

$$\mu\nabla w = \sum_{\mathbf{H}}\sum_{\mathbf{G}} i\left((K_x+G_x)\,\hat{\mathbf{i}} + (K_y+G_y)\,\hat{\mathbf{j}}\right) w_{\mathbf{G}}\,\mu_{\mathbf{H}}\, e^{i(\mathbf{K}+\mathbf{G}+\mathbf{H})\cdot\mathbf{x}}, \tag{2.111}$$

using $\mathbf{H}$ to highlight the difference between the expansions of material properties and the displacement. We now take the divergence of this

$$\begin{aligned} \nabla\cdot(\mu\nabla w) &= -\sum_{\mathbf{G}}\sum_{\mathbf{H}} \big((K_x+G_x)(K_x+G_x+H_x) \\ &\quad +(K_y+G_y)(K_y+G_y+H_y)\big)\, w_{\mathbf{G}}\,\mu_{\mathbf{H}}\, e^{i(\mathbf{K}+\mathbf{G}+\mathbf{H})\cdot\mathbf{x}} \\ &= -\sum_{\mathbf{G}}\sum_{\mathbf{H}} (\mathbf{K}+\mathbf{G})\cdot(\mathbf{K}+\mathbf{G}+\mathbf{H}) w_{\mathbf{G}}\,\mu_{\mathbf{H}}\, e^{i(\mathbf{K}+\mathbf{G}+\mathbf{H})\cdot\mathbf{x}}. \end{aligned} \tag{2.112}$$

Note that we have swapped the order of the sums. By defing the new vector $\mathbf{G}'$, such that $\mathbf{G}' = \mathbf{G} + \mathbf{H}$ we shift the vector $\mathbf{H}$ by $\mathbf{G}$. The reason for doing this is to obtain the exponential term purely as a function of just one of the lattice vectors. Since the sums are over all possible values of $\mathbf{G}$ and $\mathbf{H}$, we can simply exchange the sum over $\mathbf{H}$ with one over $\mathbf{G}'$. Our spatial derivative becomes

$$\nabla \cdot (\mu \nabla w) = -\sum_{\mathbf{G}'} \sum_{\mathbf{G}} (\mathbf{K} + \mathbf{G}) \cdot (\mathbf{K} + \mathbf{G}') w_{\mathbf{G}} \, \mu_{\mathbf{G}'-\mathbf{G}} \, e^{i(\mathbf{K}+\mathbf{G}')\cdot\mathbf{x}}. \tag{2.113}$$

Bringing everything together by plugging this into (2.104), we have

$$\sum_{\mathbf{G}'} \Big[\sum_{\mathbf{G}} \left((\mathbf{K} + \mathbf{G}) \cdot (\mathbf{K} + \mathbf{G}') \, \mu_{\mathbf{G}'-\mathbf{G}} - \omega^2 \rho_{\mathbf{G}'-\mathbf{G}} \right) w_{\mathbf{G}} \Big] e^{i(\mathbf{K}+\mathbf{G}')\cdot\mathbf{x}} = 0. \tag{2.114}$$

Since this must apply for all $\mathbf{x}$, for each $\mathbf{G}'$ we require that

$$\sum_{\mathbf{G}} \left((\mathbf{K} + \mathbf{G}) \cdot (\mathbf{K} + \mathbf{G}') \, \mu_{\mathbf{G}'-\mathbf{G}} - \omega^2 \rho_{\mathbf{G}'-\mathbf{G}} \right) w_{\mathbf{G}} = 0. \tag{2.115}$$

This is an infinite system of equations which, given a value of the Bloch wavevector $\mathbf{K}$, we truncate to find an approximate value of ω. The conventional procedure is to scan the Bloch wavevector around the outside of the irreducible Brillouin zone. It is widely accepted that when looking for stop bands, the edge of the irreducible Brillouin zone gives all the important information about a material. For example, if there is a frequency that will not propagate around the edge of this zone, we have an absolute band gap inside the entire Brillouin zone [86]. In some rare cases it may be necessary to search inside the Brillouin zone [12].

2.3.4 A two-phase composite

Until now, the analysis has been applicable to a generic cell of any shape with either discontinuous or smoothly varying properties. In order to give an illustrative example, we restrict ourselves to the two-phase composite pictured in figure 2.9. We choose the inclusions to be circular in shape to further simplify the analysis. We refer to the material outside this circle to be the host.

Since the material properties are homogeneous in each region, we can split the integrals given by (2.108) and (2.109) into two. As an example, we look at the density

integral first. For the case when $\mathbf{G} = \mathbf{0}$, we have

$$\begin{aligned}\rho_{\mathbf{G}} &= \iint_{\text{Cell}} \rho(\mathbf{x}) d\mathbf{x} \\ &= \rho_0 \iint_{\text{Host}} d\mathbf{x} + \rho_1 \iint_{\text{Inc}} d\mathbf{x} \\ &= \rho_0(1-\phi) + \rho_1 \phi\,, \end{aligned} \tag{2.116}$$

where ϕ is the volume fraction of the inclusion. We note that $1 - \phi = A_{\text{Host}}$ and $\phi = A_{\text{Inc}}$ where the subscript 'Inc' refers to the inclusion.

For the case where $\mathbf{G} \neq \mathbf{0}$ we have

$$\begin{aligned}\rho_{\mathbf{G}} &= \iint_{\text{Cell}} \rho(\mathbf{x}) e^{-i\mathbf{G}\cdot\mathbf{x}} d\mathbf{x} \\ &= \rho_0 \iint_{\text{Host}} e^{-i\mathbf{G}\cdot\mathbf{x}} d\mathbf{x} + \rho_1 \iint_{\text{Inc}} e^{-i\mathbf{G}\cdot\mathbf{x}} d\mathbf{x}. \end{aligned} \tag{2.117}$$

We now make use of the fact that if we integrate any of the plane waves over the unit cell, all peaks and troughs cancel to give zero. Because of this, we can write the integral of the plane waves over the whole cell as

$$\iint_{\text{Cell}} e^{-i\mathbf{G}\cdot\mathbf{x}} d\mathbf{x} = \iint_{\text{Host}} e^{-i\mathbf{G}\cdot\mathbf{x}} d\mathbf{x} + \iint_{\text{Inc}} e^{-i\mathbf{G}\cdot\mathbf{x}} d\mathbf{x} = 0. \tag{2.118}$$

Using this in (2.117), we get

$$\rho_{\mathbf{G}} = (\rho_1 - \rho_0) F(\mathbf{G}), \tag{2.119}$$

where $F(\mathbf{G})$ is known as the form factor or shape function. It is given by

$$F(\mathbf{G}) = \iint_{\text{Inc}} e^{-i\mathbf{G}\cdot\mathbf{x}} d\mathbf{x}. \tag{2.120}$$

As mentioned previously, if we assume that the inclusions are circular in cross section, with radius r_0, then the form factor integral becomes

$$F(\mathbf{G}) = \int_0^{r_0} \int_0^{2\pi} r e^{-i|\mathbf{G}| r\cos\theta}\, d\theta\, dr. \tag{2.121}$$

We have chosen to write the exponent in the form $-i|\mathbf{G}| r\cos\theta = -i\mathbf{G}\cdot\mathbf{x}$, where the value of θ denotes the angle between $\mathbf{G}$ and $\mathbf{x}$. By splitting the θ integral into two

$$F(\mathbf{G}) = \int_0^{r_0} r \left[\int_0^{\pi} e^{-i|\mathbf{G}| r\cos\theta}\, d\theta + \int_0^{\pi} e^{i|\mathbf{G}| r\cos\theta}\, d\theta \right] dr, \tag{2.122}$$

we get integrals of the form of equation (9.1.21) in Abramowitz and Stegun [2]. These integrals can be written as

$$F(\mathbf{G}) = \pi \int_0^{r_0} r\big[J_0(-|\mathbf{G}|r) + J_0(|\mathbf{G}|r)\big]dr, \tag{2.123}$$

where J_0 is the Bessel function of the first kind. Since J_0 is even, we have

$$F(\mathbf{G}) = 2\pi \int_0^{r_0} r J_0(|\mathbf{G}|r)dr. \tag{2.124}$$

This integral can be evaluated using equation (11.3.20) in [2], giving

$$F(\mathbf{G}) = \frac{2\phi}{r_0|\mathbf{G}|} J_1(|\mathbf{G}|r_0), \tag{2.125}$$

where $\phi = \pi r_0^2$ is the volume fraction of the inclusion as defined above.

Solving the system

We now have everything we need to solve (2.115) for the eigenvalues. The system of equations to be solved is

$$\sum_{\mathbf{G}} \left((\mathbf{K}+\mathbf{G})\cdot(\mathbf{K}+\mathbf{G}')\,\mu_{\mathbf{G}'-\mathbf{G}} - \omega^2\rho_{\mathbf{G}'-\mathbf{G}}\right) w_{\mathbf{G}} = 0.$$

This may be rewritten as a generalised matrix eigenvalue problem

$$\mathbf{A}\mathbf{w}_{\mathbf{G}} = \omega^2 \mathbf{B}\,\mathbf{w}_{\mathbf{G}}. \tag{2.126}$$

The components of the matrix A_{ij} are given as

$$A_{ij} = (\mathbf{K}+\mathbf{G}_j)\cdot(\mathbf{K}+\mathbf{G}_i)\mu_{\mathbf{G}_i-\mathbf{G}_j}, \tag{2.127}$$

whereas the components of the matrix B_{ij} are

$$B_{ij} = \rho_{\mathbf{G}_i-\mathbf{G}_j}. \tag{2.128}$$

The vector $\mathbf{G}_i$ represents specific values of m and n in the reciprocal lattice vector. In order to reduce the two-dimensional problem to a one-dimensional eigenvalue problem, we have indexed each lattice vector by a single subscript index i, as detailed below. Practically this only works for a finite number of lattice vectors but this is always the case in the plane-wave expansion method.

In order to solve the problem numerically, we must truncate the system, so that everything is expanded in terms of a finite number of plane waves, thus allowing us to construct the matrices **A** and **B**. Recall that the reciprocal lattice vector for a square lattice is given by (2.103)

$$\mathbf{G} = 2\pi \left(m\hat{\mathbf{i}} + n\hat{\mathbf{j}} \right). \tag{2.129}$$

We restrict the reciprocal lattice vector by allowing m and n to reside in the range $-N_{\max} \leq m, n \leq N_{\max}$. This gives a total of $(2N_{\max}+1)^2$ distinct plane waves. We can now describe how $\mathbf{G}_i$ is indexed. The index of the reciprocal lattice vector i runs from $i = 1, \ldots, (2N_{\max}+1)^2$. For $i = 1, \ldots, 2N_{\max}+1$, we set $m = -N_{\max}$ while n runs from $-N_{\max}$ to $N_{\max}$. For $i = 2N_{\max}+2, \ldots, 2(2N_{\max}+1)$, we set $m = -N_{\max}+1$ and again n runs from $-N_{\max}$ to $N_{\max}$. This pattern is followed until $i = (2N_{\max}+1)^2$, at which point $m = n = N_{\max}$.

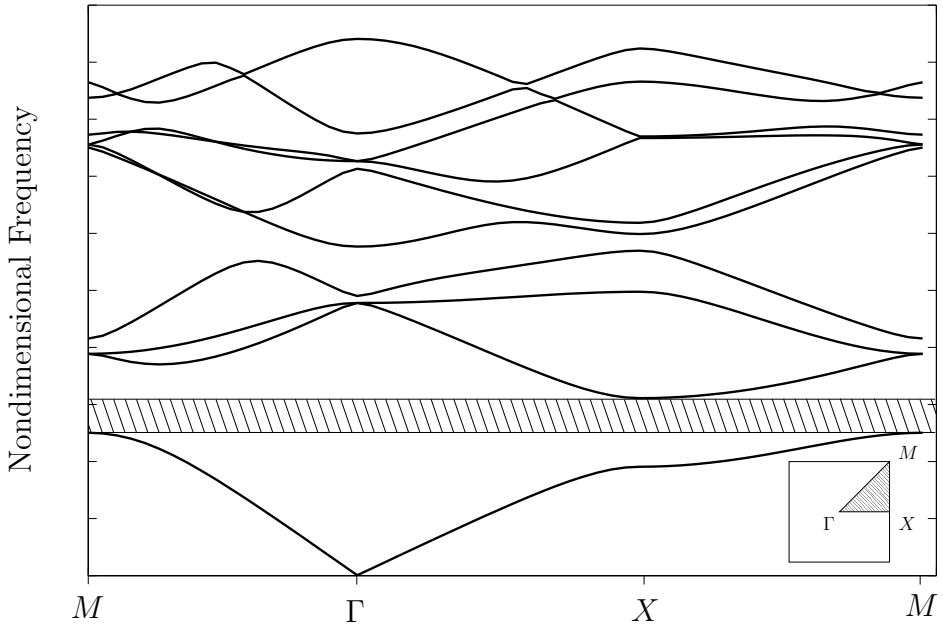

Figure 2.10: The band diagram for a two-dimensional elastic composite with circular inclusions. We scan around the irreducible Brillouin zone depicted by the triangle in the bottom right. We can see an absolute band gap in the shaded region just above the first branch.

We find the eigenfrequencies by using the Matlab `eig` function to solve (2.126). We use $N_{\max} = 10$, which gives 441 plane-waves. For most geometries this program runs relatively quickly on a standard desktop computer and recreates the band diagram accurately for a relatively low number of plane waves. This method has been compared

with an integral equation method at low frequencies, and to a multipole method for small scatterers. Good agreement was observed in both cases. The plane-wave expansion method struggles when modelling small scatterers since a large number of plane waves are needed to resolve the inclusion. A similar issue occurs with large scatterers that almost touch.

An example of the band diagram is given in figure 2.10. We give $\mathbf{K}$ values along the boundary of the irreducible Brillouin zone, which is pictured on the bottom right of the figure. The three points defining the Brillouin zone are M, Γ and X.

Each branch corresponds to different eigenvalues of the system. The higher order modes play a less important roll in the behaviour of the system, so we only show the first ten branches. As expected, we see homogenised, non-dispersive behaviour at low frequencies. In this case, we can see an absolute band gap just above the first branch.

Determining the band gap structure for more complicated systems such as the coupled P-SV mode or the fully three-dimensional problem is achieved in much the same way as described here. There is obvious increase in complexity and therefore computational time experienced. The key advantage of the plane-wave expansion method is its flexibility in modelling different geometries. As we will see later, this method lends itself well to finding the band diagrams of pre-stressed nonlinearly elastic media.

2.4 Nonlinear elasticity and the theory of small-on-large

We are interested in studying the effect that a large pre-stress has on the band structure of an elastic material. In order to achieve this, we must develop the theory associated with wave propagation in pre-stressed heterogeneous media. The theory of small-on-large is used, which describes the propagation of small amplitude waves in an elastic material that has undergone a large initial deformation.

In the following section we introduce the basic concepts of nonlinear elasticity, finite deformation and the theory of small-on-large. The introduction is in no way exhaustive, but consists simply of what is required in the rest of this thesis. At the same time, we describe the deformation used throughout this thesis, namely the axial

stretching and radial inflation of an annular cylinder. Many of the ideas along with the notation used here follows that introduced in the PhD thesis of Shearer [76].

2.4.1 Cylindrical coordinates

Since the geometry of our deformation is cylindrically symmetric, it is convenient to work in cylindrical polar coordinates. We define a vector in cylindrical coordinates relative to the unit basis vectors $\hat{\mathbf{r}}$, $\hat{\boldsymbol{\theta}}$ and $\hat{\mathbf{z}}$ pointing in the radial, azimuthal and axial directions respectively. For example, a general vector $\mathbf{v}$ is given by

$$\mathbf{v} = v_r\hat{\mathbf{r}} + v_\theta\hat{\boldsymbol{\theta}} + v_z\hat{\mathbf{z}}. \tag{2.130}$$

A general position vector $\mathbf{x}$ may be written as

$$\mathbf{x} = r\,\hat{\mathbf{r}}(\theta) + z\,\hat{\mathbf{z}}, \tag{2.131}$$

where the polar coordinates may be written in terms of the Cartesian using

$$r = \sqrt{x^2+y^2}, \qquad \theta = \tan^{-1}\left(\frac{y}{x}\right) \quad \text{and} \quad z = z. \tag{2.132}$$

Note that the direction of the unit radial basis vector in (2.131) is dependent on the angle θ.

It is useful to define the differential operators in cylindrical coordinates. The more common ones are the gradient of a scalar, given by

$$\nabla f(\mathbf{r}) = \hat{\mathbf{r}}\frac{\partial f}{\partial r} + \hat{\boldsymbol{\theta}}\frac{1}{r}\frac{\partial f}{\partial \theta} + \hat{\mathbf{z}}\frac{\partial f}{\partial z} \tag{2.133}$$

and the divergence of a vector

$$\nabla\cdot\mathbf{v}(\mathbf{r}) = \frac{1}{r}\frac{\partial\left(rv_r\right)}{\partial r} + \frac{1}{r}\frac{\partial v_\theta}{\partial\theta} + \frac{\partial v_z}{\partial z}, \tag{2.134}$$

where v_r, v_θ and v_z are the respective components of the vector in the r, θ and z directions. Combining (2.133) and (2.134) gives the scalar Laplacian

$$\nabla^2 f(\mathbf{r}) = \frac{1}{r}\frac{\partial}{\partial r}\left(r\frac{\partial f}{\partial r}\right) + \frac{1}{r^2}\frac{\partial^2 f}{\partial\theta^2} + \frac{\partial^2 f}{\partial z^2}. \tag{2.135}$$

Operators that are less common include the gradient of a vector and the divergence

of a tensor. The first of these is given by

$$\begin{aligned}\nabla \otimes \mathbf{v}(\mathbf{r}) =& \frac{\partial v_r}{\partial r}\hat{\mathbf{r}} \otimes \hat{\mathbf{r}} + \frac{1}{r}\left(\frac{\partial v_r}{\partial \theta} - v_\theta\right)\hat{\mathbf{r}} \otimes \hat{\boldsymbol{\theta}} + \frac{\partial v_r}{\partial z}\hat{\mathbf{r}} \otimes \hat{\mathbf{z}} \\ &+ \frac{\partial v_\theta}{\partial r}\hat{\boldsymbol{\theta}} \otimes \hat{\mathbf{r}} + \frac{1}{r}\left(\frac{\partial v_\theta}{\partial \theta} + v_r\right)\hat{\boldsymbol{\theta}} \otimes \hat{\boldsymbol{\theta}} + \frac{\partial v_\theta}{\partial z}\hat{\boldsymbol{\theta}} \otimes \hat{\mathbf{z}} \\ &+ \frac{\partial v_z}{\partial r}\hat{\mathbf{z}} \otimes \hat{\mathbf{r}} + \frac{1}{r}\frac{\partial v_z}{\partial \theta}\hat{\mathbf{z}} \otimes \hat{\boldsymbol{\theta}} + \frac{\partial v_z}{\partial z}\hat{\mathbf{z}} \otimes \hat{\mathbf{z}}, \end{aligned} \tag{2.136}$$

where $\otimes$ denotes the tensor product. The divergence of a tensor is given by

$$\begin{aligned}\nabla \cdot \mathbf{A} =& \left(\frac{\partial A_{rr}}{\partial r} + \frac{1}{r}\frac{\partial A_{\theta r}}{\partial \theta} + \frac{\partial A_{zr}}{\partial z} + \frac{1}{r}\left(A_{rr} - A_{\theta\theta}\right)\right)\hat{\mathbf{r}} \\ &+ \left(\frac{\partial A_{r\theta}}{\partial r} + \frac{1}{r}\frac{\partial A_{\theta\theta}}{\partial \theta} + \frac{\partial A_{z\theta}}{\partial z} + \frac{1}{r}\left(A_{r\theta} + A_{\theta r}\right)\right)\hat{\boldsymbol{\theta}} \\ &+ \left(\frac{\partial A_{rz}}{\partial r} + \frac{1}{r}\frac{\partial A_{\theta z}}{\partial \theta} + \frac{\partial A_{zz}}{\partial z} + \frac{1}{r}A_{rz}\right)\hat{\mathbf{z}}, \end{aligned} \tag{2.137}$$

where $A_{\alpha\beta}$ denote the elements of the tensor $\mathbf{A}$ with respect to the cylindrical polar coordinate basis. Details of how these expressions are derived may be found in the first chapter of [61].

2.4.2 Static deformation

We will begin this section by describing the deformation used in chapters 5 and 6 of this thesis. We define this now so that it may be used as an example when deriving the incremental equations of elasticity. The static deformation considered in this thesis is the radial inflation of an annular cylinder, accompanied by an axial stretch. In chapter 5 we consider the cylinder to be incompressible whereas in chapter 6, the cylinder is compressible. In both cases, for simplicity of presentation, we insist that the outer radius remains fixed. The reasons for this will become clear later. A sketch of the deformation is given in figure 2.11.

The deformation is formalised by writing the coordinates of the undeformed configuration in terms of the deformed configuration

$$R = R(r), \qquad \Theta = \theta \quad \text{and} \quad Z = \frac{z}{\beta}, \tag{2.138}$$

where β is the axial stretch that characterises the deformation. This will be the single parameter we vary when investigating different deformations. We have used the convention that upper case letters correspond to the undeformed configuration and lower

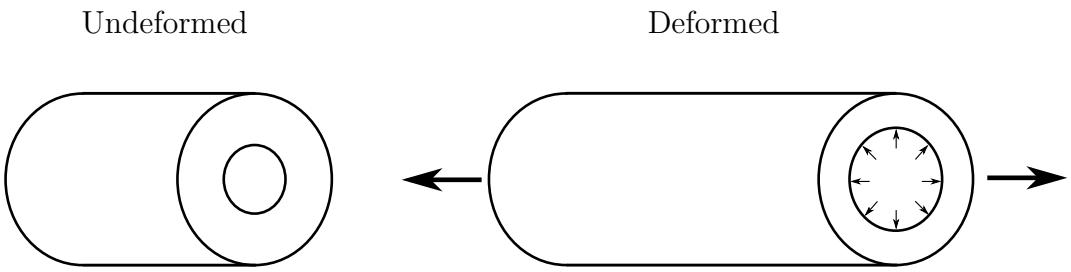

Figure 2.11: The undeformed and deformed annular cylinders. The deformation corresponds to an inflation accompanied by an axial stretch. We perform the deformation such that the outer radius remains constant.

case letters correspond to the deformed. The function $r(R)$ is the unknown radial displacement, which is dependent on the axial stretch and the choice of (nonlinear) elastic properties. When deriving the equations of small-on-large, we find it convenient to consider the undeformed radius as a function of the deformed $R(r)$. For the deformed and undeformed configurations, the inner radii will be denoted by R_0 and r_0 and the outer radii by R_1 and r_1. As mentioned previously, the outer radius remains unchanged so $R_1 = r_1$.

A deformation is most commonly characterised by its deformation gradient tensor, which is defined as the gradient of the deformed coordinates with respect to the undeformed coordinates

$$\mathbf{F} = \mathrm{Grad}\,\mathbf{x}. \tag{2.139}$$

In Cartesian coordinates, this is given by

$$F_{ij} = \mathrm{Grad}\,\mathbf{x} = \frac{\partial x_i}{\partial X_j}, \tag{2.140}$$

where the upper case G refers to the gradient with respect to the undeformed configuration. In cylindrical polar coordinates, the position vector is given by (2.131) and the deformation gradient tensor is given by

$$\mathbf{F} = \begin{pmatrix} \frac{\partial r}{\partial R} & \frac{1}{R}\left(\frac{\partial r}{\partial \Theta}\right) & \frac{\partial r}{\partial Z} \\ 0 & \frac{r}{R} & 0 \\ \frac{\partial z}{\partial R} & \frac{1}{R}\frac{\partial z}{\partial \Theta} & \frac{\partial z}{\partial Z} \end{pmatrix}. \tag{2.141}$$

In the example used here of an inflated and stretched annular cylinder, this simplifies

to

$$\mathbf{F} = \begin{pmatrix} \frac{\partial r}{\partial R} & 0 & 0 \\ 0 & \frac{r}{R} & 0 \\ 0 & 0 & \beta \end{pmatrix}. \tag{2.142}$$

It is common to decompose the deformation gradient tensor into the two forms

$$\mathbf{F} = \mathbf{V} \cdot \mathbf{R} = \mathbf{R} \cdot \mathbf{W}, \tag{2.143}$$

where $\mathbf{R}$ is the rotation tensor, $\mathbf{V}$ is the left stretch tensor and $\mathbf{W}$ is the right stretch tensor and the dot product of two second-order tensors gives the conventional matrix multiplication ($\mathbf{A} \cdot \mathbf{B} = A_{ij}B_{jk}$). The first form corresponds to performing a rigid body rotation followed by a stretch and the second form corresponds to performing a stretch followed by a rigid body rotation. The two stretch tensors have the same eigenvalues, λ_1, λ_2 and λ_3, which are referred to as the principal stretches of the deformation. The eigenvectors correspond to the principal axes. These are the three orthogonal directions along which the material experiences pure stretch. For a general inhomogeneous deformation, the principal axes are dependent on position. For the inhomogeneous deformation considered here, the principal axes remain the same at every point.

The left and right Cauchy-Green strain tensors are defined respectively as

$$\mathbf{B} = \mathbf{F} \cdot \mathbf{F}^T = \mathbf{V} \cdot \mathbf{V} \tag{2.144}$$

and

$$\mathbf{C} = \mathbf{F}^T \cdot \mathbf{F} = \mathbf{W} \cdot \mathbf{W}\ . \tag{2.145}$$

We may write the invariants of the Cauchy-Green strain tensors in terms of these principal stretches as

$$I_1 = \mathrm{tr}(\mathbf{B}) = \mathrm{tr}(\mathbf{C}) = \lambda_1^2 + \lambda_2^2 + \lambda_3^2, \tag{2.146}$$

$$I_2 = \frac{1}{2}\left(I_1^2 - \mathrm{tr}(\mathbf{B}^2)\right) = \frac{1}{2}\left(I_1^2 - \mathrm{tr}(\mathbf{C}^2)\right) = \lambda_1^2\lambda_2^2 + \lambda_1^2\lambda_3^2 + \lambda_2^2\lambda_3^2, \tag{2.147}$$

$$I_3 = \det(\mathbf{B}) = \det(\mathbf{C}) = \lambda_1^2\lambda_2^2\lambda_3^2\ . \tag{2.148}$$

These are called the strain invariants and will be used later in defining constitutive laws for specific materials. The third strain invariant corresponds to the infinitesimal

volume change at a point and is denoted by J. For an incompressible material, we have no volume change and therefore $J^2 = I_3 = 1$.

In the example of an annular cylinder, we apply no rigid body rotations, which implies that

$$\mathbf{F} = \mathbf{V} = \mathbf{W}. \tag{2.149}$$

The principal axes correspond to the radial, azimuthal and axial basis vectors and the principal stretches along these axes are given by the diagonal elements of $\mathbf{F}$ (see (2.142))

$$\lambda_r = \frac{\partial r}{\partial R}, \quad \lambda_\theta = \frac{r}{R}, \quad \lambda_z = \beta. \tag{2.150}$$

Through consideration of the conservation of energy, we can define the Cauchy stress, $\mathbf{T}$ in terms of the strain energy density. For a compressible material, the Cauchy stress is given by

$$\mathbf{T} = \frac{\mathbf{F}}{J} \cdot \frac{\partial W}{\partial \mathbf{F}}, \tag{2.151}$$

or in index notation

$$T_{ij} = \frac{F_{ik}}{J} \frac{\partial W}{\partial F_{jk}}. \tag{2.152}$$

For an incompressible material we have

$$\mathbf{T} = \mathbf{F} \cdot \frac{\partial W}{\partial \mathbf{F}} + Q\mathbf{I}, \tag{2.153}$$

where $\mathbf{I}$ is the identity matrix and Q is a Lagrange multiplier necessary to satisfy the incompressibility constraint (see [61] for details). The components of the Cauchy stress tensor are those stresses that act on the faces of an infinitesimal cube aligned with the axes. For example, the component T_{ij} gives the stress in the direction x_i on the face with normal in direction x_j. The function $W(I_1, I_2, I_3)$ is the strain energy function, which is dependent on the three strain invariants for an isotropic material. The form of this function is a constitutive relation that dictates how the material behaves.

We may also define the nominal stress, which gives the force relative to the undeformed configuration. This is defined for compressible materials as

$$\mathbf{S} = \frac{\partial W}{\partial \mathbf{F}}, \tag{2.154}$$

and for incompressible materials as

$$\mathbf{S} = \frac{\partial W}{\partial \mathbf{F}} + Q\mathbf{F}^{-1}. \tag{2.155}$$

Note that the relation between the Cauchy and nominal stress tensors is

$$\mathbf{T} = \frac{1}{J}\mathbf{F} \cdot \mathbf{S}. \tag{2.156}$$

Recall that the equation of motion in the absence of body forces is given by (2.85)

$$\text{div}\mathbf{T} = \rho\frac{\partial^2 \mathbf{U}}{\partial t^2}, \tag{2.157}$$

where $\mathbf{U} = \mathbf{x} - \mathbf{X}$ is the displacement from the reference configuration. Clearly, for a static deformation we obtain the equilibrium equation

$$\text{div}\mathbf{T} = 0. \tag{2.158}$$

2.4.3 Strain energy functions

The strain energy function relates a deformation to the amount of energy held in elastic potential. As mentioned above, it is dependent on the three strain invariants, or equivalently the principal stretches

$$W = W(I_1, I_2, I_3) = \hat{W}(\lambda_1, \lambda_2, \lambda_3). \tag{2.159}$$

For incompressible materials, we have $I_3 = J^2 = 1$, which implies that the strain energy function only depends on the first two invariants,

$$W = W(I_1, I_2). \tag{2.160}$$

During this thesis we make use of four different strain energy functions. Three are for an incompressible material and are the neo-Hookean, Mooney-Rivlin and a simplified version of the Fung strain energy function. For compressible materials, we consider the strain energy function presented by Levinson and Burgess [49].

Neo-Hookean

For an incompressible neo-Hookean material, the strain energy function is given in [61], that is,

$$W = \frac{\mu}{2}(I_1 - 3) = \frac{\mu}{2}(\lambda_r^2 + \lambda_\theta^2 + \lambda_z^2 - 3). \tag{2.161}$$

This is one of the simplest strain energy functions since it involves just the first strain invariant as a linear function. This strain energy function evolved from Hooke's law

(hence the name) but gives nonlinear stress-strain behaviour for large deformations. This is usually the first approximation used when studying a problem in nonlinear elasticity.

Mooney-Rivlin

Next we have the Mooney-Rivlin strain energy function. This model is typically used to describe rubber like materials and is said to be more realistic than the neo-Hookean model. The strain energy function for a Mooney-Rivlin material is given in [61], that is,

$$W = \frac{\mu}{2}\left(S_1(\lambda_r^2 + \lambda_\theta^2 + \lambda_z^2 - 3) + S_2(\lambda_r^2\lambda_\theta^2 + \lambda_r^2\lambda_z^2 + \lambda_\theta^2\lambda_z^2 - 3)\right), \tag{2.162}$$

where S_1 and S_2 are material constants, typically found empirically. In order to be consistent with linear elasticity, the constraint that $S_1 + S_2 = 1$ must hold. Note that when $S_1 = 1$ ($S_2 = 0$), we recover the neo-Hookean case. We can think of the Mooney-Rivlin strain energy function as an extension of the neo-Hookean model involving the second strain invariant.

Fung

Since the Mooney-Rivlin strain energy function is essentially an extension of the Neo-Hookean, we will also consider a form of strain energy function that exhibits completely different behaviour. The chosen form is a simplified version of the Fung strain energy function given in [21], that is,

$$W = \frac{\mu}{2}\left(e^Q - 1\right), \tag{2.163}$$

where

$$Q = E_r^2 + E_\theta^2 + E_z^2, \tag{2.164}$$

$$E_k = \frac{1}{2}\left(\lambda_k^2 - 1\right) \qquad \text{for} \quad k = r, \theta, z. \tag{2.165}$$

This strain energy function is often used to model biological tissues such as arteries.

Levinson and Burgess

For compressible materials, we choose to use the Levinson and Burgess strain energy function, given by (see [49])

$$W = \frac{\mu}{2}(I_1 - 3) + \frac{\lambda + \mu}{2}(I_3 - 1) - (\lambda + 2\mu)(I_3^{1/2} - 1). \tag{2.166}$$

This strain energy function was chosen as it is a compressible extension to the neo-Hookean strain energy function. When finding deformations with this strain energy function, little progress can be made analytically; for this reason we must use numerical techniques.

2.4.4 Incremental deformation

We study how a large pre-stress affects the propagation of waves by using the small-on-large technique. This method involves a linearisation for small displacements about a pre-stressed state. We follow the notation used in [76]. For more details on the derivation, please see [61] and [13].

We consider a deformation from the reference configuration to a new configuration (which we call the perturbed configuration) where the position vector is given by $\bar{\mathbf{x}}$. The difference between deformed and the perturbed configuration is denoted by

$$\mathbf{u} = \bar{\mathbf{x}} - \mathbf{x}, \tag{2.167}$$

where we assume that this perturbation is in some sense small.

We next examine the deformation gradient tensor of the perturbed configuration. First let us define $\mathbf{f}$

$$\mathbf{f} = \operatorname{grad} \bar{\mathbf{x}}, \tag{2.168}$$

where the lower case g refers to the gradient with respect to the deformed configuration. The tensor $\mathbf{f}$ is the gradient of the perturbed configuration with respect to the deformed position $\mathbf{x}$. The deformation gradient tensor in the perturbed configuration is given by

$$\bar{\mathbf{F}} = \operatorname{Grad} \bar{\mathbf{x}} = \mathbf{f} \cdot \mathbf{F}. \tag{2.169}$$

We find it useful to define the gradient of the displacement, given by

$$\boldsymbol{\gamma} = \operatorname{grad} \mathbf{u} = \operatorname{grad} \bar{\mathbf{x}} - \operatorname{grad} \mathbf{x} = \mathbf{f} - \mathbf{I}, \tag{2.170}$$

giving

$$\mathbf{f} = \boldsymbol{\gamma} + \mathbf{I}. \tag{2.171}$$

We note that, assuming the displacement is small, we have

$$|\boldsymbol{\gamma}| = (\boldsymbol{\gamma} : \boldsymbol{\gamma}^T)^{1/2} \ll 1, \tag{2.172}$$

where : denotes a double contraction of two tensors, defined in index notation by

$$(\mathbf{A} : \mathbf{B})_{ab\ldots il\ldots z} = A_{ab\ldots jk} B_{kjl\ldots z}, \tag{2.173}$$

where repeated (dummy) indices are summed over.

In the perturbed configuration we assume that the nominal stress tensor is given by

$$\bar{\mathbf{S}} = \mathbf{S} + \mathbf{s}, \tag{2.174}$$

where $\mathbf{S}$ is the stress due to the initial deformation and $\mathbf{s}$ is the stress due to the perturbation. Noting that

$$\bar{\mathbf{S}} = \bar{\mathbf{S}}(\bar{\mathbf{F}}) = \bar{\mathbf{S}}(\mathbf{F} + \boldsymbol{\gamma} \cdot \mathbf{F}), \tag{2.175}$$

we find the stress perturbation due to the small amplitude waves by taking a Taylor series of $\bar{\mathbf{S}}$ about $\mathbf{F}$, giving

$$\bar{\mathbf{S}} = \mathbf{S}(\mathbf{F}) + \frac{\partial \mathbf{S}}{\partial \mathbf{F}} : (\boldsymbol{\gamma} \cdot \mathbf{F}) + \ldots, \tag{2.176}$$

where the partial derivative gives a fourth-order tensor, which we denote $\mathbf{L}$. In index notation, the component L_{ijkl} is defined as

$$L_{ijkl} = \frac{\partial S_{ij}}{\partial F_{lk}} = \frac{\partial^2 W}{\partial F_{ji} \partial F_{lk}}. \tag{2.177}$$

We conclude that the perturbation to the stress is given by

$$\mathbf{s} = \mathbf{L} : (\boldsymbol{\gamma} \cdot \mathbf{F}). \tag{2.178}$$

For an incompressible material, we have

$$\mathbf{s} = \mathbf{L} : (\boldsymbol{\gamma}\mathbf{F}) + q\mathbf{F}^{-1} - Q\boldsymbol{\gamma} \cdot \mathbf{F}^{-1}, \tag{2.179}$$

where q is the perturbation to the Lagrange multiplier Q.

It is convenient to define the push forward of the nominal stress perturbation $\boldsymbol{\zeta}$

$$\boldsymbol{\zeta} = \frac{1}{J}\,\mathbf{F}\cdot\mathbf{s} \tag{2.180}$$

and in index notation

$$\zeta_{ij} = \frac{1}{J}\,F_{im}\,L_{mjnl}\,\gamma_{lk}\,F_{kn}. \tag{2.181}$$

This gives

$$\boldsymbol{\zeta} = \mathbf{M} : \boldsymbol{\gamma}, \tag{2.182}$$

where $\mathbf{M}$ is the pre-stressed fourth-order elasticity tensor for small deformations. In index notation, $\mathbf{M}$ is given by

$$M_{ijkl} = \frac{1}{J}\,L_{mjnl}\,F_{im}\,F_{kn} = \frac{1}{J}\frac{\partial^2 W}{\partial F_{jm}\partial F_{ln}}F_{im}F_{kn}. \tag{2.183}$$

We are now able to write the equation of motion for small amplitude waves. From (2.85), the equation of motion in the perturbed configuration is

$$\overline{\operatorname{div}}\,\bar{\mathbf{T}} = \bar{\rho}\frac{\partial^2\bar{\mathbf{U}}}{\partial t^2}, \tag{2.184}$$

where $\overline{\operatorname{div}}$ gives the divergence with respect to the perturbed configuration, $\bar{\mathbf{U}} = \mathbf{U}+\mathbf{u}$ is the total displacement (i.e. the sum of the static and perturbed displacements) and $\bar{\mathbf{T}}$ is the total stress.

Because $\mathbf{U}$ is the static displacement and has no time dependence, we get

$$\frac{\partial^2\bar{\mathbf{U}}}{\partial t^2} = \frac{\partial^2\mathbf{u}}{\partial t^2}. \tag{2.185}$$

To further simplify matters, we note that for small displacements $\bar{\rho} = \rho + O(|\mathbf{u}|)$. This means, since we neglect terms of order $O(|\mathbf{u}|^2)$, we have

$$\overline{\operatorname{div}}\,\bar{\mathbf{T}} = \rho\frac{\partial^2\mathbf{u}}{\partial t^2}. \tag{2.186}$$

It can be shown that this is equivalent to

$$\operatorname{div}\boldsymbol{\zeta} = \rho\frac{\partial^2\mathbf{u}}{\partial t^2}, \tag{2.187}$$

details of which can be found in [76]. Equation (2.187) is the set of equations of motion governing incremental waves and will be used in later chapters to study pre-stressed media. For a more detailed derivation of the equations of elasticity, see one of the many books on the subject, for example Ogden [61], Fu and Ogden [20] and Green and Zerna [29].

Chapter 3

Pulse reflection from a semi-infinite array of point masses on a string

3.1 Introduction

In this chapter, we discuss the reflection problem for an array of point masses on a string. Recall that we refer to these point masses as "beads". The configuration of periodic beads on a string lends itself nicely to elegant experiments which are easy to run and inexpensive to set up. The paper by Gomez et al. [27] investigates the normal modes of a beaded string and includes some very nice photographs. Good agreement was found between the expected theoretical modes and those observed experimentally. Similar problems include a string with concentrated masses on elastic supports, investigated by Vedenova et al. [89] and more recently by Richoux [70]. In the latter of these two papers, the reflection and transmission coefficients from a finite number of beads are computed. This work relies largely on numerical methods in obtaining results.

Disordered or near-periodic spacing is another area of interest and has been studied by Martin [54], Maurel et al. [56], and Ottarsson and Pierre [64]. Martin looked at the reflection and transmission coefficients from a finite series of beads and used this to find approximate reflection and transmission coefficients for a random series of beads which is almost periodic. Maurel et al. found an effective wavenumber for a perturbed periodic medium. At low frequencies, it is shown to match extremely well with numerical simulations. Ottarsson and Pierre used transfer matrices to study the

beaded string. Localised vibrations were observed by varying either the spacing of the beads or their mass.

Although the majority of analysis is carried out for a single frequency, some studies have considered the time domain solution via numerical simulations. For example, the finite-difference time-domain method is used by Oh and Escuti [62], and Veysoglu et al. [90]. Both use a similar technique involving periodic boundary conditions to model the structure using only one period. This technique allows the computation of waves at oblique angles and is found to match well with other techniques such as the frequency domain technique. Missing from the literature is an analytic study of time-dependent propagation of waves in one-dimensional periodic structures.

Analytical work was carried out by Karlsson and Kreider [39] who utilised wave splitting to analyse the transient properties of electromagnetic waves. In further work, Karlsson and Stewart [40] made use of wave propagators which essentially model the reflection and transmission of a pulse from each boundary. This technique is useful for broad-band pulses.

The set up we will consider here will be a set of periodically spaced point masses on half of the string as pictured in figure 3.1. The first bead will be positioned at $x = 0$ and the spacing of the beads will be unity. Again, because of our dimensionless scaling introduced in equation (2.8) this corresponds to a physical spacing of ℓ. The motivation behind studying this geometry is the fact that it is possible to find the exact reflection coefficient in this case. We find the exact solution in the context of an incident pulse by taking the Fourier transform of the input to find the spectral composition. We will multiply this by the frequency dependent reflection coefficient and then take the inverse Fourier transform to find the reflected pulse.

3.2 Constructing the reflection of a pulse

We begin by constructing the solution for the reflection of an incoming pulse. We find the frequency components of the incoming wave using the Fourier transform. We know that each frequency component will be reflected according to some function $R(\epsilon)$. Details of this method have been omitted for the time-being. A more rigorous derivation for a similar problem is given in the next chapter.

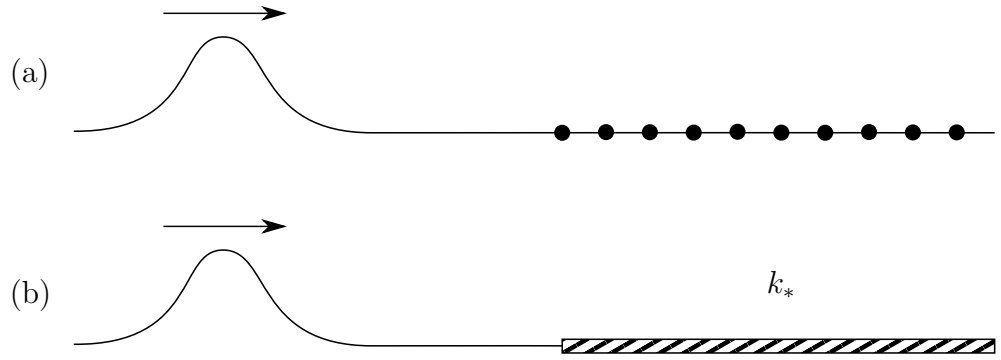

Figure 3.1: A pulse on a string encountering (a) a series of periodic point masses and (b) an effective material with wavenumber k_*.

Writing the displacement on the left-hand side of the string in terms of nondimensional quantities, we have

$$u^-(x,t) = u_{\text{in}}(x,t) + u_R(x,t) = h(x-t) + u_R(x+t), \tag{3.1}$$

where $h(x-t)$ is the prescribed incoming pulse and $u_R(x+t)$ is the reflected pulse to be found. Taking the Fourier transform (defined by (2.14)) of the input, $u_{\text{in}}(x,t)$, we get

$$H(\epsilon) = \int_{-\infty}^{\infty} h(x-t)e^{i\epsilon(x-t)}d(x-t),$$

which, using the change of variables $u = x - t$, gives

$$H(\epsilon) = \int_{-\infty}^{\infty} h(u)e^{i\epsilon u}du. \tag{3.2}$$

Note that here,

$$e^{i\epsilon u} = e^{i\epsilon(x-t)} \tag{3.3}$$

represents a plane wave travelling from left to right.

The reflected part of the solution is now given by the inverse Fourier transform with the integrand modulated by the reflection coefficient

$$u_R(x+t) = \frac{1}{2\pi}\int_{-\infty}^{\infty} R(\epsilon)H(\epsilon)e^{-i\epsilon(x+t)}d\epsilon, \tag{3.4}$$

where the plane waves are now travelling from right to left. This integral describes the reflected pulse given a specific input and reflection coefficient. In general it is not possible to perform the integration exactly to determine an analytical solution. However, we will later describe how to obtain a neat solution when using the exact reflection coefficient.

3.3 Reflection from an effective medium

We now find the reflection coefficient assuming that we can take a homogeneous effective medium. Consider the heterogeneous portion of string on the right-hand side to be given by the effective medium characterised by a wavenumber k_*. For the case considered here of a string with beads, we take the effective wavenumber to be the one for the infinite case, given by equation (2.71)

$$\cos(k_*) = \cos(\epsilon) - \frac{M\epsilon}{2}\sin(\epsilon). \tag{3.5}$$

Note that this wavenumber is exact rather than an approximation usually obtained in homogenisation theory. This wavenumber holds for all of the stop and pass band frequencies of the infinite beaded string.

To find the reflection coefficient we consider a time-harmonic solution (given by $u(x,t) = U(x)e^{-i\epsilon t}$) and propose the spatial form

$$U(x) = \begin{cases} e^{i\epsilon x} + Re^{-i\epsilon x} & \text{if } x \leq 0 \\ Te^{ik_* x} & \text{if } x \geq 0, \end{cases} \tag{3.6}$$

where R and T are the effective reflection and transmission coefficients. As usual, we have used a unit bead spacing in nondimensional variables (see (2.8)). The form given by (3.6) consists of a wave of unit amplitude incoming from the left, a reflected wave travelling to the left with wavenumber ϵ and a transmitted wave travelling to the right with effective wavenumber k_*.

To find the reflection and transmission coefficients in this case, we choose to apply the conditions of continuity of displacement and slope at the origin, given by

$$U(x)\Big|_{0^-}^{0^+} = 0,$$

$$\frac{\partial U}{\partial x}(x)\Big|_{0^-}^{0^+} = 0.$$

The reasoning for choosing these conditions is based on the assumption that the right hand side is given by a string with effective wavenumber k_*. Recall from the background section 2.1.4, that the continuity of force in a string corresponds to continuity of slope. In reality, the inhomogeneous string will not behave like an effective medium; we assume it does here in order to highlight the problems with treating a heterogeneous medium as an effective one when boundary effects are important.

Applying the ansatz in (3.6) to these conditions give

$$1 + R = T, \tag{3.7}$$

$$i - iR = i\gamma T, \tag{3.8}$$

where we have defined $\gamma(\epsilon) = k_*(\epsilon)/\epsilon$ as the reciprocal of the effective phase speed. Solving (3.7) and (3.8) for R and T gives the effective reflection and transmission coefficients

$$R = \frac{1-\gamma}{1+\gamma}, \tag{3.9}$$

$$T = \frac{2}{1+\gamma}. \tag{3.10}$$

Equations (3.9) and (3.9) should in theory give the reflection and transmission at a given wavelength. There are in fact fundamental issues with trying to do this, which will be discussed later in the chapter. One of these issues is the multivaluedness of the effective wavenumber k_*. Since we can choose any number of branches for this function, the reflection and transmission can also take multiple values. As discussed in the background section 2.2, we can make this function single-valued by imposing the requirement that it approaches the nondispersive case in the zero mass limit. We assume that k_* (and thus γ) have this single-valued form.

Since we are interested in transient problems, we will now go on to discuss the reflection of pulses. In order to do this, we decompose the input into its frequency components. Each of those harmonic components are reflected using the above coefficients. The reflection may then be reconstructed using the inverse Fourier transform.

3.4 The exact reflection coefficient for a semi-infinite array of point masses

In order to determine the reflection from a semi-infinite array of beads, we consider the set up shown in figure 3.1. We look for the reflection and transmission coefficient due to a harmonic wave of unit amplitude. The method described is given in more detail in [1]. Here we will give a brief overview of the method and then analyse the result.

We start by writing down the total displacement, given by

$$u_{\text{tot}}(x) = \begin{cases} u(x) + e^{i\epsilon x} - e^{-i\epsilon x}, & \text{if } x \leq 0, \\ u(x), & \text{if } x \geq 0. \end{cases} \tag{3.11}$$

The $e^{i\epsilon x}$ term is the forcing term and constitutes an incoming harmonic wave from the left. The $-e^{-i\epsilon x}$ term is included to make $u(x)$ continuous at the origin which in turn makes the algebra slightly simpler. By considering the jump condition (2.61) at the origin, we find the Green's function for the first bead

$$u_1(x) = \left(\frac{iM\epsilon}{2}u(0) + 1\right) e^{i\epsilon|x|}. \tag{3.12}$$

As was done in the background chapter, we find the total solution by summing the Green's functions given by equation (2.62) for each bead. In this case the sum starts from zero and includes the Green's function for the bead at the origin

$$u(x) = \frac{iM\epsilon}{2} \sum_{n=0}^{\infty} u(x_n) e^{i\epsilon|x-x_n|} + e^{i\epsilon|x|}. \tag{3.13}$$

This solution is implicit since it depends on the displacements at each bead position.

We are unable to solve this as in section 2.2 by assuming a Bloch-Floquet solution because there is no translational symmetry of the problem. Instead, the Wiener-Hopf technique may be used. This technique is a common tool used for such semi-infinite problems. For more details, please see [60]. Briefly, the Wiener-Hopf technique is commonly used to solve integral equations of the form

$$f(x) + \lambda \int_0^{\infty} k(x-y) f(y) dy = g(x), \quad 0 \leq x < \infty \tag{3.14}$$

for some unknown $f(x)$, given $g(x)$ defined for $0 \leq x < \infty$ and $k(x)$ defined for all $x \in \mathbb{R}$. This equation may be Fourier transformed into the general form of a Wiener-Hopf equation, given by

$$\lambda K(\alpha) U^+(\alpha) + U^-(\alpha) = P(\alpha), \quad \mu < \Im(\alpha) < \lambda, \tag{3.15}$$

where $K(\alpha)$ is a known function containing the "physics" of the problem and $P(\alpha)$ gives the chosen forcing. This equation is defined on a strip of the complex α-plane given by $\mu < \Im(\alpha) < \lambda$. The functions $U^+(\alpha)$ and $U^-(\alpha)$ are sought, but are known to be analytic in upper and lower domains respectively. Alternatively, the equation

can be arranged so that + denotes functions analytic inside and on the unit circle ($|\alpha| \leq 1$), and − denotes functions analytic outside and on the unit circle ($|\alpha| \geq 1$). The intersection of these two domains consists of the strip over which the equation is defined and the union of the two regions makes up the entire complex plane.

The solution technique involves separating the equation into parts that have different regions of analyticity. Begin by splitting $K(\alpha)$ as a product decompositions such that $K(\alpha) = K^+(\alpha)K^-(\alpha)$, where $\pm$ denote the above analyticity properties. After dividing by $K^-(\alpha)$ we get

$$K^+(\alpha)U^+(\alpha) + \frac{U^-(\alpha)}{K^-} = \frac{P(\alpha)}{K^-}, \quad \mu < \Im(\alpha) < \lambda, \tag{3.16}$$

By performing a sum split to the term on the right-hand defined by

$$\frac{P(\alpha)}{K^-} = Q^-(\alpha) + Q^+(\alpha), \tag{3.17}$$

we can isolate the terms analytic inside or outside the unit circle, i.e.

$$K^+(\alpha)U^+(\alpha) - Q^+(\alpha) = -\frac{U^-(\alpha)}{K(\alpha)} + Q^-(\alpha), \quad \mu < \Im(\alpha) < \lambda. \tag{3.18}$$

Since both sides of this equation are analytic along the strip defined by $\mu < \Im(\alpha) < \lambda$, we can use analytic continuation to extend the domain of the equation to the whole complex plane. We can therefore set this equation equal to an entire function which we call $E(\alpha)$, say,

$$K^+(\alpha)U^+(\alpha) - Q^+(\alpha) = -\frac{U^-(\alpha)}{K(\alpha)} + Q^-(\alpha) \equiv E(\alpha), \quad \mu < \Im(\alpha) < \lambda. \tag{3.19}$$

Provided we are able to find $E(\alpha)$ we can use this equation to find the two unknowns $U^-(\alpha)$ and $U^+(\alpha)$.

Return to equation (3.13) and we see that it may be solved as outlined in [1]. To obtain a Wiener-Hopf equation in the form of (3.15) from the implicit solution (3.13) we start by sampling at the mth bead position

$$u(m) = \frac{iM\epsilon}{2} \sum_{n=0}^{\infty} u(n) e^{i\epsilon|m-n|} + e^{i\epsilon|m|}. \tag{3.20}$$

We then take the z transform, defined in the introduction by equation (2.16), giving

$$\sum_{m=-\infty}^{\infty} u(m) z^m = \frac{iM\epsilon}{2} \sum_{m=-\infty}^{\infty} \sum_{n=0}^{\infty} u(n) z^m e^{i\epsilon|m-n|} + \sum_{m=-\infty}^{\infty} z^m e^{i\epsilon|m|}. \tag{3.21}$$

The sum on the left-hand side of (3.21) may be split into two parts

$$V^+(z) = \sum_{m=0}^{\infty} u(m) z^m, \tag{3.22}$$

$$V^-(z) = \sum_{m=-\infty}^{-1} u(m) z^m. \tag{3.23}$$

We add a small imaginary part to ϵ to aid convergence,

$$\epsilon \to \epsilon + i\mu, \tag{3.24}$$

and it is then possible to show that $V^+(z)$ is analytic inside an inner region defined by the disk

$$|z| < e^{\mu} \approx 1 + \mu. \tag{3.25}$$

Similarly, the function $V^-(z)$ is analytic in an outer region defined by

$$|z| > e^{-\mu} \approx 1 - \mu. \tag{3.26}$$

The overlapping region of analyticity is the annulus $e^{-\mu} < |z| < e^{\mu}$.

By writing the geometric series in the form

$$\sum_{u=0}^{\infty} z^u e^{i\epsilon u} = \frac{1}{1 - z e^{i\epsilon}} \tag{3.27}$$

and applying some rearrangements, equation (3.21) may be converted into the form of a Wiener-Hopf equation

$$V^-(z) + K(z) V^+(z) = \frac{e^{i\epsilon}}{z - e^{i\epsilon}} - \frac{e^{-i\epsilon}}{z - e^{-i\epsilon}}, \tag{3.28}$$

where

$$\begin{aligned} K(z) &= \frac{z^2 - 2z\left(\cos(\epsilon) - \frac{M\epsilon}{2}\sin(\epsilon)\right) + 1}{(z - e^{i\epsilon})(z - e^{-i\epsilon})}. \\ &= \frac{z^2 - 2z\cos(k_*) + 1}{(z - e^{i\epsilon})(z - e^{-i\epsilon})} \end{aligned} \tag{3.29}$$

It is interesting to note that the exact wavenumber for the infinite case, given by (2.71), appears in the semi-infinite problem.

As mentioned previsouly we split the function $K(z)$ as a product decomposition. This gives

$$K^+(z) = \frac{z - e^{-ik_*}}{z - e^{-i\epsilon}} \tag{3.30}$$

$$K^-(z) = \frac{z - e^{ik_*}}{z - e^{i\epsilon}} \tag{3.31}$$

Note that all of the poles and zeroes of $K^+(z)$ are outside the unit circle and the poles and zeroes of $K^-(z)$ are inside the unit circle. Dividing equation (3.28) by $K^-(z)$, we obtain

$$\frac{V^-(z)}{K^-(z)} + K^+(z)V^+(z) = \left(\frac{e^{i\epsilon}}{z-e^{ik_*}}\right)^- - \left(\frac{z-e^{i\epsilon}}{z-e^{ik_*}}\right)^- \left(\frac{e^{-i\epsilon}}{z-e^{-i\epsilon}}\right)^+, \tag{3.32}$$

where the superscript plus and minus indicate analyticity within and outside the unit circle respectively.

All that remains is to split the last term in (3.32). This can be done by pole removal, giving

$$\begin{aligned}\left(\frac{z-e^{i\epsilon}}{z-e^{ik_*}}\right)^- \left(\frac{e^{-i\epsilon}}{z-e^{-i\epsilon}}\right)^+ &= \left(\frac{e^{-i\epsilon}}{z-e^{-i\epsilon}}\left(\frac{z-e^{i\epsilon}}{z-e^{ik_*}} - \frac{e^{-i\epsilon}-e^{i\epsilon}}{e^{-i\epsilon}-e^{ik_*}}\right)\right)^- \\ &\quad + \left(\frac{e^{-i\epsilon}}{z-e^{-i\epsilon}}\ \frac{e^{-i\epsilon}-e^{i\epsilon}}{e^{-i\epsilon}-e^{ik_*}}\right)^+.\end{aligned} \tag{3.33}$$

Our Wiener-Hopf equation may now be split into two parts, one analytic inside the unit circle and one analytic outside.

$$\begin{aligned}\frac{V^-(z)}{K^-(z)} - \left(\frac{e^{i\epsilon}}{z-e^{ik_*}}\right)^- + \left(\frac{e^{-i\epsilon}}{z-e^{-i\epsilon}}\left(\frac{z-e^{i\epsilon}}{z-e^{ik_*}} - \frac{e^{-i\epsilon}-e^{i\epsilon}}{e^{-i\epsilon}-e^{ik_*}}\right)\right)^- \\ = -K^+(z)V^+(z) + \left(\frac{e^{-i\epsilon}}{z-e^{-i\epsilon}}\ \frac{e^{-i\epsilon}-e^{i\epsilon}}{e^{-i\epsilon}-e^{ik_*}}\right)^+ \equiv E(z)\end{aligned} \tag{3.34}$$

Note that both sides are analytic on the unit circle itself so we can use analytic continuation to equate each site to the entire function $E(z)$.

From the definition of $V^-(z)$ given in equation (3.23), we see that

$$V^-(z) = O(z^{-1}) \quad \text{as} \quad |z| \to \infty \tag{3.35}$$

and therefore the left hand side of (3.34) goes to zero as $|z| \to \infty$. Using Liouville's theorem we can infer that

$$E(z) = 0. \tag{3.36}$$

This gives us the solution in the z domain

$$V^+(z) = \frac{e^{-i(\epsilon+k_*)/2}\sin(\epsilon)}{\sin\left((\epsilon+k_*)/2\right)(z-e^{-ik_*})}, \tag{3.37}$$

$$V^-(z) = \frac{e^{i\epsilon}}{z-e^{i\epsilon}} - \frac{e^{-i\epsilon}}{z-e^{-i\epsilon}}\left(1 - \frac{e^{i(\epsilon-k_*)/2}\sin(\epsilon)}{\sin\left((\epsilon+k_*)/2\right)}\frac{(z-e^{ik_*})}{(z-e^{i\epsilon})}\right). \tag{3.38}$$

Then, by evaluating the inverse z transform given by (2.17) we find the solution in each domain to be

$$u(m) = \frac{e^{-i(\epsilon-k_*)/2}\sin(\epsilon)}{\sin((\epsilon+k_*)/2)}e^{ik_*m} \quad \text{for } m \geq 0, \tag{3.39}$$

$$u(m) = \frac{e^{-i\epsilon}\sin((\epsilon-k_*)/2)}{\sin((\epsilon+k_*)/2)}e^{-i\epsilon m} + e^{-i\epsilon m} \quad \text{for } m \leq 0. \tag{3.40}$$

Note that for $m \leq 0$, we may replace the discrete m by x since the string is homgeneous. The same cannot be said for $m \geq 0$ but equation (3.13) may be used to find the solution anywhere on the string. We are thus able to give the transmission and reflection coefficients for the harmonic problem to be

$$T = \frac{e^{-i(\epsilon-k_*)/2}\sin(\epsilon)}{\sin((\epsilon+k_*)/2)}, \tag{3.41}$$

$$R = \frac{e^{-i\epsilon}\sin((\epsilon-k_*)/2)}{\sin((\epsilon+k_*)/2)}. \tag{3.42}$$

The coefficients found here are exact. They may be used to test the validity of the effective ones given in equations (3.9) and (3.10).

3.5 Comparison of the reflection coefficients

We are now in a position to compare the reflection coefficient from the homogenised material to the exact one. We expect the two forms of reflection coefficient to agree when we take the homogenization limit $\epsilon \to 0$. This can be seen to be true by taking the expansion of (3.42) for small ϵ

$$R = \frac{(1-i\epsilon+O(\epsilon^2))((\epsilon-k_*)/2+O(\epsilon^2))}{(\epsilon+k_*)/2+O(\epsilon^2)} \approx \frac{1-\gamma}{1+\gamma}, \tag{3.43}$$

where $\gamma = k_*/\epsilon$. This is to be expected since in the homogenisation limit, long wavelengths only see the averaged properties of a material.

In figure 3.2 the modulus of the exact reflection coefficient has been plotted alongside the effective one, given by (3.9). Note that for the effective coefficient, the branch of k_* has been chosen to be consistent with figure (2.5). The first point to note is that in some regions the exact reflection coefficients magnitude is precisely one. It should not come as a surprise that these regions coincide with the imaginary part of the effective wavenumber being non-zero. Since these regions are stop bands, all energy

must be reflected. It should also be noted that as ϵ increases, more of the energy is reflected. This is in agreement with the effective wavenumber.

The reflection coefficient agree for small ϵ, as can be seen, but soon the two solutions diverge. What is of note is that for large ϵ it seems that the effective material predicts that none of the energy is reflected which is in disagreement with the exact reflection coefficient. This implies that for other problems, where we cannot solve for the reflection coefficient exactly, there is no obvious way to find the reflection and transmission coefficients.

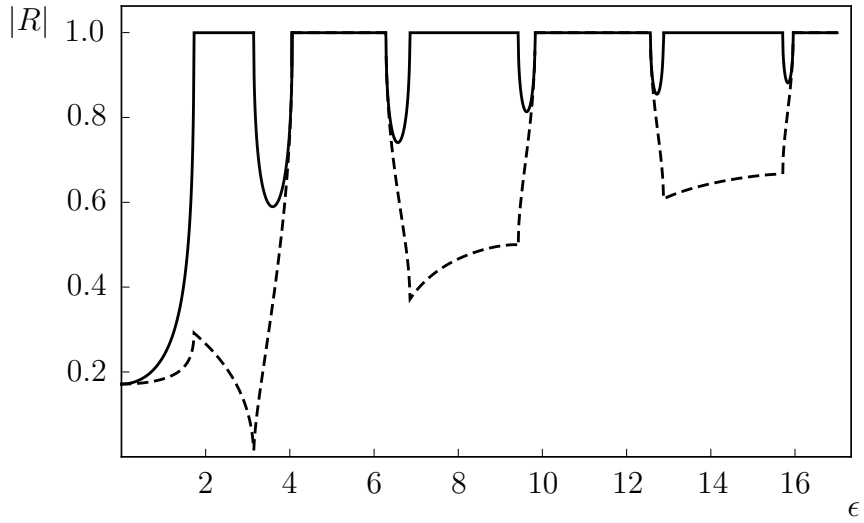

Figure 3.2: The comparison between the exact reflection coefficient and that obtained by assuming the beads can be treated as an effective medium. The exact reflection coefficient is given by the solid line and the effective term by the dashed line.

There is a clear issue with treating periodic or other inhomogeneous materials as effectively homogeneous in the manner described above. An understanding of how waves behave inside a material does not give us the full story. The question remains how waves interact with boundaries of periodic media. It is common practice to use experiments such as the split Hopkinson bar [51] to measure the reflection from an incoming pulse. In this case the input will broadband and will therefore contain frequencies in the regime where homogenisation is not applicable. When it comes down to transient behaviour, if we are to compare the theory with experiments then we will be limited to cases where we can solve for the exact reflection and transmission, especially in the high-frequency regime. We note that some work has been carried out calculating the reflection from heterogeneous media numerically[84].

3.6 Exact pulse reflection

Since $R(\epsilon)$ has been found exactly and is given by (3.42), this can be inserted in (3.4) to give

$$u_R(x,t) = \frac{1}{2\pi}\int_{-\infty}^{\infty} \frac{e^{-i\epsilon}\sin(\epsilon(1-\gamma(\epsilon))/2)}{\sin(\epsilon(1+\gamma(\epsilon))/2)} \left[\int_{-\infty}^{\infty} h(u)e^{i\epsilon u}du\right] e^{-i\epsilon(x+t)}d\epsilon. \tag{3.44}$$

This expression gives the reflected pulse anywhere on the left-hand side ($x < 0$). It is not immediately clear how to evaluate this integral so some investigation into the singularity structure of the integrand is made.

We can begin to make progress with the above integral given by equation (3.44) through investigation of the singularity structure in the complex plane. Clearly, the exponential term is analytic. We therefore know that the singularities come from the sine term in (3.44) as well as possible singularities from the Fourier transform of the input. In order to see the singularity structure, we must rearrange the sine term in (3.44). To do this, we use the fact that

$$\frac{\sin\left(\frac{\epsilon}{2}-\frac{\gamma\epsilon}{2}\right)}{\sin\left(\frac{\epsilon}{2}+\frac{\gamma\epsilon}{2}\right)} = \frac{\sin\left(\frac{\epsilon}{2}\right)\cos\left(\frac{\gamma\epsilon}{2}\right)-\cos\left(\frac{\epsilon}{2}\right)\sin\left(\frac{\gamma\epsilon}{2}\right)}{\sin\left(\frac{\epsilon}{2}\right)\cos\left(\frac{\gamma\epsilon}{2}\right)+\cos\left(\frac{\epsilon}{2}\right)\sin\left(\frac{\gamma\epsilon}{2}\right)},$$

which, after multiplying by a factor of $(\cos(\gamma\epsilon/2))^{-1}$ on the top and bottom of the right-hand side, gives

$$\begin{aligned}
\frac{\sin\left(\frac{\epsilon}{2}-\frac{\gamma\epsilon}{2}\right)}{\sin\left(\frac{\epsilon}{2}+\frac{\gamma\epsilon}{2}\right)} &= \frac{\sin\left(\frac{\epsilon}{2}\right)(1+\cos(\gamma\epsilon))-\cos\left(\frac{\epsilon}{2}\right)\sin(\gamma\epsilon)}{\sin\left(\frac{\epsilon}{2}\right)(1+\cos(\gamma\epsilon))+\cos\left(\frac{\epsilon}{2}\right)\sin(\gamma\epsilon)} \\
&= \frac{\sin\left(\frac{\epsilon}{2}\right)-\cos\left(\frac{\epsilon}{2}\right)\frac{\sqrt{1-\cos^2(\gamma\epsilon)}}{1+\cos(\gamma\epsilon)}}{\sin\left(\frac{\epsilon}{2}\right)+\cos\left(\frac{\epsilon}{2}\right)\frac{\sqrt{1-\cos^2(\gamma\epsilon)}}{1+\cos(\gamma\epsilon)}} \\
&= \frac{\sin\left(\frac{\epsilon}{2}\right)-\cos\left(\frac{\epsilon}{2}\right)\sqrt{\frac{1-\cos(\gamma\epsilon)}{1+\cos(\gamma\epsilon)}}}{\sin\left(\frac{\epsilon}{2}\right)+\cos\left(\frac{\epsilon}{2}\right)\sqrt{\frac{1-\cos(\gamma\epsilon)}{1+\cos(\gamma\epsilon)}}} \\
&= \frac{\sin\left(\frac{\epsilon}{2}\right)\sqrt{1+\cos(\gamma\epsilon)}-\cos\left(\frac{\epsilon}{2}\right)\sqrt{1-\cos(\gamma\epsilon)}}{\sin\left(\frac{\epsilon}{2}\right)\sqrt{1+\cos(\gamma\epsilon)}+\cos\left(\frac{\epsilon}{2}\right)\sqrt{1-\cos(\gamma\epsilon)}}.
\end{aligned}$$

Now that we have isolated $\cos(\gamma\epsilon)$, we can use the dispersion relation in equation (2.71). It is possible to eliminate the square root from the bottom by multiplying top and bottom by

$$\sin\left(\frac{\epsilon}{2}\right)\sqrt{1+\cos(\gamma\epsilon)}-\cos\left(\frac{\epsilon}{2}\right)\sqrt{1-\cos(\gamma\epsilon)}.$$

After some simple rearrangement of the above fraction, the reflection coefficient becomes

$$R(\epsilon) = \frac{2e^{-i\epsilon}}{M\epsilon}\left(\sin(\epsilon)\sqrt{1-\left(\frac{M\epsilon}{2}\right)^2+\frac{M\epsilon}{\tan(\epsilon)}}-\sin(\epsilon)-\frac{M\epsilon}{2}\cos(\epsilon)\right). \tag{3.45}$$

Although it appears that there is a singularity at $\epsilon = 0$, if we look a bit closer, since $\sin(\epsilon) \approx \epsilon$ for small ϵ, this singularity is removable. This means that the only singularities come from the branch points due to the square root. These branch points occur when the function under the square root is zero or infinite. It appears that the branch points correspond to the edges of the stop bands. This function is plotted in figure 3.3. The asymptotes of the function, spaced out at integer multiples of π, are caused by the $\tan(\epsilon)$ term. It appears that the branch cuts cluster, near these asymptotes such that if we define the n^{th} branch point to be located at

$$\epsilon_n = n\pi + \mu \tag{3.46}$$

then as $n \to \infty$, $\mu \to 0$. We can show this by rearranging the expression into the form

$$\tan(\epsilon) = \frac{M\epsilon}{\left(\frac{M\epsilon}{2}\right)^2 - 1} \tag{3.47}$$

then since

$$\lim_{\epsilon\to\infty}\left(\frac{M\epsilon}{\left(\frac{M\epsilon}{2}\right)^2 - 1}\right) = 0, \tag{3.48}$$

the expression (3.47) is satisfied when

$$\tan(\epsilon) = 0 \tag{3.49}$$

or

$$\epsilon = n\pi. \tag{3.50}$$

Because we have an infinite number of branch points to close, we will always find ourselves with an infinite number of branch cuts. Clearly, we cannot expect to get an exact solution of (3.44) due to the infinite number of branch cuts.

3.6.1 Replacing the branch cuts with a series of poles

We will now show how to remove the branch points from the integral, leaving only poles. We begin by rearranging the reflection coefficient, (3.45), by taking the sine

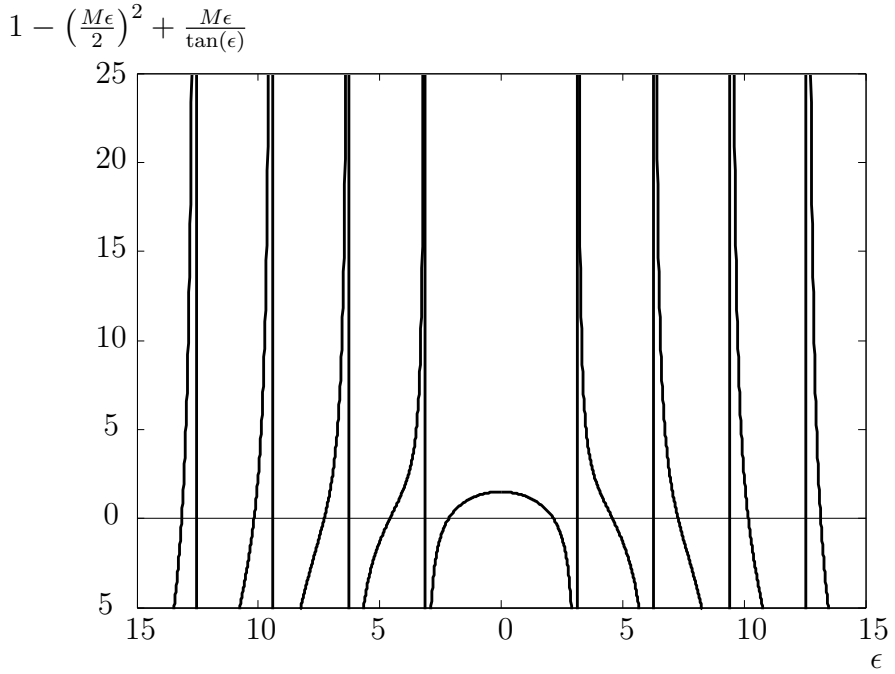

Figure 3.3: The root function in (3.45) giving the branch cuts (i.e. where the function vanishes or is infinite) of the reflection coefficient.

term out of the square root and converting trigonometric terms into exponential form

$$\begin{aligned} R(\epsilon) &= \frac{2e^{-i\epsilon}}{M\epsilon}\left(\sqrt{\sin(\epsilon)}\sqrt{\left(1-\left(\frac{M\epsilon}{2}\right)^2\right)\sin(\epsilon)+M\epsilon\cos(\epsilon)}-\sin(\epsilon)-\frac{M\epsilon}{2}\cos(\epsilon)\right) \\ &= \frac{2e^{-i\epsilon}}{M\epsilon}\left(\sqrt{\frac{e^{i\epsilon}-e^{-i\epsilon}}{2i}}\sqrt{\left(1-\left(\frac{M\epsilon}{2}\right)^2\right)\frac{e^{i\epsilon}-e^{-i\epsilon}}{2i}+M\epsilon\frac{e^{i\epsilon}+e^{-i\epsilon}}{2}}\right. \\ &\qquad \left.-\frac{e^{i\epsilon}-e^{-i\epsilon}}{2i}-\frac{M\epsilon}{2}\frac{e^{i\epsilon}+e^{-i\epsilon}}{2}\right). \end{aligned} \tag{3.51}$$

The aim now is to get the square roots in the form $\sqrt{1+f(\epsilon)e^{2i\epsilon}}$, for some function $f(\epsilon)$. Once we have this, the square root can be expanded using the binomial theorem,

giving increasing powers of $e^{2i\epsilon}$. We can rearrange (3.51) to give

$$R(\epsilon) = \frac{2e^{-i\epsilon}}{M\epsilon}\left(\sqrt{\frac{i}{2}\left(e^{-i\epsilon}-e^{i\epsilon}\right)}\sqrt{\frac{1}{2i}\left(-\left(1-\frac{iM\epsilon}{2}\right)^2 e^{-i\epsilon}+\left(1+\frac{iM\epsilon}{2}\right)^2 e^{i\epsilon}\right)}\right.$$
$$\left.-\frac{e^{i\epsilon}-e^{-i\epsilon}}{2i}-\frac{M\epsilon}{2}\frac{e^{i\epsilon}+e^{-i\epsilon}}{2}\right) \tag{3.52}$$

$$= \frac{e^{-2i\epsilon}}{M\epsilon}\left(i\left(1-\frac{iM\epsilon}{2}\right)\left(1-e^{2i\epsilon}\right)^{1/2}\left(1-\frac{\left(1+\frac{iM\epsilon}{2}\right)^2}{\left(1-\frac{iM\epsilon}{2}\right)^2}e^{2i\epsilon}\right)^{1/2}\right.$$
$$\left.+\,i(e^{2i\epsilon}-1)-\frac{M\epsilon}{2}(e^{2i\epsilon}+1)\right), \tag{3.53}$$

and so we can expand the square root functions using the binomial expansion, giving

$$R(\epsilon) = \frac{iM\epsilon}{2-iM\epsilon}+\frac{4iM\epsilon\, e^{2i\epsilon}}{(2-iM\epsilon)^3}+\dots\,. \tag{3.54}$$

We note that for each additional term of the expansion, we get a higher power of $e^{2i\epsilon}$. When we substitute this into the integral (3.44) we get a series of integrals. For example, when $x = 0$ we have

$$u(0,t) = \int_{-\infty}^{\infty} a_0 e^{-i\epsilon t}+a_1 e^{-i\epsilon(t-2)}+a_2 e^{-i\epsilon(t-4)}+\dots d\epsilon, \tag{3.55}$$

where $a_0(\epsilon), a_1(\epsilon), \dots$ are the terms obtained from the binomial expansions and contain only poles. Since the binomial expansion will involve only poles and no branch points, all of these integrals can be evaluated easily by using Cauchy's residue theorem. At any point in time, we only pick up a finite number of poles. This trick will be discussed more in the next chapter.

In figures 3.4 and 3.5, we can see the reflection of two different pulses from a string with periodically spaced beads. What we are seeing here is the shape of the wave as it travels back along the string to the left. In the first figure, 3.4, we impose a Dirac delta function as the incoming pulse. Due to the extreme nature of this input we see discontinuities in slope each time the pulse reflects from a bead. The second loading is a triangular shaped pulse. The response in this case is a lot smoother. We can see the tail of the pulse decay quickly in time.

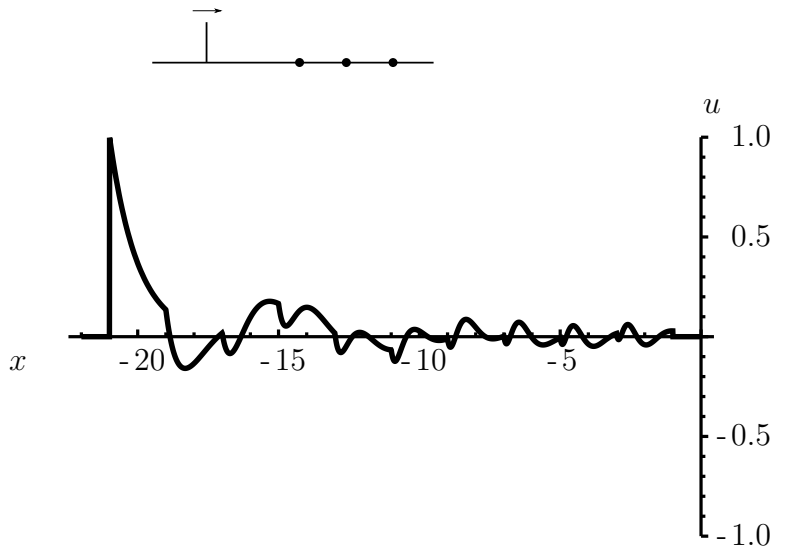

Figure 3.4: The response of a delta function hitting a set of periodically spaced beads.

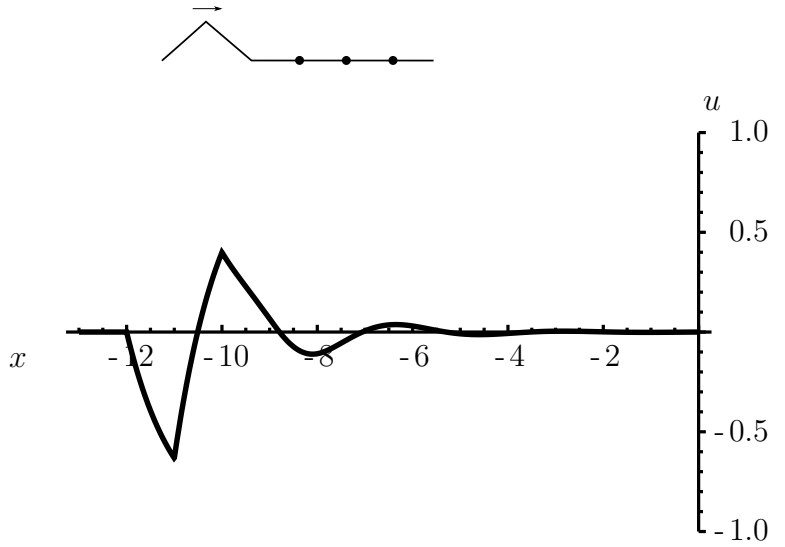

Figure 3.5: The response of a triangle function hitting a set of periodically spaced beads.

3.7 Conclusion

In this chapter we have studied the exact reflection of a pulse from an infinite set of periodically spaced beads. The solution for the reflected pulse was given in terms of the inverse Fourier transform. This solution involves the reflection coefficient for the time-harmonic wave. Both the exact and effective reflection coefficients were found and compared. For the exact reflection coefficient we have shown how it is possible to convert the branch points of the solution into a sum of terms, each containing only

poles.

In comparing the exact and effective reflection coefficients we found that the effective term is only valid in the low frequency regime despite the fact that the exact infinite beaded string wavenumber is used. This implies that even if we know exactly how a wave propagates when inside a heterogeneous material (from k_*), we still do not know how the wave reflects and transmits at a boundary. Using an effective reflection coefficient for a pulse reflection problem is insufficient because the pulse is broadband and contains all frequencies. A large body of work, especially in engineering, is focused on finding the effective properties of a material rather than focussing on this more important issue.

In the next section we will study in more detail how a pulse enters a heterogeneous media. The geometry considered will be an infinite string that is initially at rest. At a specified time, we start to force the bead at the origin with some specified loading. By this means we hope to gain insight into how waves of specific frequencies behave differently in stop and pass bands and how their energy enters the periodic system.

Chapter 4

The transient excitation of waves on a string carrying an infinite array of peridocally spaced point masses

4.1 Introduction

The aim of this chapter is to study the time-dependent motion of waves excited on an infinite string with a periodic heterogeneity made up of equally spaced point masses. The bead at the origin is forced with some prescribed input. This forcing is switched on at $t = 0$. From studying this problem, insight is gained into how stop and pass bands manifest in transient problems. Although the application is rather rudimentary it illustrates the difficulties that are encountered generally in such problems. The mathematics required is non-trivial even in this simple application. Results are not necessarily intuitive and illustrate the effects of transient forcing rather neatly.

In this chapter, we study the transient response from an infinite series of beads. We force the bead at the origin with some prescribed function. This force is switched on at $t = 0$ so initially the bead is at rest. We use integral transforms to find the solution of the bead displacements. The displacements are found exactly in terms of an expansion of poles. The long-time solution is also investigated as well as the energy input into the system. This method is advantageous over direct numerical simulation

because the solution at any finite point in time is exact. Also, the asymptotic long-time behaviour can be obtained in a straightforward manner.

4.2 The problem configuration

We investigate the time-dependent forcing of an infinite string with periodically spaced point masses. The configuration is pictured in figure 4.1. As shown, the bead to be forced is located at $x = 0$. The response of the other beads on the string will be determined analytically.

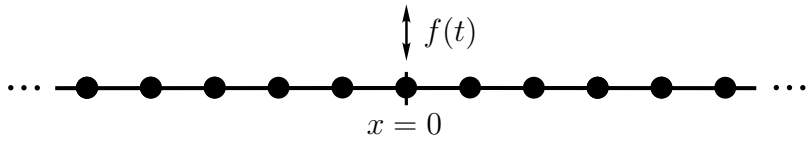

Figure 4.1: An infinite number of masses placed periodically with unit spacing along a string.

Let us begin with the equation of motion for an infinite beaded string, which is forced at the origin as given by equation (2.63)

$$\frac{\partial^2 u}{\partial x^2} = \left(1 + M \sum_{n=-\infty}^{\infty} \delta(x-n)\right) \frac{\partial^2 u}{\partial t^2} + \delta(x) f(t). \tag{4.1}$$

Using the nondimensionalisation given in section 2.1.1, the nondimensional mass M is given by $M = m/\rho_0 \ell$ where m is the dimensional mass, ρ_0 is the string density (i.e. mass per unit length) and ℓ is the period. The infinite sum in (4.1) accounts for the added mass of each bead and the final term corresponds to the force imposed at the origin. The forcing $f(t)$ is given by

$$f(t) = H(t) f_0(t), \tag{4.2}$$

where $H(t)$ is the Heaviside step function, which is defined as

$$H(t) = \begin{cases} 0 & \text{for } t < 0 \\ 1 & \text{for } t > 0 \end{cases} \tag{4.3}$$

and ensures that the forcing does not act for $t < 0$. A typical form for $f_0(t)$ would be $f_0(t) = \sin(\omega_* t)$. This particular form allows us to explore how the time-dependent

response reaches a steady harmonic state in both stop and pass bands. Both the short term transients, and by taking a long-time approximation, the steady-state behaviour are obtained.

Another forcing that is of interest is $f_0(t) = \sin(\omega_* t)H(T-t)$, for $T > 0$, which corresponds to a wave packet that lasts for a finite amount of time (given by T). The advantage of using this forcing is that it gives us a chance to isolate the transient behaviour without concerning ourselves with the long-time behaviour.

4.3 Finding the solution

In obtaining the solution to this problem we require the use of the Fourier transform. This was defined in the introduction by equation (2.14), i.e.

$$\hat{u}(\epsilon) = \int_{-\infty}^{\infty} u(x)e^{i\epsilon x}dx, \tag{4.4}$$

where ϵ is the transform variable. In this chapter, k and ω are used for the transform variables in space and time respectively. The Fourier transform in space is denoted by a hat, $\hat{u}(k,t)$, and the time transform by a capital letter, $U(x,\omega)$. A transform in both space and time is denoted by $\hat{U}(k,\omega)$.

The solution technique is outlined as follows

- The Fourier transform of (4.1) is taken in space (x) and then time (t) to find the solution in the transform domain. $u(x,t) \to \hat{U}(k,\omega)$.
- We invert in the k-domain back to the space domain, obtaining an implicit solution in the space-frequency domain, $U(x,\omega)$.
- This solution is sampled at the bead position yielding an infinite system of equations to which we apply the discrete z transform. $U(x,\omega) \to V(z,\omega)$.
- The inverse z transform is performed to get the explicit solution at the bead positions, $U(m,\omega)$.
- The inverse Fourier transform in time is performed to transform the solution at the bead positions back into the space-time domain, $u(m,t)$.

Once the solution is obtained, we then investigate its behaviour. Primarily we will compare the transient solution to the stop and pass band behaviour predicted by the infinite string time-harmonic theory. The long-time approximation to the solution is found and then the energy input into the system is investigated in different regimes.

In taking the Fourier transform of (4.1) in both time and space, we find

$$k^2\hat{U}(k,\omega) = \omega^2\hat{U}(k,\omega) + M\omega^2 \sum_{n=-\infty}^{\infty} U(n,\omega)e^{ikn} - F(\omega). \tag{4.5}$$

This can be trivially rearranged to

$$\hat{U}(k,\omega) = \frac{M\omega^2}{(k+\omega)(k-\omega)} \sum_{n=-\infty}^{\infty} U(n,\omega)e^{ikn} - \frac{F(\omega)}{(k+\omega)(k-\omega)},$$

giving the solution implicitly in the wavenumber-frequency domain

4.3.1 Singularities in the ω plane

Before performing the inversion back into the spatial domain, one important comment about the time domain inversion is made. Since the Heaviside function is included in the forcing, the solution must be zero for $t < 0$. Recall that the inverse Fourier transform is given by

$$u(t) = \frac{1}{2\pi}\int_{-\infty}^{\infty} U(\omega)e^{-i\omega t}d\omega. \tag{4.6}$$

When $t < 0$, the integral is closed into a D-shaped contour by adding a semi-circular path of radius R in the upper half plane. As $R \to \infty$, the contribution from the semi-circular section vanishes since the integrand experiences exponential decay at all points along this path. Because the integral along the real line must also be zero in this case, we know that there can be no singularities in the upper half plane. Since all singularities are below the integration path along the real line in (4.6), a constant positive imaginary part can legitimately be added onto ω. The integration contour is now along the path

$$\omega = \omega_r + i\,\omega_i, \tag{4.7}$$

where ω_r runs from $-\infty$ to ∞ and ω_i is a positive constant. It does not matter how large we take ω_i, the integration contour is still valid. In fact, any path may be chosen which runs from left to right and always remains in the upper half plane. In the following analysis we consider ω_i as a small positive constant.

4.3.2 Performing the inverse Fourier transform in space

Proceeding with the evaluation of the inverse Fourier transform in space, we begin by considering a positive value of x, located between any two beads. That is, we have $0 \leq m < x < m+1$ for some integer m. The solution in the space-frequency domain is given by the integral

$$U^{>}(x,\omega) = \frac{1}{2\pi}\int_{-\infty}^{\infty}\left(\frac{M\omega^2}{(k+\omega)(k-\omega)}\sum_{n=-\infty}^{\infty}U(n,\omega)e^{ikn} - \frac{F(\omega)}{(k+\omega)(k-\omega)}\right)e^{-ikx}dk, \tag{4.8}$$

where the superscript $>$ reminds us that $x > 0$. This is split into three separate integrals with the sums taken outside

$$\begin{aligned} U^{>}(x,\omega) = {} & \frac{M\omega^2}{2\pi}\sum_{n=-\infty}^{m}U(n,\omega)\int_{-\infty}^{\infty}\frac{e^{ik(n-x)}}{(k-\omega)(k+\omega)}dk \\ & + \frac{M\omega^2}{2\pi}\sum_{n=m+1}^{\infty}U(n,\omega)\int_{-\infty}^{\infty}\frac{e^{ik(n-x)}}{(k-\omega)(k+\omega)}dk \\ & - \frac{F(\omega)}{2\pi}\int_{-\infty}^{\infty}\frac{e^{-ikx}}{(k-\omega)(k+\omega)}dk. \end{aligned} \tag{4.9}$$

The reason for splitting the integral in this way is to make it explicit whether the exponent in the integrand is positive or negative for a given $x \in (m, m+1)$

The contour along the real line is closed using a semi-circular path running either above or below the real line, depending on the sign of the exponent. Since ω has a positive imaginary part, the pole at $k = +\omega$ lies in the upper half plane and the pole at $k = -\omega$ lies in the lower half plane. The contour path is shown in figure 4.2 for ω_i taking a small positive value.

Bearing in mind that the exponent in the first integral on the right-hand side of (4.9) is negative ($n - x < 0$), the first set of integrals are closed in the lower half plane (picking up the residues of the poles at $k = -\omega$). Similarly, because the exponent in the second integral is positive ($n - x > 0$), the second set of integrals are closed in the upper half plane (picking up the residues of the poles at $k = +\omega$). The third integral is closed in the lower half plane since we are considering $x > 0$. The solution in the space-frequency domain is thus

$$U^{>}(x,\omega) = \frac{M\omega i}{2}\sum_{n=-\infty}^{\infty}U(n,\omega)e^{i\omega|n-x|} - \frac{F(\omega)i\ e^{i\omega x}}{2\omega}. \tag{4.10}$$

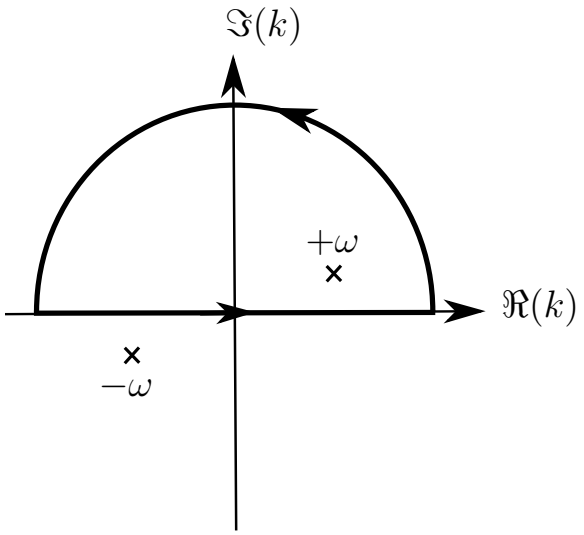

Figure 4.2: A D-shaped contour, deformed above the real line, picking up the contour at $k = +\omega$.

Following the same procedure when $x < 0$, we get

$$U^{<}(x,\omega) = \frac{M\omega i}{2} \sum_{n=-\infty}^{\infty} U(n,\omega) e^{i\omega|n-x|} - \frac{F(\omega) i\, e^{-i\omega x}}{2\omega}. \tag{4.11}$$

These two solutions can be combined into one by taking the modulus of x in the last term

$$U(x,\omega) = \frac{M\omega i}{2} \sum_{n=-\infty}^{\infty} U(n,\omega) e^{i\omega|n-x|} - \frac{F(\omega) i\, e^{i\omega|x|}}{2\omega}. \tag{4.12}$$

Equation (4.12) gives an implicit solution at any point on the string and is related to that given in (3.13). This solution is implicit because it depends on the unknown displacements at every bead position. The solution may be sampled at each bead position, giving an infinite system of equations. This system is solved by applying a z transform to find the bead displacements.

4.3.3 The z transform

Sampling the solution (4.12) at a single bead point $x = m$, we get the infinite system of equations

$$U(m,\omega) = \frac{M\omega i}{2} \sum_{n=-\infty}^{\infty} U(n,\omega) e^{i\omega|n-m|} - \frac{F(\omega) i\, e^{i\omega|m|}}{2\omega}. \tag{4.13}$$

Take the z transform as defined by equation (2.15) by multiplying by z^m and summing over all m values

$$\sum_{m=-\infty}^{\infty} z^m U(m,\omega) = \frac{M\omega i}{2} \sum_{m=-\infty}^{\infty} \sum_{n=-\infty}^{\infty} z^m U(n,\omega) e^{i\omega|n-m|} - \sum_{m=-\infty}^{\infty} \frac{z^m F(\omega) i \; e^{i\omega|m|}}{2\omega}. \tag{4.14}$$

In doing this, the sampling point m has become a dummy variable, being replaced by the independent parameter z. We choose to make the change of variables $u = m - n$ in the first term on the right-hand side, giving

$$\sum_{m=-\infty}^{\infty} z^m U(m,\omega) = \frac{M\omega i}{2} \sum_{n=-\infty}^{\infty} z^n U(n,\omega) \sum_{u=-\infty}^{\infty} z^u e^{i\omega|u|} - \frac{F(\omega) i}{2\omega} \sum_{m=-\infty}^{\infty} z^m \; e^{i\omega|m|}. \tag{4.15}$$

The sum on the left-hand side is denoted $V(z,\omega) = \sum_{m=-\infty}^{\infty} z^m U(m,\omega)$, allowing us to rearrange (4.15) into the form

$$V(z,\omega)\left(1 - \frac{M\omega i}{2} \sum_{u=-\infty}^{\infty} z^u e^{i\omega|u|}\right) = -\frac{F(\omega) i}{2\omega} \sum_{u=-\infty}^{\infty} z^u \; e^{i\omega|u|}. \tag{4.16}$$

The remaining sum in (4.16) is split into two parts,

$$\sum_{u=-\infty}^{\infty} z^u e^{i\omega|u|} = \sum_{u=0}^{\infty} z^u e^{i\omega u} + \sum_{u=1}^{\infty} z^{-u} e^{i\omega u}. \tag{4.17}$$

These are both geometric series, which can be summed exactly using

$$\sum_{u=0}^{\infty} z^u e^{i\omega u} = \frac{-e^{-i\omega}}{z - e^{-i\omega}} \tag{4.18}$$

and

$$\sum_{u=1}^{\infty} z^{-u} e^{i\omega u} = \frac{e^{i\omega}}{z - e^{i\omega}}. \tag{4.19}$$

These identities hold provided the modulus of the respective summands are less than one. Recall that ω has a positive imaginary part, i.e. $\omega = \omega_r + i\,\omega_i$. With this in mind, the first sum, (4.18), converges in the region defined by

$$|z| < e^{\omega_i}, \tag{4.20}$$

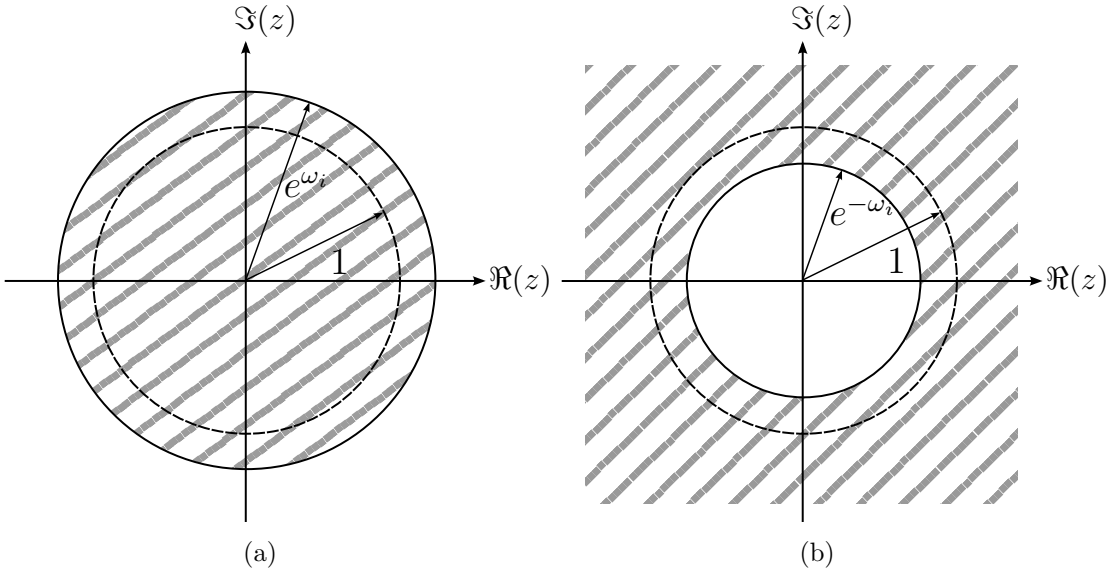

Figure 4.3: These figures show the regions of convergence for (a) the sum given in (4.18) and (b) the sum given in (4.19)

.

which is the region inside the disk of radius $e^{\omega_i} > 1$, shown in figure 4.3(a). The second sum, (4.19), converges in the region

$$|z| > e^{-\omega_i}, \tag{4.21}$$

which is the region outside the disk of radius $e^{-\omega_i} < 1$, shown in figure 4.3(b). What is important is that both sums converge on the circle defined by $|z| = 1$, since this will be the contour path of the inverse z transform.

Substituting (4.18) and (4.19) into equation (4.16), we find that

$$V(z,\omega) = \frac{\dfrac{F(\omega)i}{2\omega}\left(\dfrac{e^{-i\omega}}{z-e^{-i\omega}} - \dfrac{e^{i\omega}}{z-e^{i\omega}}\right)}{1 + \dfrac{M\omega i}{2}\left(\dfrac{e^{-i\omega}}{z-e^{-i\omega}} - \dfrac{e^{i\omega}}{z-e^{i\omega}}\right)}. \tag{4.22}$$

This may be simplified by multiplying top and bottom by $(z-e^{-i\omega})(z-e^{i\omega})$, to give

$$V(z,\omega) = \frac{F(\omega)z\sin(\omega)}{\omega\left(z^2 - 2z\left(\cos(\omega) - \frac{M\omega}{2}\sin(\omega)\right) + 1\right)}. \tag{4.23}$$

This function clearly has two poles in the z plane, which are given by the quadratic formula

$$z_*^{\pm} = \cos(\omega) - \frac{M\omega}{2}\sin(\omega) \pm \sqrt{\left(\cos(\omega) - \frac{M\omega}{2}\sin(\omega)\right)^2 - 1}. \tag{4.24}$$

Care must be taken in defining the square root since this function is multivalued.

Relation with effective wavenumber

It is possible to relate $z_*^{\pm}$ to the effective wavenumber of the beaded string, k_*, given by (2.71)

$$\cos(k_*) = \cos(\omega) - \frac{M\omega}{2}\sin(\omega). \tag{4.25}$$

With this in mind, we see that $z_*^{\pm}$ is given by

$$z_*^{\pm} = \cos(k_*) \mp i\sin(k_*) = e^{\mp ik_*}, \tag{4.26}$$

where the negative branch of $\sqrt{-1}$ has been taken. The reason for this will become clear later. We note from here that z_*^+ and z_*^- are reciprocals of each other. In the situation where k_* is purely real (a pass band), then z_*^+ is also complex conjugate to z_*^-. Alternatively, when k_* is complex (a stop band) the real part of k_* must be an integer multiple of π. This gives

$$z_*^+ = \frac{1}{z_*^-} = \pm e^{+\Im(k_*)}. \tag{4.27}$$

In this expression, the $\pm$ refers to the fact that the sign can either be positive or negative depending on whether $\Re(k_*)$ is equal an even or odd multiple of π respectively.

In figure 4.4 we plot the real, imaginary and absolute values of z_*^+ (4.4(a)) and z_*^- (4.4(b)) as a function of the real part of the frequency, $\Re(\omega)$. Note that the regions where $|z_*^{\pm}| = 1$ correspond to pass bands and the regions where $|z_*^+| > 1$ (and subsequently $|z_*^-| < 1$) correspond to stop bands. As mentioned earlier, we note that in the stop bands, the imaginary part of $z_*^{\pm}$ is zero: the poles are purely real. It is also clear from the diagrams that z_*^+ is the reciprocal of z_*^-. In the pass bands, this corresponds to them being complex conjugates. Lastly, we note that $z_*^{\pm}(-\omega)$ is the complex conjugate of $z_*^{\pm}(\omega)$.

The branch cut structure

In order to be precise in the definition of $z_*^{\pm}$ we must define how the branch cuts of the square root in equation (4.24) are laid out and which sheet of the Riemann surface we are on. First note that the square root gives an infinite number of branch points all residing on the real line; half of which are located at $\omega = n\pi$ for $n \in \mathbb{Z}$, $n \neq 0$ (since $\cos(\omega) = 1$ and $\sin(\omega) = 0$) and the other half lie in between these and are located at positions named $\omega = \pm\omega_n$ for $n = 0, 1, 2\ldots$, noting that the position of these branch

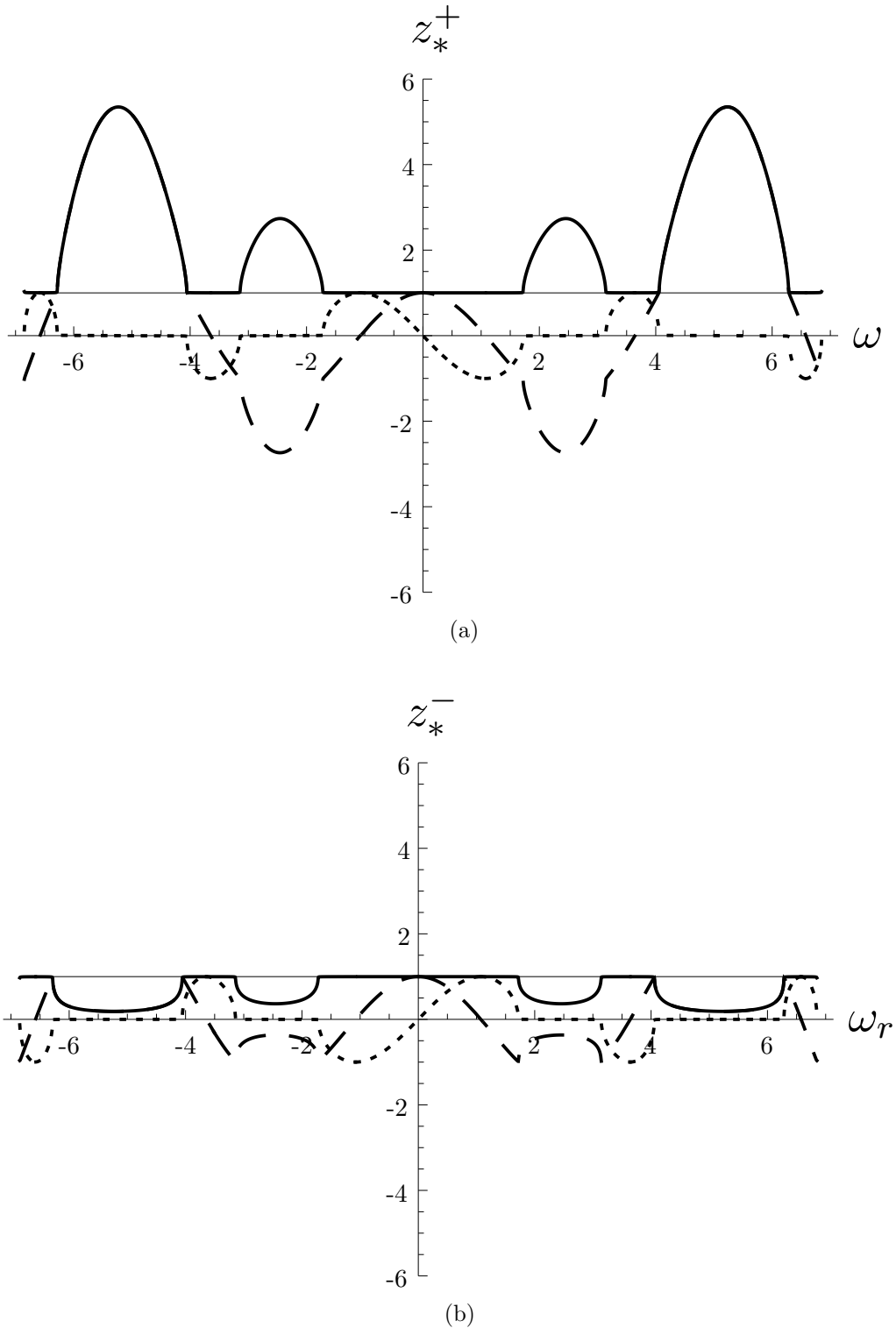

Figure 4.4: The values of (a) z_*^+ and (b) z_*^- for $M = 1$. The absolute value is given by the solid line, the real part by the dashed line and the imaginary part by the dotted line. The thin straight line is located at $z_* = 1$. The horizontal axis gives the frequency, ω. The imaginary part is taken to be vanishingly small, that is $\Im(\omega) = \omega_i = 0^+$.

points is symmetric with respect to the origin. It can be shown that the location of these branch points corresponds to the edges of the stop bands. This can be verified simply be noting that the branch points occur when

$$\cos(\omega) - \frac{M\omega}{2}\sin(\omega) = \cos(k_*) = \pm 1. \tag{4.28}$$

As we will discuss later, we don't have a branch cut at $\omega = 0$.

A choice has been made for all branch cuts to run vertically downward in the complex ω plane as shown in figure 4.6. Once this choice is made, a decision must be made as to which sheet of the Riemann surface we are on. This is defined by restricting the angle of the argument of the square root at each branch point. With vertical square-root branch cuts, the possible choices are

$$-\frac{\pi}{2} < \theta < \frac{3\pi}{2} \tag{4.29}$$

and

$$\frac{3\pi}{2} < \theta < \frac{7\pi}{2}. \tag{4.30}$$

Any other choice of θ can be shown to be equivalent to one of these two choices. With $\omega_i \neq 0$, the restriction of the angles is chosen such that the pole at z_*^+ always lies outside the unit circle and the pole at z_*^- always lies inside the unit circle. The justification for these choices will become clear when considering the inverse z transform.

4.3.4 Back to the physical space domain

In order to obtain the solution in the physical domain, the inverse z transform of (4.23) is taken. For the pth bead, this is defined by equation (2.17),

$$U(p,\omega) = \frac{1}{2\pi i}\oint_C V(z,\omega) z^{-p-1} dz, \qquad \text{where } p \in \mathbb{Z}, \tag{4.31}$$

and where the contour C runs anti-clockwise around the unit circle. Recall that $V(z,\omega)$, given by

$$\begin{aligned} V(z,\omega) &= \frac{F(\omega) z \sin(\omega)}{\omega\left(z^2 - 2z\left(\cos(\omega) - \frac{M\omega}{2}\sin(\omega)\right) + 1\right)} \\ &= \frac{F(\omega) z \sin(\omega)}{\omega(z - z_*^+)(z - z_*^-)}, \end{aligned} \tag{4.32}$$

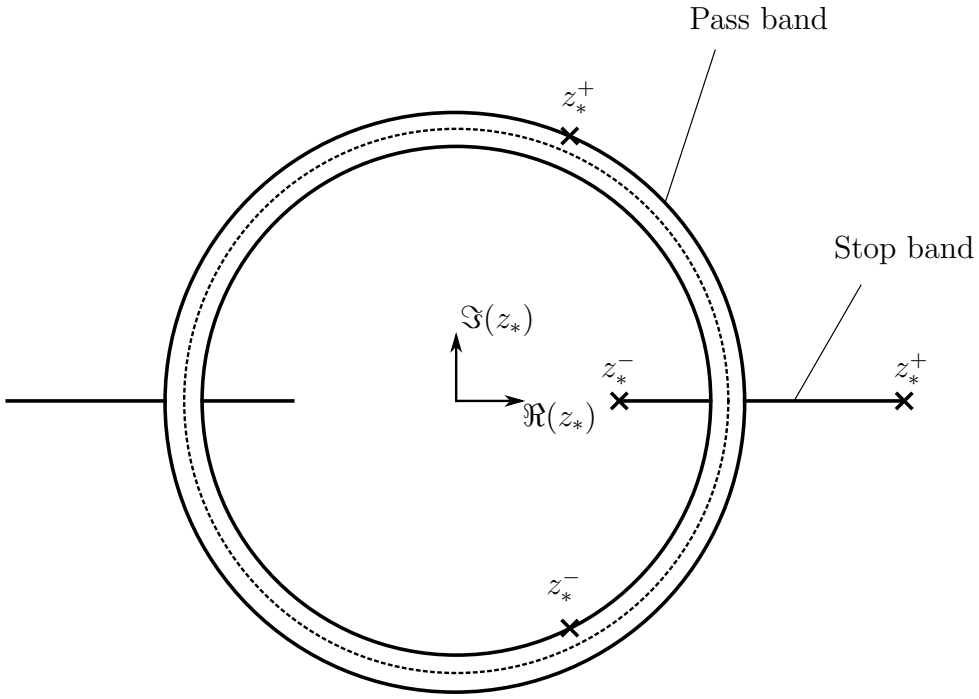

Figure 4.5: A schematic diagram showing the possible values of $z_*^{\pm}$ in the complex plane. The dotted line corresponds to $|z_*^{\pm}| = 1$. Two typical values of z_*^+ and z_*^- are shown. One is for ω chosen in a stop band, where $z_*^{\pm}$ lie on the real line. The other in for ω chosen in a pass band, where $z_*^{\pm}$ lie close the unit circle. Due to the small imaginary frequency component, ω_i, when in a pass band $z_*^{\pm}$ lie off the unit circle as required.

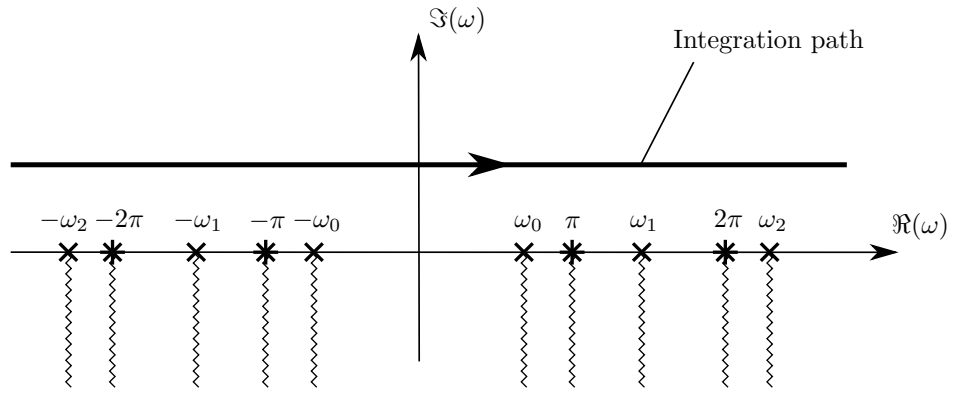

Figure 4.6: The branch points of $z_*^{\pm}$. The branch cuts are shown to run vertically downward and the integration path runs along the top since $\omega_i > 0$. The branch points at $\omega = n\pi$ are labelled with stars and those at $\omega = \omega_n$ with crosses.

which has two poles. One pole is located at z_*^+ (outside the unit circle) and the other is located at z_*^- (inside the unit circle). Substituting (4.32) into (4.31) gives

$$U(p,\omega) = \frac{F(\omega)\sin(\omega)}{2\pi i\,\omega} \oint_C \frac{z^{-p}}{(z - z_*^+)(z - z_*^-)} dz. \tag{4.33}$$

This integral is evaluated by using Cauchy's residue theorem.

When $p > 0$, the exponent of z is negative, giving a pole of order p at the origin. In order to avoid evaluation of this contribution, the contour is closed instead at infinity and the residue from $z = z_*^+$ only is obtained. The path integral at infinity becomes zero since the integrand decays sufficiently fast as $|z| \to \infty$. In this case the integral becomes

$$U(p,\omega) = -\frac{F(\omega)\sin(\omega)(z_*^+)^{-p}}{\omega(z_*^+ - z_*^-)} \quad \text{for} \quad p > 0. \tag{4.34}$$

When $p \leq 0$, there is no pole at the origin. In this case, the residue of the pole located at $z = z_*^-$ is picked up, giving

$$U(p,\omega) = -\frac{F(\omega)\sin(\omega)(z_*^-)^{-p}}{\omega(z_*^+ - z_*^-)} \quad \text{for} \quad p \leq 0. \tag{4.35}$$

Using the fact that $z_*^+ = (z_*^-)^{-1}$, for any p, we have

$$U(p,\omega) = -\frac{F(\omega)\sin(\omega)(z_*^+)^{-|p|}}{\omega(z_*^+ - z_*^-)}. \tag{4.36}$$

Recall from (4.26) that

$$z_*^{\pm} = e^{\mp ik_*},$$

where k_* is the effective wavenumber of the string. The $(z_*^+)^{-|p|}$ term in (4.36) is now given by

$$(z_*^+)^{-|p|} = e^{ik_*|p|}. \tag{4.37}$$

In essence, this term represents the outgoing waves from the forcing point at the origin. They travel with the effective wavenumber given by the homogenised string as described in the background section 2.2. All of the transient behaviour of the string is accounted for by the singularity structure of (4.36) in the complex ω-plane. We will mostly choose not to represent the terms given by $z_*^{\pm}$ as $e^{\mp ik_*}$ since it can hide the underlying mathematics. Instead, the full form with the square root function is retained.

Substituting equation (4.24) into (4.36), we obtain the explicit solution in ω space

$$U(p,\omega) = -\frac{F(\omega)\sin(\omega)\left(\cos(\omega) - \frac{M\omega}{2}\sin(\omega) + \sqrt{\left(\cos(\omega) - \frac{M\omega}{2}\sin(\omega)\right)^2 - 1}\right)^{-|p|}}{2\,\omega\sqrt{\left(\cos(\omega) - \frac{M\omega}{2}\sin(\omega)\right)^2 - 1}}.$$

This may be inverted to give the solution at each bead position in the time domain

$$u(p,t) = \frac{-1}{4\pi}\int_{-\infty}^{\infty} \frac{F(\omega)\sin(\omega)\left(\cos(\omega) - \frac{M\omega}{2}\sin(\omega) + \sqrt{G(\omega)}\right)^{-|p|} e^{-i\omega t}}{\omega\sqrt{G(\omega)}} d\omega, \tag{4.38}$$

where for convenience, the expression under the square root is written as

$$G(\omega) = \left(\cos(\omega) - \frac{M\omega}{2}\sin(\omega)\right)^2 - 1. \tag{4.39}$$

The behaviour of the string and bead displacements is entirely related to the singularity structure of the integrand. There are an infinite number of branch points due to $\sqrt{G(\omega)}$, a simple pole at $\omega = 0$ and possible singularities from $F(\omega)$.

4.3.5 Contour deformation

Before evaluating the integral fully, we analyse the solution in different regions of space and time. Let us briefly return to the exponential form of z_*^+ given in equation (4.37). In using this form, the solution (4.38) is given by

$$u(p,t) = \frac{-1}{4\pi}\int_{-\infty}^{\infty} \frac{F(\omega)\sin(\omega)e^{i(k_*|p|-\omega t)}}{\omega\sqrt{G(\omega)}}d\omega. \tag{4.40}$$

Let us define $\gamma = k_*/\omega$ which is essentially the reciprocal of the effective wave speed. In doing this, the integral becomes

$$u(p,t) = \frac{-1}{4\pi}\int_{-\infty}^{\infty} \frac{F(\omega)\sin(\omega)e^{i\omega(\gamma|p|-t)}}{\omega\sqrt{G(\omega)}}d\omega. \tag{4.41}$$

In evaluating this integral there are two cases to consider. When $t < \Re(\gamma)|p|$, the contour is closed in the upper half plane and no singularities are picked up. When $t > \Re(\gamma)|p|$, the contour is closed in the lower half plane and the contributions from all singularities are picked up. We can now argue that it is due to causality that the branch cut structure in equation (4.26) was chosen.

4.4 The finite time solution

It is possible to evaluate the exact solution given by (4.38) at any finite point in time. The method used will be described here. The integrand currently has an infinite number of branch points. In order to obtain the solution, an integral must be performed along each of the branch cuts emanating from these points. Not only do we have an

infinite number of these integrals, it is not possible to evaluate them analytically so numerical methods are needed to approximate their values.

Instead of attempting to numerically evaluate a finite number of these integrals, the integrand will be converted into a form such that the branch points are transformed into poles. These poles can trivially be evaluated using the residue theorem. Although the solution is still given as an infinite series, we are careful to construct the integrand in such a way that at any point in time, only a finite number of terms give a non-zero contribution.

4.4.1 A chosen forcing

Before proceeding, the forcing must be prescribed so that the entire singularity structure of the integrand is known. As an illustrative example, a sinusoidal forcing that is turned on at $t = 0$ is chosen. This makes the input to the problem in equation (4.1) equal to

$$f(t) = H(t)\sin(\omega_* t), \tag{4.42}$$

where ω_* is the chosen forcing frequency. The Fourier transform of this input is given by

$$\begin{aligned} F(\omega) &= \int_0^\infty \sin(\omega_* t) e^{i\omega t} dt \\ &= \frac{-\omega_*}{\omega^2 - \omega_*^2}. \end{aligned} \tag{4.43}$$

This term will introduce two simple poles into the solution located at $\omega = \pm\omega_*$.

4.4.2 Expansion of the $\sqrt{G(\omega)}$ term

In order to convert the branch points into poles, the square root term in (4.38) is expanded by use of the binomial theorem. This expansion converts the branch points into a series of poles in the lower half plane. At the same time, a series with increasing powers of $e^{2i\omega}$ is created. Each of these subsequent powers of $e^{2i\omega}$ causes a time delay before deforming the respective contours into the lower half plane and picking up their contribution from the poles.

In order to expand $\sqrt{G(\omega)}$, it must first be rearranged. Recall that $\sqrt{G(\omega)}$ is

given by

$$\sqrt{G(\omega)} = \sqrt{\left(\cos(\omega) - \frac{M\omega}{2}\sin(\omega)\right)^2 - 1} \tag{4.44}$$
$$= \sqrt{\left(\left(\frac{M\omega}{2}\right)^2 - 1\right)\sin^2(\omega) - M\omega\cos(\omega)\sin(\omega)}\ .$$

By using the exponential form of the trigonometric functions, after some rearrangement we obtain

$$\sqrt{G(\omega)} = \sqrt{\frac{e^{-i\omega} - e^{i\omega}}{4}\left(\left(1 - \frac{M\omega i}{2}\right)^2 e^{-i\omega} - \left(1 + \frac{M\omega i}{2}\right)^2 e^{i\omega}\right)} \tag{4.45}$$
$$= \sqrt{\frac{e^{-2i\omega}\left(1 - \frac{M\omega i}{2}\right)^2}{4}(1 - e^{2i\omega})\left(1 - \left(\frac{1 + \frac{M\omega i}{2}}{1 - \frac{M\omega i}{2}}\right)^2 e^{2i\omega}\right)}.$$

Separating terms, the expression becomes

$$\sqrt{G(\omega)} = \frac{e^{-i\omega}\left(1 - \frac{M\omega i}{2}\right)}{2}(1 - e^{2i\omega})^{1/2}\left(1 - \left(\frac{1 + \frac{M\omega i}{2}}{1 - \frac{M\omega i}{2}}\right)^2 e^{2i\omega}\right)^{1/2}. \tag{4.46}$$

The remaining square roots can be expanded using the generalised binomial theorem, which is given by the infinite sum

$$(1 + x)^n = \sum_{r=0}^{\infty} \binom{n}{r} x^r. \tag{4.47}$$

In our example, the first two terms of (4.46) are given by

$$\sqrt{G(\omega)} = \frac{1 - \frac{M\omega i}{2}}{2}\, e^{-i\omega} - \frac{1}{4}\left(1 - \frac{M\omega i}{2} + \frac{(1 + \frac{M\omega i}{2})^2}{(1 - \frac{M\omega i}{2})}\right) e^{i\omega} + \dots\ . \tag{4.48}$$

In a similar manner to section 3.6.1 we can now write the solution (4.38) in expanded form. For example, considering the displacement at the origin we have

$$u(0, t) = \int_{-\infty}^{\infty} a_0 e^{-i\omega t} + a_1 e^{-i\omega(t-2)} + a_2 e^{-i\omega(t-4)} + \dots d\omega, \tag{4.49}$$

where $a_0(\omega), a_1(\omega), \dots$ are the terms obtained from the binomial expansions and contain only poles. This integral may be evaluated simply by finding the residues of the poles of a_n. As described in section 4.3.5 these contours are either deformed up (picking up no poles) or down (picking up a finite number of poles) depending on the sign of

the exponents. For example, when $0 < t < 2$, only the first contour is deformed down and the entire contribution comes from the first term of the series. When $2 < t < 4$ both the first and second terms are included and so on.

We note that in the expansion of equation (4.46), the location of all poles that have been introduced are at

$$\omega = -\frac{2i}{M}. \tag{4.50}$$

It is interesting to note that as higher terms in the series are taken, higher order poles at $\omega = -2i/M$ are obtained. For large times, evaluating the residues of the poles is possible, but is tedious and becomes numerically difficult due to the poles being given by ratios of very large numbers. For this reason, in this regime, we choose to investigate the long-time asymptotic behaviour.

4.5 The long-time asymptotic behaviour

Although it is possible to find the exact displacements at any finite time, this becomes increasingly difficult numerically. In this section the long-time behaviour of the solution will be discussed. We retain the sinusoidal forcing given by (4.42) with its Fourier transform being given by (4.43). In considering the long-time solution, we return to the original form given by (4.38), which with the forcing included, is given by

$$u(p,t) = \frac{\omega_*}{4\pi} \int_{-\infty}^{\infty} \frac{\sin(\omega)\left(\cos(\omega) - \frac{M\omega}{2}\sin(\omega) + \sqrt{G(\omega)}\right)^{-|p|} e^{-i\omega t}}{\omega(\omega^2 - \omega_*^2)\sqrt{G(\omega)}}\, d\omega. \tag{4.51}$$

Let us begin by studying the contribution due to the branch cuts and then consider the contributions due to the poles at $\omega = \pm\omega_*$ and $\omega = 0$.

4.5.1 The branch cut integrals

The solution has an infinite number of branch points given by the square root function. We begin by considering the expression $G(\omega)$ defined by (4.39). The square root is simplified by taking a factor of $\sin(\omega)/\omega$ out, giving

$$\sqrt{G(\omega)} = \sqrt{\frac{\sin(\omega)}{\omega}} \sqrt{\left(\left(\frac{M\omega}{2}\right)^2 - 1\right)\omega\sin(\omega) - M\omega^2\cos(\omega)}. \tag{4.52}$$

The reason for choosing this factor is not initially obvious. It has been chosen to illustrate the branch point structure. If instead a factor of $\sin(\omega)$ were taken out then we would apparently have a branch point at the origin. There are two sources of branch points from equation (4.52), one from each of the square roots. The first square root gives the series of branch points at $\omega = n\pi$ (for $n \neq 0$). The branch points from the second square root are located at $\omega = \omega_n$. The closest branch points to the origin are pictured in figure 4.6. As n increases towards $+\infty$, the branch point at ω_n approaches $\omega = n\pi$ from the right. Similarly, as n decreases towards $-\infty$, the branch point at ω_n approaches $\omega = n\pi$ from the left.

Product decomposition of each function

Before we proceed with further investigation of the branch cuts, a product decomposition of $G(\omega)$ is taken. In order to isolate the zero at the origin, $G(\omega)$ is written as

$$G(\omega) = \omega^2 P(\omega) Q(\omega), \tag{4.53}$$

where

$$P(\omega) = \frac{\sin(\omega)}{\omega} \tag{4.54}$$

$$Q(\omega) = \left(\left(\frac{M\omega}{2} \right)^2 - 1 \right) \frac{\sin(\omega)}{\omega} - M\cos(\omega). \tag{4.55}$$

Note that both $P(\omega)$ and $Q(\omega)$ have only zeros and no poles. When taking the square root of ω^2, care must be taken in order to choose the correct branch in order to be consistent with $\sqrt{G(\omega)}$, which we recall is given by

$$\sqrt{G(\omega)} = z_*^+ - z_*^-. \tag{4.56}$$

The singularities introduced by $G(\omega)$ include a simple pole and an infinite number of branch points given by the (infinite number of) zeros of $P(\omega)$ and $Q(\omega)$. With this in mind, the integral is now

$$u(p,t) = \frac{\omega_*}{4\pi} \int_{-\infty}^{\infty} \frac{\sqrt{P(\omega)} \left(\cos(\omega) - \frac{M\omega}{2}\sin(\omega) + \omega\sqrt{P(\omega)}\sqrt{Q(\omega)} \right)^{-|p|} e^{-i\omega t}}{(\omega^2 - \omega_*^2)\omega\sqrt{Q(\omega)}} d\omega.$$

Following the procedure outlined by Titchmarsh [83, p. 114], both $P(\omega)$ and $Q(\omega)$ will be written as infinite products. By taking a product decomposition, any meromorphic function $f(z)$ may be written in terms of its zeros as

$$f(z) = f(0)e^{z\frac{f'(0)}{f(0)}} \prod_{n=1}^{\infty} \left(1 - \frac{z}{a_n}\right) e^{z/a_n}, \tag{4.57}$$

where a_n denotes the position of the n^{th} zero. The expansion for $P(\omega)$ is well known to be

$$\begin{aligned} P(\omega) = \frac{\sin(\omega)}{\omega} &= \prod_{n=1}^{\infty} \left(1 - \frac{\omega^2}{n^2\pi^2}\right) \\ &= \prod_{n=1}^{\infty} -\frac{(\omega^2 - n^2\pi^2)}{n^2\pi^2}. \end{aligned} \tag{4.58}$$

Finding an expansion for $Q(\omega)$ is a little more involved. We know that there are an infinite number of zeros spaced along the real line, located at $\omega = \pm\omega_n$, for $n = 0, 1, 2, \ldots$. These branch points are indexed so that, for positive n, $\omega = \omega_n$ is to the right of $\omega = n\pi$. This has the consequence that $\omega = -\omega_n$ is to the left of $\omega = -n\pi$. It is important to note that the function $Q(\omega)$ is even and smooth. This means two things, firstly that $Q'(0) = 0$. Secondly, it means that the zeros are placed symmetrically, so that positive and negative zeros may be matched up to simplify the product. This gives

$$Q(\omega) = -(1 + M) \prod_{n=0}^{\infty} \left(1 - \frac{\omega^2}{\omega_n^2}\right) \tag{4.59}$$

$$= -(1 + M) \prod_{n=0}^{\infty} -\frac{(\omega^2 - \omega_n^2)}{\omega_n^2}. \tag{4.60}$$

When the square root of these functions are taken, the location of all branch points is clear from the product decomposition. The reason this form is so useful is because it is possible isolate one branch point at a time and integrate vertically down from that chosen one. In doing this, it is clear how the function varies on either side of this branch cut.

Focusing on one branch point

We now focus in on one branch point and consider the integral along the associated cut emanating from that point. All branch cuts are chosen to run vertically downward

from the branch point on the real line to negative infinity. We begin by focusing in on the integral along the branch cut emanating from $\omega = \omega_m$, for some m. The procedure for branch cuts emanating from $m\pi$ is similar so will not be outlined here. By using the product decomposition given in (4.60), the value of $\sqrt{Q(\omega)}$ on either side of the cut may be evaluated

$$\sqrt{Q(\omega)}_m^{\pm} = \left\{ i(1+M)^{1/2} \left(1+\frac{\omega}{\omega_m}\right)^{1/2} \prod_{n\neq m} \left(1-\frac{\omega^2}{\omega_n^2}\right)^{1/2} \right\} \left(1-\frac{\omega}{\omega_m}\right)_{\pm}^{1/2} \tag{4.61}$$

$$= \left\{ \frac{(1+M)^{1/2}}{\omega_m^{1/2}} \left(1+\frac{\omega}{\omega_m}\right)^{1/2} \prod_{n\neq m} \left(1-\frac{\omega^2}{\omega_n^2}\right)^{1/2} \right\} (\omega-\omega_m)_{\pm}^{1/2}, \tag{4.62}$$

where the subscript $\pm$ indicates reference to the value just to the right or just to the left of the cut. The expression in the curly brackets does not vary on either side of the cut associated with ω_m. This is true because whichever side of the cut is considered, we remain either to the left or to the right of every other cut. To simplify the notation, the function $K_m(\omega)$ is introduced for the expression inside the curly brackets,

$$K_m(\omega) = \frac{(1+M)^{1/2}}{\omega_m^{1/2}} \left(1+\frac{\omega}{\omega_m}\right)^{1/2} \prod_{n\neq m} \left(1-\frac{\omega^2}{\omega_n^2}\right)^{1/2}. \tag{4.63}$$

This gives

$$\sqrt{Q(\omega)}_m^{\pm} = K_m(\omega)(\omega-\omega_m)_{\pm}^{1/2}. \tag{4.64}$$

To determine $\sqrt{Q(\omega)}$ on either side of the cut, $\omega - \omega_m$ is rewritten as

$$\omega - \omega_m = |\omega-\omega_m| e^{i\theta_m}, \tag{4.65}$$

where θ_m is the angle measured locally around the branch point. On the right (plus) side of the cut $\theta_m = -\pi/2$ and on the left (minus) side $\theta_m = 3\pi/2$. This gives the value of $\sqrt{Q(\omega)}$ either side of the cut to be

$$\sqrt{Q(\omega)}_m^{+} = -K_m(\omega)|\omega-\omega_m|^{1/2} e^{i3\pi/4}, \tag{4.66}$$

and

$$\sqrt{Q(\omega)}_m^{-} = K_m(\omega)|\omega-\omega_m|^{1/2} e^{i3\pi/4}. \tag{4.67}$$

The contribution from the mth cut to the the pth bead displacement may now be

evaluated and is given by

$$u_m(p,t) = \frac{\omega_*}{4\pi}\int_{\omega_m}^{\omega_m - i\infty} \frac{\sqrt{P(\omega)}e^{-i\omega t}}{(\omega^2-\omega_*^2)\omega} \times \left[\frac{\left(\cos(\omega) - \frac{M\omega}{2}\sin(\omega) + \omega\sqrt{P(\omega)}\sqrt{Q(\omega)}_m^+\right)^{-|p|}}{\sqrt{Q(\omega)}_m^+} - \frac{\left(\cos(\omega) - \frac{M\omega}{2}\sin(\omega) + \omega\sqrt{P(\omega)}\sqrt{Q(\omega)}_m^-\right)^{-|p|}}{\sqrt{Q(\omega)}_m^-}\right] d\omega. \tag{4.68}$$

Substituting (4.66) and (4.67) into this solution gives

$$u_m(p,t) = \frac{-\omega_* e^{-i3\pi/4}}{4\pi}\int_{\omega_m}^{\omega_m - i\infty} \frac{\sqrt{P(\omega)}e^{-i\omega t}}{(\omega^2-\omega_*^2)\omega K_m(\omega)|\omega-\omega_m|^{1/2}} \times \left[\left(\cos(\omega) - \frac{M\omega}{2}\sin(\omega) - \omega\sqrt{P(\omega)}K_m(\omega)|\omega-\omega_n|^{1/2}e^{i3\pi/4}\right)^{-|p|} + \left(\cos(\omega) - \frac{M\omega}{2}\sin(\omega) + \omega\sqrt{P(\omega)}K_m(\omega)|\omega-\omega_n|^{1/2}e^{i3\pi/4}\right)^{-|p|}\right] d\omega. \tag{4.69}$$

By following a similar procedure for a branch point at $\omega = m\pi$ $(m \neq 0)$, we get

$$u_{m\pi}(p,t) = \frac{-\omega_* e^{i3\pi/4}}{4\pi}\int_{\omega_m}^{\omega_m - i\infty} \frac{K_{m\pi}(\omega)|\omega-m\pi|^{1/2}e^{-i\omega t}}{(\omega^2-\omega_*^2)\omega^2\sqrt{Q(\omega)}} \times \left[\left(\cos(\omega) - \frac{M\omega}{2}\sin(\omega) - \omega\sqrt{Q(\omega)}K_{m\pi}(\omega)|\omega-m\pi|^{1/2}e^{i3\pi/4}\right)^{-|p|} + \left(\cos(\omega) - \frac{M\omega}{2}\sin(\omega) + \omega\sqrt{Q(\omega)}K_{m\pi}(\omega)|\omega-m\pi|^{1/2}e^{i3\pi/4}\right)^{-|p|}\right] d\omega,$$

where in this case $K_{m\pi}(\omega)$ is defined as

$$K_{m\pi}(\omega) = \frac{i(1+\frac{\omega}{m\pi})^{1/2}}{(m\pi)^{1/2}}\prod_{n\neq m}\left(1-\frac{\omega^2}{n^2\pi^2}\right)^{1/2}. \tag{4.70}$$

The long-time approximation of each integral

We now look at the long-time approximation for the sinusoidal loading. Again focusing on the contribution from the ω_m cut, a change of variables is made in (4.69) defined

by $\omega = \omega_m - iu$. The integral along this cut now has the form

$$\begin{aligned} u_m(p,t) = \frac{i\omega_* e^{-i3\pi/4} e^{-i\omega_m t}}{4\pi} \int_0^\infty & \frac{\sqrt{P(\omega_m - iu)} e^{-ut}}{((\omega_m - iu)^2 - \omega_*^2)(\omega_m - iu) K_m(\omega_m - iu) u^{1/2}} \\ \times \Bigg[& \Bigg(\cos(\omega_m - iu) - \frac{M(\omega_m - iu)}{2} \sin(\omega_m - iu) \\ & - (\omega_m - iu)\sqrt{P(\omega_m - iu)} K_m(\omega_m - iu) u^{1/2} e^{i3\pi/4} \Bigg)^{-|p|} \\ + & \Bigg(\cos(\omega_m - iu) - \frac{M(\omega_m - iu)}{2} \sin(\omega_m - iu) \\ & + (\omega_m - iu)\sqrt{P(\omega_m - iu)} K_m(\omega_m - iu) u^{1/2} e^{i3\pi/4} \Bigg)^{-|p|} \Bigg] du. \end{aligned} \tag{4.71}$$

The next step is to approximate this integral in the long-time limit. Due to the rapid decay of the e^{-ut} term, the long-time limit corresponds to small u. In the limit of small u, we approximate all functions of $(\omega_m - iu)$ as being evaluated at ω_m. For example

$$\cos(\omega_m - iu) \approx \cos(\omega_m). \tag{4.72}$$

Applying this approximation, the integral simplifies to

$$\begin{aligned} u_m(p,t) \approx \frac{\omega_* \sqrt{P(\omega_m)} e^{-i\pi/4} e^{-i\omega_m t}}{4\pi(\omega_m^2 - \omega_*^2)\omega_m K_m(\omega_m)} & \int_0^\infty \frac{e^{-ut}}{u^{1/2}} \\ \times \Bigg[& \Bigg(\cos(\omega_m) - \frac{M\omega_m}{2} \sin(\omega_m) \\ & - \omega_m \sqrt{P(\omega_m)} K_m(\omega_m) u^{1/2} e^{i3\pi/4} \Bigg)^{-|p|} \\ + & \Bigg(\cos(\omega_m) - \frac{M\omega_m}{2} \sin(\omega_m) \\ & + \omega_m \sqrt{P(\omega_m)} K_m(\omega_m) u^{1/2} e^{i3\pi/4} \Bigg)^{-|p|} \Bigg] du, \end{aligned} \tag{4.73}$$

where all functions of ω_m become constant. Since u is small, when the binomial expansions of the two expressions in square brackets is taken we find that

$$\begin{aligned} & \Bigg(\cos(\omega_m) - \frac{M\omega_m}{2} \sin(\omega_m) \pm \sqrt{\omega_m^2}\sqrt{P(\omega_m)} K_m(\omega_m) u^{1/2} e^{i3\pi/4} \Bigg)^{-|p|} \\ & \qquad = \Bigg(\cos(\omega_m) - \frac{M\omega_m}{2} \sin(\omega_m) \Bigg)^{-|p|} + O(u^{1/2}). \end{aligned}$$

We choose to ignore the higher order terms in this expansion since they produce $O(1)$ terms in the integrand which are negligible compared to the $O(u^{-1/2})$ terms.

Care must be taken when considering the integral in equation (4.73) since the constant in front of the integral will grow as $\omega_* \to \omega_m$. This corresponds to the forcing frequency being close to a branch point i.e. close to the edge of a stop band. The situation of forcing near a stop band edge will be considered shortly.

Considering the case when $\omega_* \not\approx \omega_m$, the integral reduces to the very simple form

$$u_m(p,t) \approx A_m\, e^{-i\omega_m t} \int_0^\infty \frac{e^{-ut}}{u^{1/2}} du, \tag{4.74}$$

where A_m is simply a constant and is given by

$$A_m = \frac{\omega_* e^{-i\pi/4}\sqrt{P(\omega_m)}\left(\cos(\omega_m) - \frac{M\omega_m}{2}\sin(\omega_m)\right)^{-|p|}}{2\pi(\omega_m^2 - \omega_*^2)\omega_m^2 K_m(\omega_m)}. \tag{4.75}$$

Since we only wish to know the asymptotic behaviour of this integral for long times, we are not primarily concerned with the actual value of this constant; however it can be evaluated numerically. By introducing the variable $v = ut$, the integral (4.74) becomes

$$u_m(p,t) \approx \frac{A_m\, e^{-i\omega_m t}}{t^{1/2}} \int_0^\infty \frac{e^{-v}}{v^{1/2}} dv. \tag{4.76}$$

Conveniently, the remaining integral is a standard integral and has the value $\sqrt{\pi}$, giving the solution

$$u_m(p,t) = \frac{A_m\sqrt{\pi}e^{-i\omega_m t}}{t^{1/2}} + O(t^{-1}). \tag{4.77}$$

Following a similar procedure for the branch points at $m\pi$ it is possible to show that the integrals behave like

$$u_{m\pi}(p,t) = \frac{A_{m\pi}\sqrt{\pi}e^{-im\pi t}}{t^{3/2}} + O(t^{-2}). \tag{4.78}$$

In this case the branch cut integrals decay like $t^{-3/2}$ in time rather than $t^{-1/2}$.

It is possible to pair up the branch cut integrals from ω_m and $-\omega_m$ (and equivalently $m\pi$ and $-m\pi$). In doing this, we get

$$u_{\pm m}(p,t) = \frac{2A_m\sqrt{\pi}}{t^{1/2}}\cos(\omega_m t), \tag{4.79}$$

where the $\pm$ symbol has been included to show that the positive and negative branch cuts are considered. Following a similar procedure for the branch cuts at $m\pi$ we have

$$u_{\pm m\pi}(p,t) = \frac{2A_{m\pi}\sqrt{\pi}}{t^{3/2}}\cos(m\pi t). \tag{4.80}$$

It has been shown that when forcing the system at a frequency away from the band-gap edge, the contribution of each branch cut integral decays algebraically in

time. This behaviour occurs irrespective of whether the forcing frequency is in a stop or pass band. This is unusual since in a stop band it is known that the energy is trapped close to the forcing point. How is it therefore possible to avoid a solution that grows in time in this case?

We conclude that the integrals given by the branch points represent the initial transients of the solution. This transient behaviour dies out in the long-time limit. Since this is true regardless of whether the forcing frequency is located in a stop or pass band we know that the branch cut integrals will not result in the solution blowing up. If the solution does blow up, it must either occur when the forcing frequency is close to a band edge or it must come from the pole contributions.

Now we look at the case when the forcing frequency is on the edge of a stop band. Again, consider the integral along only the mth branch cut. The forcing frequency will be equal to the stop band edge $\omega_* = \omega_m$. Under this assumption, it is no longer possible to assume $((\omega_m - iu)^2 - \omega_*^2) = (\omega_m^2 - \omega_*^2)$. In this case, the integral becomes

$$u_m(p,t) = B\, e^{-i\omega_m t} \int_0^\infty \frac{e^{-ut}}{u^{3/2}} du, \tag{4.81}$$

where

$$B = \frac{-\omega_* e^{-i3\pi/4}\sqrt{P(\omega_m)}\left(\cos(\omega_m) - \frac{M\omega_m}{2}\sin(\omega_m)\right)^{-|p|}}{4\pi\omega_m\sqrt{\omega_m^2}K_m(\omega_m)}. \tag{4.82}$$

Applying the same change of variables $v = ut$ to (4.81) we get

$$u_m(p,t) = t^{1/2} B\, e^{-i\omega_m t} \int_0^\infty \frac{e^{-v}}{v^{3/2}} dv. \tag{4.83}$$

Clearly this solution will grow in time since, as before, the integral evaluates to $\sqrt{\pi}$. Following a similar procedure for the branch points at $\omega = m\pi$ gives decay in time of order $O(t^{-1/2})$ when $\omega_* = m\pi$.

When the forcing frequency is close to the stop band (but not equal to it) then we expect initially to experience growth in the solution. Once sufficient time has passed, the solution is then expected to decay as before.

It is concluded that the solution grows indefinitely in time when the forcing frequency is at to the edge of a stop band at $\omega = \omega_m$ (but not $\omega = m\pi$). A resonant phenomenon is experienced such that the bead at the origin is moving in the same direction as the applied force. It is interesting to note that there is no growth in time resulting from the branch cut integrals at $\omega = m\pi$.

4.5.2 The contribution from the poles

We now investigate the contribution from the two poles at $\omega = \pm\omega_*$. These poles are introduced by the forcing term $F(\omega)$. It is expected that these poles will give rise to the wave like solution that will dominate in the long-time limit. To investigate the contribution from these poles we cast our minds back to the form of the solution given by (4.51)

$$\begin{aligned} u(p,t) &= \frac{\omega_*}{4\pi}\int_{-\infty}^{\infty} \frac{\sin(\omega)\left(\cos(\omega) - \frac{M\omega}{2}\sin(\omega) + \sqrt{G(\omega)}\right)^{-|p|} e^{-i\omega t}}{\omega(\omega^2-\omega_*^2)\sqrt{G(\omega)}}\, d\omega \\ &= \frac{\omega_*}{4\pi}\int_{-\infty}^{\infty} \frac{\sin(\omega)(z_*^+)^{-|p|}e^{-i\omega t}}{\omega(\omega^2-\omega_*^2)(z_*^+ - z_*^-)}\, d\omega. \end{aligned} \tag{4.84}$$

This integral has two poles located at $\omega = \pm\omega_*$. The contributions due to these poles we denote $u_{\omega_*}(p,t)$ and are found by summing up the residues for $\omega = \pm\omega_*$, i.e.

$$u_{\omega_*}(p,t) = \frac{-i\,\sin(\omega_*)}{2\omega_*}\left(\frac{(z_*^+(\omega_*))^{-|p|}\, e^{-i\omega_* t}}{z_*^+(\omega_*) - z_*^-(\omega_*)} - \frac{(z_*^+(-\omega_*))^{-|p|}\, e^{i\omega_* t}}{z_*^+(-\omega_*) - z_*^-(-\omega_*)}\right). \tag{4.85}$$

The solution is denoted u_{ω_*} to avoid confusion with the contributions from the branch cut integrals.

Recall from figure 4.4 and the discussion surrounding z_* in section 4.3.3 that

$$z_*^+(-\omega) = \overline{z_*^-(-\omega)} = z_*^-(\omega) = \overline{z_*^+(\omega)}, \qquad \text{in a pass band,} \tag{4.86}$$

$$z_*^+(-\omega) = z_*^+(\omega) = \frac{1}{z_*^-(\omega)} = \frac{1}{z_*^-(-\omega)}, \qquad \text{in stop band,} \tag{4.87}$$

where the bar denotes complex conjugation. Using these facts the pole contribution, (4.85), is rearranged into separate forms for stop bands and pass bands

$$u_{\omega_*} = \frac{-i\sin(\omega_*)}{2\omega_*(z_*^+ - z_*^-)}\left((z_*^+(\omega_*))^{-|p|}e^{-i\omega_* t} + \left(\overline{z_*^+(\omega_*)}\right)^{-|p|} e^{i\omega_* t}\right), \quad \text{in a pass band,} \tag{4.88}$$

$$u_{\omega_*} = \frac{-i\sin(\omega_*)}{2\omega_*(z_*^+ - z_*^-)}\left((z_*^+(\omega_*))^{-|p|}e^{-i\omega_* t} - \left(z_*^+(\omega_*)\right)^{-|p|} e^{i\omega_* t}\right), \qquad \text{in stop band.} \tag{4.89}$$

Since, from (4.26), $z_*^{\pm} = e^{\mp ik_*}$ the solution can be written in terms of the effective

wavenumber

$$u_{\omega_*} = -\frac{\sin(\omega_*)}{2\omega_* \sin(k_*)} \cos(\omega_*(\gamma|p| - t)), \qquad \text{in a pass band,} \tag{4.90}$$

$$u_{\omega_*} = -\frac{i \sin(\omega_*)}{2\omega_* \sin(k_*)} e^{-\Im(k_*)|p|} \sin(\omega_* t), \qquad \text{in stop band.} \tag{4.91}$$

Recall that $\gamma = k_*/\omega_*$ is the reciprocal of the effective wave speed. The contribution from the pole at the origin simply adds a constant term, which counteracts the jump in displacement that would occur from (4.90).

It is now clear that the poles at $\omega = \pm\omega_*$ give the wave-like solution. In a pass band, the solution is given by the travelling wave in (4.90). Alternatively, in a stop band, the solution is given by the evanescent field in (4.91). Note that the term $e^{-\Im(k_*)|p|}$ causes exponential decay of the solution with bead position moving away from the forcing point. This is as expected since it is known that waves are unable to propagate in a stop band.

4.6 Energy input to the system

It is known that when exciting a periodic system in a stop band, energy cannot propagate out in the form of waves. When forcing this system one may therefore expect the solution to grow at the origin as the input energy cannot propagate away from the origin. However, since the branch cut contributions given by (4.77) and (4.78) decay in time, and the pole contribution given by (4.85) is bounded, this is not observed here. The solution only grows when the system is excited at the lower edge of a stop band. In order to understand how it is possible to excite a periodic system in a stop band without the solution blowing up in time, we study the energy input into the system. We do this by calculating the work done on the bead at the origin.

To recap, provided the forcing frequency is away from the edge of a band gap, the long-time solution is given by

$$u(p,t) = \sum_{m=0}^{\infty} \frac{2A_m\sqrt{\pi}}{t^{1/2}} \cos(\omega_m t) - \frac{\sin(\omega_*)}{4\omega_* \sin(k_*)} \cos(\omega(\gamma|p| - t)) + O(t^{-1}) \tag{4.92}$$

in a pass band, and

$$u(p,t) = \sum_{m=0}^{\infty} \frac{2A_m\sqrt{\pi}}{t^{1/2}} \cos(\omega_m t) - \frac{i \sin(\omega_*)}{4\omega_* \sin(k_*)} e^{-\Im(k_*)|p|} \sin(\omega_* t) + O(t^{-1}) \tag{4.93}$$

in a stop band. The terms inside the sum give the branch cut integrals and the term outside gives the contribution from the poles.

The work done on the bead at the origin between times t_1 and t_2 is defined as

$$W = \int_{t_1}^{t_2} f_0(t) \left.\frac{\partial u}{\partial t}\right|_{p=0} dt, \tag{4.94}$$

where $f_0(t)$ is the forcing, which in the example used here is given by $f_0(t) = \sin(\omega_* t)$. Choosing to take the work done over one cycle starting at time T we set $t_1 = T$ and $t_2 = T + 2\pi/\omega_*$.

First let us take a look at the work done due to the branch cut integrals. As before, we will focus on the integral emanating from ω_m, with the integrals from $m\pi$ being very similar. Differentiating (4.79) and evaluating at $p = 0$ we have

$$\left.\frac{\partial u_{\pm m}}{\partial t}\right|_{p=0} = -2A_m^0\sqrt{\pi}\left(\frac{\omega_m \sin(\omega_m t)}{t^{1/2}} + \frac{\cos(\omega_m t)}{2\,t^{3/2}}\right), \tag{4.95}$$

where A_m^0 denotes the value of A_m evaluated at $p = 0$. With this in mind, the work done for this branch integral is given by

$$W_{\pm m} = -2A_m^0\sqrt{\pi}\int_T^{T+2\pi/\omega_*} \frac{\omega_m \sin(\omega_m t)\sin(\omega_* t)}{t^{1/2}} + \frac{\cos(\omega_m t)\sin(\omega_* t)}{2\,t^{3/2}}\, dt. \tag{4.96}$$

This integral may be rewritten in terms of Fresnel integrals. Alternatively we can show that the integral decays in the long-time limit by noting that

$$\int_T^{T+2\pi/\omega_*} \frac{\sin(\omega_m t)\sin(\omega_* t)}{t^{1/2}}\, dt < \int_T^{T+2\pi/\omega_*} \frac{1}{t^{1/2}}\, dt = 2\left((T + 2\pi/\omega_*)^{1/2} - T^{1/2}\right). \tag{4.97}$$

Using the binomial expansion on the square root term, it is possible to show that

$$\int_T^{T+2\pi/\omega_*} \frac{\sin(\omega_m t)\sin(\omega_* t)}{t^{1/2}}\, dt < \frac{2\pi}{\omega_* T} + O\left(T^{-2}\right) \to 0 \ \text{ as } \ T \to \infty. \tag{4.98}$$

Therefore the work done from each branch cut integral decays as $T \to \infty$, concluding that the branch cut integrals make no contribution to the energy input into the system in the long-time limit.

Focusing on the contribution from the pole, we begin by considering the solution in a pass band given by (4.90). Differentiating this, we get

$$\left.\frac{\partial u_{\omega_*}}{\partial t}\right|_{p=0} = \frac{\sin(\omega_*)}{4\sin(k_*)}\sin(\omega_* t), \tag{4.99}$$

leading to the work done being given by

$$W_{\omega_*} = \frac{\sin(\omega_*)}{4\sin(k_*)} \int_T^{T+2\pi/\omega_*} \sin^2(\omega_* t) dt$$
$$= \frac{\pi \sin(\omega_*)}{4\omega_* \sin(k_*)}. \tag{4.100}$$

This shows that when the system is forced in a pass band, at large times a constant amount of energy is put into the system per cycle. This is to be expected since the travelling waves transport energy away from the origin at a constant rate.

Now focusing on the solution in the stop band, given by (4.91), this is differentiated to give

$$\left.\frac{\partial u_{\omega_*}}{\partial t}\right|_{p=0} = -\frac{i\sin(\omega_*)}{4\sin(k_*)} \cos(\omega_* t). \tag{4.101}$$

The work done per cycle in a stop band is thus given by

$$W_{\omega_*} = -\frac{i\sin(\omega_*)}{4\sin(k_*)} \int_T^{T+2\pi/\omega_*} \sin(\omega_* t)\cos(\omega_* t) dt$$
$$= 0. \tag{4.102}$$

This implies that over each cycle, in a stop band, we are putting no additional energy into the system in the long-time limit. This explains how it is possible to force the system without the size of the bead displacements growing.

The question remains, if a force is applied indefinitely how can adding energy into the system be avoided? The answer to this question is that the bead at the origin is not always travelling in the same direction as the force. When the bead is travelling in the opposite direction to the force, negative work is done implying that whatever is applying the force is retrieving energy. In the case of a stop band, in the long-time limit the energy being put in exactly balances the energy being given back over each cycle.

4.7 Results

In this section we will look at both the bead displacements and the energy input into the system. We aim to see how these change when the forcing frequency is in a pass band, in a stop band and at a frequency between these. To capture these zones, four forcing frequencies have been chosen

- $\omega_* = 2\pi/5$ - a point in the middle of the first pass band,
- $\omega_* = 2.15\ldots$ - the point at the edge between the first pass band and first stop band,
- $\omega_* = 2\pi/2.5$ - a point in the middle of the first stop band,
- $\omega_* = \pi$ - the point at the edge between the first stop band and second pass band.

In figures 4.7 - **??** the displacements of the eleven beads closest to the origin are plotted. The displacements are calculated at a finite time as described in section 4.4. These figures confirm that the behaviour predicted in the long-time limit, given by equations (4.90) and (4.91), occurs in the finite time case.

We then look at the work done on the bead at the origin to compare the long-time estimate, given by (4.100) and (4.102), to that found at a finite point in time. The work done between any two points in time is given by equation (4.94). The instantaneous rate of work done is defined by

$$\frac{\partial W}{\partial t} = f_0(t)\left.\frac{\partial u}{\partial t}\right|_{p=0}. \tag{4.103}$$

For the finite time case, the work done over each cycle is considered and evaluated at the end of a cycle.

In figure 4.7 the response when the bead is forced at a frequency $\omega_* = 2\pi/5$, in the middle of the first pass band is shown. It can be seen that fairly quickly, the solution reaches a travelling wave solution as predicted by (4.90). The work done for this frequency is plotted in figure 4.10. The instantaneous work done oscillates in time, in phase with the forcing frequency, and remains positive. The work done per cycle quickly reaches that predicted by the long-time solution in (4.100).

In figure 4.8 the response when the bead is forced at a frequency $\omega_* = 2.15\ldots$, at the edge between the first pass band and first stop band is shown. In this case, growth in the solution of order $O(t^{1/2})$ is predicted from equation (4.83). It can be seen from figure 4.8 that the finite time solution grows slowly in time. Interestingly, at $t = 16$, each successive bead is exactly out of phase with the last. The slow growth in the solution also manifests itself in the rate of work done. We can see from figure 4.11 that the instantaneous rate of work oscillates with increasing amplitude. Although the rate

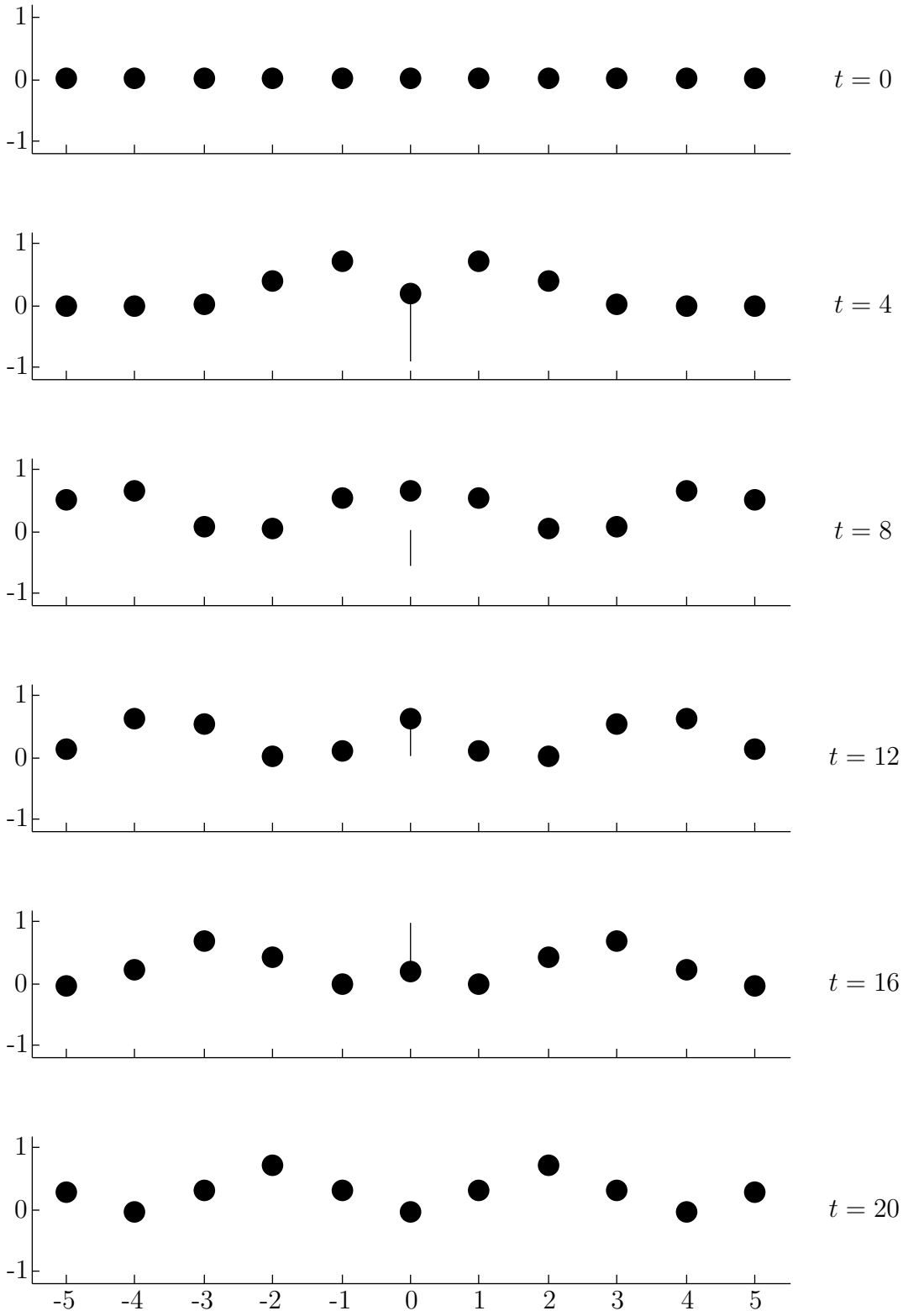

Figure 4.7: The displacements of the eleven beads closest to the origin. The dimensionless mass is $M = 0.5$ and the forcing frequency is $\omega_* = 2\pi/5$ which is in the first pass band. The magnitude of the force at each time point is illustrated by the length of the line at the origin, and its direction by whether it lies above or below zero.

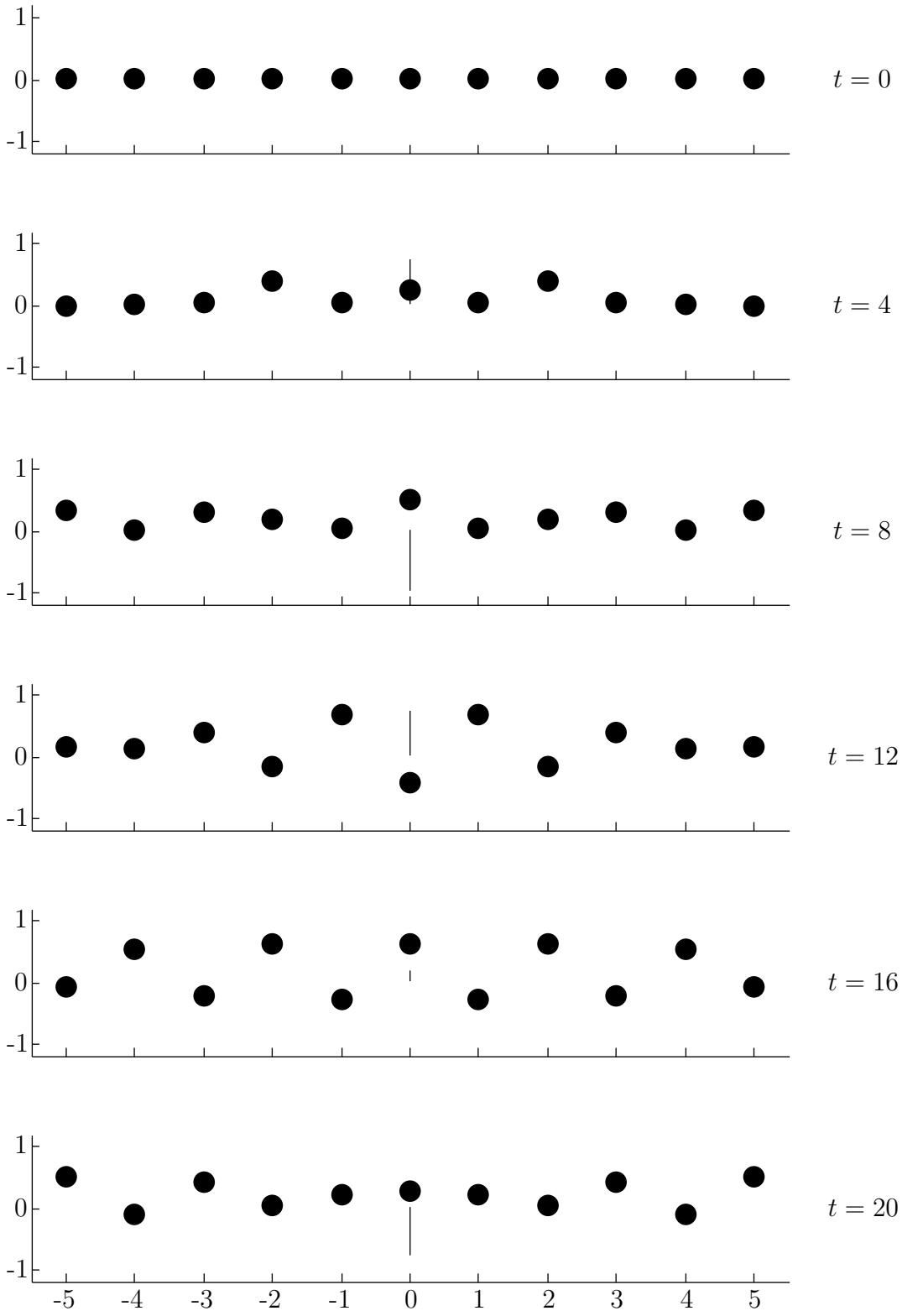

Figure 4.8: As for figure 4.7 but with forcing frequency $\omega_* = 2.15\ldots$ which coincides with the lower edge of the first stop band.

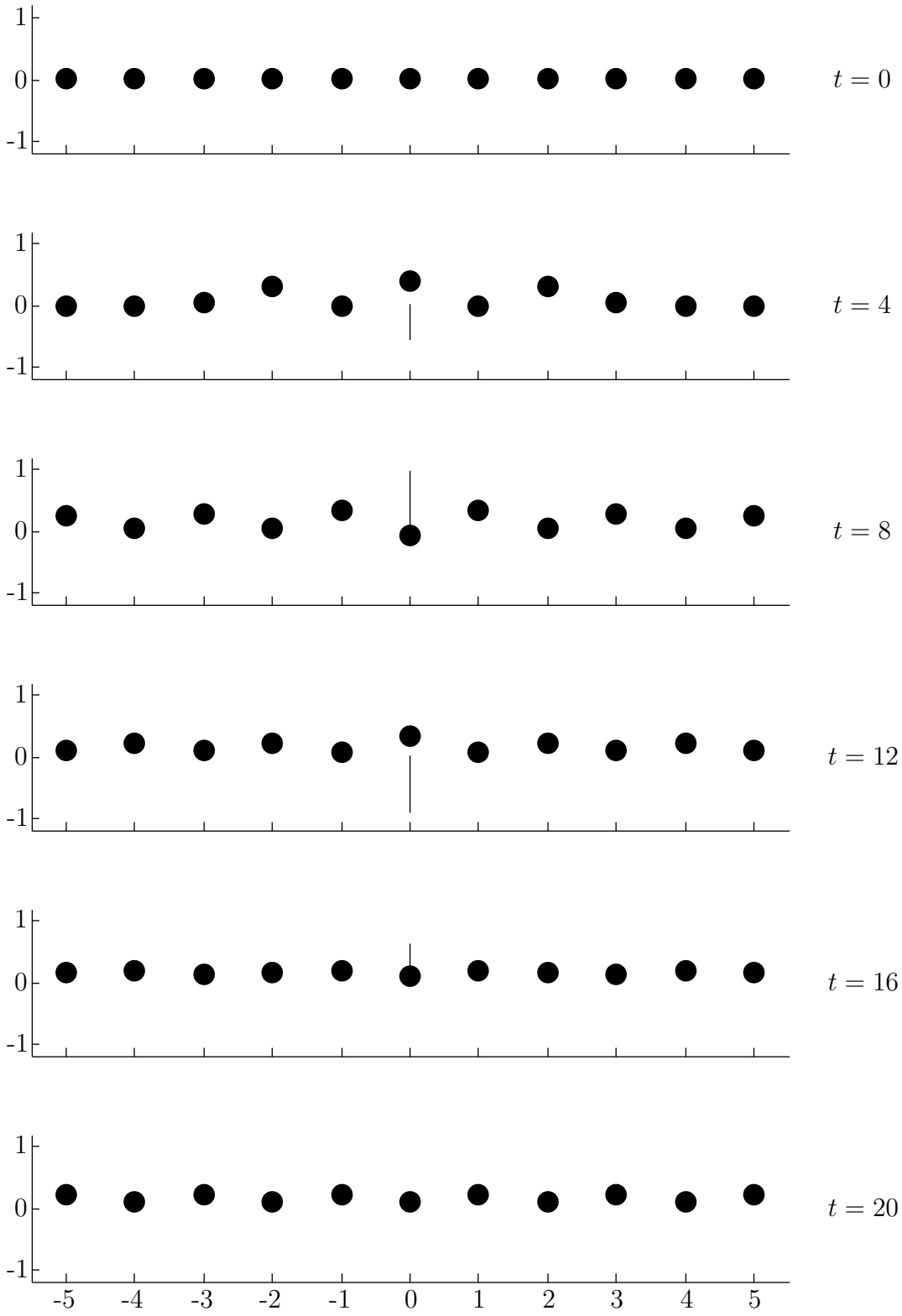

Figure 4.9: As for figure 4.7 but with forcing frequency $\omega_* = 2\pi/2.5$ which coincides with the first stop band.

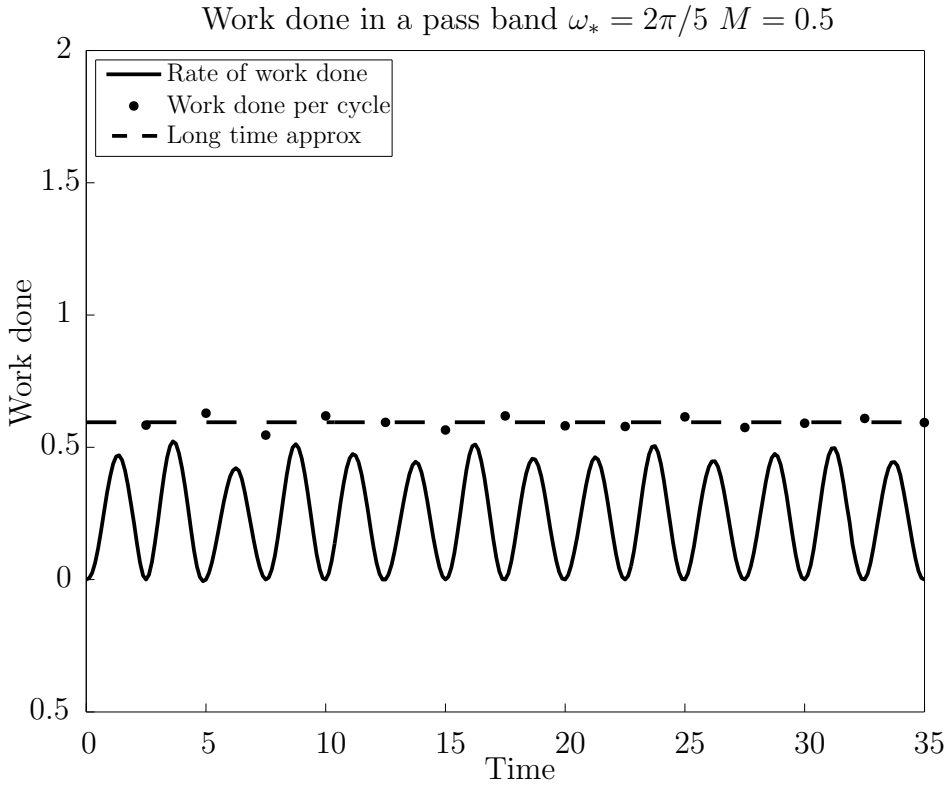

Figure 4.10: The work done in the first pass band. The mass is $M = 0.5$ and the forcing frequency is $\omega_* = 2\pi/5$.

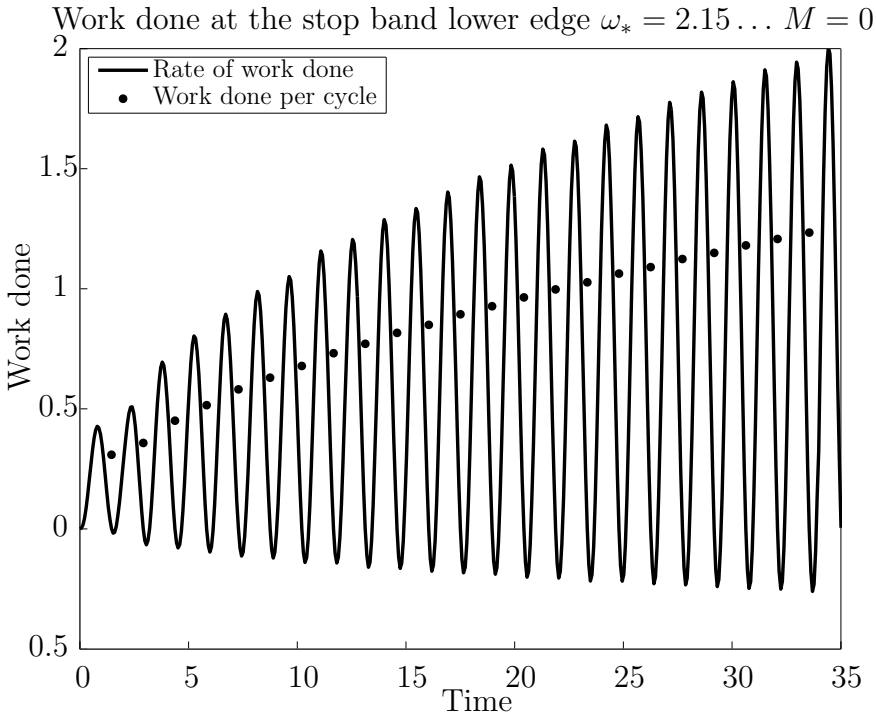

Figure 4.11: The work done when forced at the edge between the first pass band and first stop band. The mass is $M = 0.5$ and the forcing frequency is $\omega_* = 2.15\ldots$.

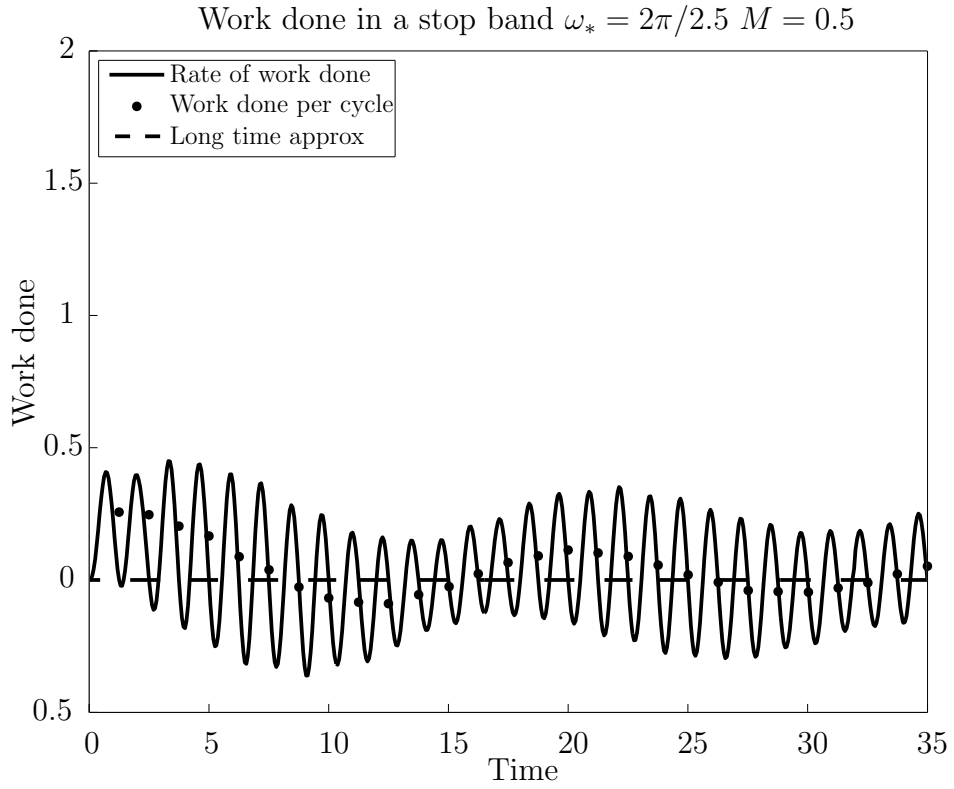

Figure 4.12: The work done in the first stop band. The mass is $M = 0.5$ and the forcing frequency is $\omega_* = 2\pi/2.5$.

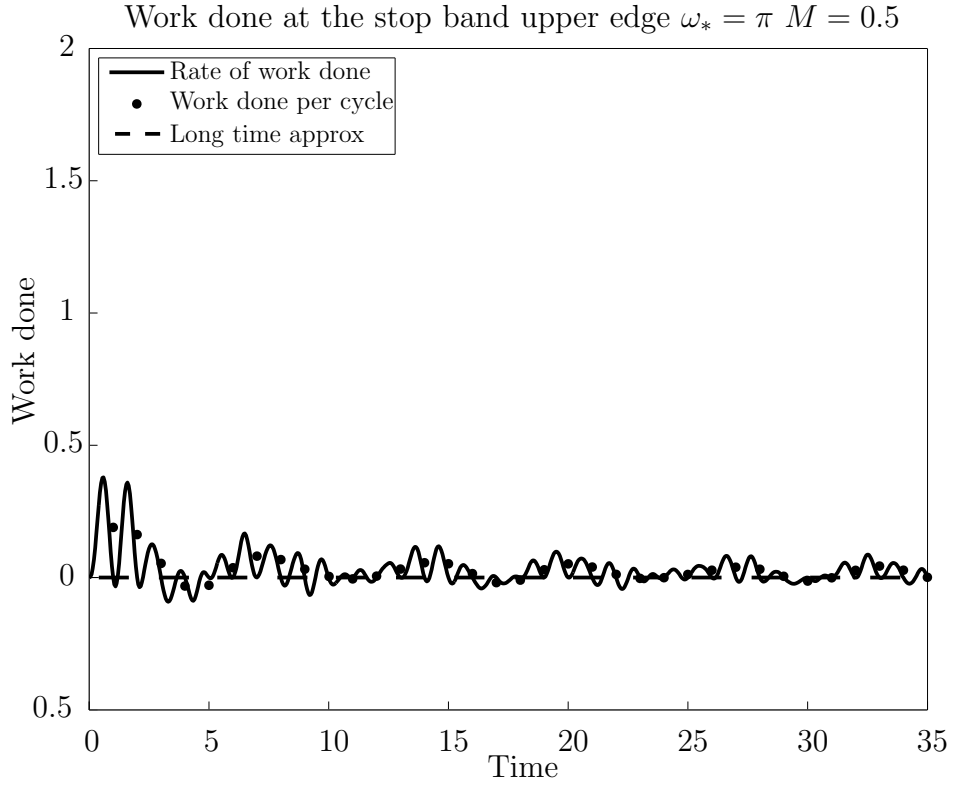

Figure 4.13: The work done when forced at the edge between the first stop band and second pass band. The mass is $M = 0.5$ and the forcing frequency is $\omega_* = \pi$.

of work does become negative at some points, it is largely positive. The work done per cycle can be seen to steadily increase with time and does not reach a constant as shown for the pass band. This confirms the long-time prediction discussed earlier

In figure 4.9 the response when the bead is forced at a frequency $\omega_* = 2\pi/2.5$, in the middle of the first stop band is shown. The solution here exhibits the expected decay in displacement of the beads further from the origin. The work done in this case is shown in figure 4.12. Although the energy input starts off having a positive value as the initial burst of energy is put into the system, the value soon becomes negative. The rate of work done then oscillates between being positive and negative, causing the work done per cycle to tend to zero. The total work done approaches a constant value.

The bead displacements for the point between the first stop band and second pass band, $\omega_* = \pi$, have not been plotted. When studied on the same scale as the other displacement plots, the bead displacements are indistinguishable from a straight line. The movement of the bead at the origin largely opposes the applied force. This is confirmed in figure 4.13 where the instantaneous work done rapidly decays to zero as no energy can get into the system.

Clearly there is a marked difference between forcing at either edge of the stop bands. At the lower edge, relatively large displacements are obtained as we hit the resonant growth discussed at the very end of section 4.5.1. At the upper edge, almost zero displacement for all beads is observed. This pattern is repeated for higher frequencies, the lower edge of the stop band always exhibits slow growth whilst at the upper edge almost no displacement is observed.

It is also interesting to note that the rate of work essentially remains positive in a pass band whereas in a stop band the rate of work must become negative at some points in time. In fact, in the long-time limit, the rate of work in a stop band must be negative for enough of the time to balance out the positive work done. This implies that the key difference between a pass band and stop band is that in a pass band the bead at the origin (almost) always travels in the same direction as the forcing but in a stop band, the bead only travels in the same direction as the force half of the time.

4.8 Conclusion

In this chapter we have studied the transient response of an infinite periodic beaded string. The string and all beads were initially at rest. The bead at the origin was then forced with a prescribed loading. The chosen loading is sinusoidal in nature with the forcing frequency variable. We have explored the difference in response of the system at pass band frequencies, at stop band frequencies and at frequencies on the edges between the two regions.

The solution was found exactly in integral form by using Fourier and z transforms. The displacements of the beads have been investigated through the singularity structure of the solution. It has been found that the transient behaviour is manifested in an infinite number of branch points whilst the steady-state solution is given by two poles. In the finite time case, these branch points were converted into poles in order to give an exact solution resulting from a finite number of poles. By analysing the long-time limit of the displacements it can be seen that in all but one case, the transient response obtained from the branch cut integrals decays in time. Interestingly, on the lower edge of each stop band, the displacements grow slowly in time ($\sim O(t^{1/2})$).

It has been confirmed that travelling wave solutions are obtained in a pass band and evanescent modes in a stop band. We found that the evanescent modes that decay in space do not grow in time, despite the fact that they are being permanently forced. On the lower edge of each stop band, the solution obtained grows slowly in time. This behaviour was not observed on the upper edge.

In order to further investigate the behaviour of the solution in a stop band, the energy input into the system was investigated. It was found that in a stop band, the energy input per cycle vanishes as the system approaches the long-time limit. This explains how we are able to excite the evanescent field without it growing in time. The energy input per cycle when forced at the lower edge of the stop band seems to grow slowly along with the displacements whilst in a pass band it reaches a constant.

Further work to be done includes the study of finite pulses. It would be interesting to study a finite sinusoidal pulse in order to confirm if it travels undisturbed in a pass band and decays in a stop band. It is currently unclear what would happen at either edge of the stop band.

In order to extend this work, it would be desirable to consider the equation for laminate one-dimensional structures. At the moment it is unclear how much progress can be made analytically in this case because the discrete z transform can no longer be taken. Another area to consider is to study two-dimensional structures such as masses on a membrane.

Chapter 5

Tuning phononic crystals using a nonlinear elastic pre-stress - antiplane waves in incompressible materials

5.1 Introduction

Complex metamaterials are at the heart of modern day engineering and technology. A vast number of such materials possess intricate microstructures that are designed to create macroscopic behaviours that are non-existent in naturally occurring materials. The ability to design these materials to the creators' precise needs is greatly advantageous. It is particularly desirable to create macroscopic properties that can be tuned in real time. Predicting how the microstructure affects the macroscopic properties on a static and dynamic level is pivotal to the design and tuning of such materials.

The desire to tune periodic structures to specific needs is not new. Early work focused on problems in solid state physics and photonics [43]. Recently, research has moved into the field of elasticity and phononics. For example, Goffaux and Vigneron [26] and subsequently Wu et al. [93] and Li et al. [50] introduce tunability of a material by rotating square cylinders inside a fluid. This work was influenced by the equivalent photonic problem [92]. Lin and Huang [52] followed on from this work by rotating circular cylinders with anisotropic material properties in air.

Others have taken advantage of the tunability of phononic crystals to create wave guides. For example, in the work by Khelif [42], a crystal is tuned to a particular frequency by adjusting the geometry. A wave guide is then created at the tuned frequency by introducing defects into the crystal. This work has been followed up by Pennec et al. in [69] who studied the creation of a waveguide filter that sends selected frequencies in different directions. Similar is the work by Evgrafov et al. [15] who use computational optimisation to build a switch which can send a signal in two separate directions. The switch is actuated by applying a mechanical stress to the device. In general, all of these papers strongly rely on the tuning of the material occurring in the design and construction phase, rather than allowing real time tuning post-construction. Once manufactured these materials have a fixed dynamic range.

As a method of performing external control over a crystal, many people consider the influence of magnetic or electric fields. This allows a user to alter the band gap structure without having to mechanically interfere with the material. Robillard et al. [71], Vasseur et al. [87] and Matar et al. [55] have collectively published work on contactless tuning of phononic crystals through the influence of a magnetic field. The use of piezoelectric materials has been studied by Hou, Wu and Liu [32], Zou et al. [100] and Casadei et al. [9]; the latter two of these papers investigate band gap control. As shown by Yeh [97], it is possible to affect the elastic properties and thus the band structure of a phononic crystal through the influence of an electric field. In a similar way, electro-rheological materials are utilised by Zhou and Chen [99]. In the paper by Wu et al. [94] a one-dimensional tunable wave guide is investigated, whereby an applied electric voltage is used to control a narrow pass band filter.

Some authors have studied the effect of temperature on the elastic properties of phononic crystals. Since the temperature effect is relatively small, such materials usually involve switching caused by a phase transition. For example in the paper by Sato et al. [75], elastic waves propagating in the GHz range through a nanocomposite are examined. Material properties are altered by the act of melting and crystallisation of the nanopores. Other authors investigating temperature effects include Huang and Wu [33], Wu, Yang and Chen [95] and Jim et al. [36].

Early work on the effect of a finite deformation on the incremental wave propagation through a material was carried out in one dimension by Rogerson and Sandiford [72]

and expanded later by Parnell [65]. In the later of these papers, the stop and pass band structure is investigated with a variety of different pre-stress. The propagation of torsional waves in a pre-stressed cylinder was covered by Shearer [77]. An experimental investigation into one-dimensional structures was carried out by Feng and Liu [17]. In the paper by Kayestha [41], the propagator matrix technique is used to study the dispersion curves. Dispersion curves for beams on an elastic foundation and the effect of pre-stress are studied by Gei, Movchan and Bigoni [24]. Later, Gei [23] looked at a similar problem with quasiperiodic composites defined by Fibonacci chains. By making use of simulations, Wang and Bertoldi [91] have looked into the mechanical tunability of three-dimensional structures. This paper utilises the finite element method to find the band gap structure.

The effect of deformation induced by an electric field has been another topic of interest. For example Gei, Roccabianca and Bacca [25] studied the effect of an electric field on the stop band structure of flexural waves on a one-dimensional composite material. The studies of small amplitude, anti-plane shear waves in an elastic medium with a deformation induced by electric field were carried out by Shmuel and deBotton in one dimension [79] and Shmuel alone in two dimensions [78]. In the last two papers, no significant change in structure of the bands occurred, the deformation simply results in a rescaling of the band structure.

Further work has looked at the buckling of periodic elastic materials under large deformations. This problem was initially studied by Mullin et al. [59]. The phononic band structure was subsequently studied by Bertoldi and Boyce [4] whereas the photonic band structure was studied by Krishnan and Johnson [44]. Bertoldi and Boyce expand on their work later with Jang and others [35].

For further reading on the subject of acoustic metamaterials, the author would like to point the reader in the direction of two recently published books, the first being edited by Craster and Guenneau [11] and focused on cloaking, wave guiding and negative refraction. The second is edited by Deymier [14] and specialises in phononic crystals and periodic structures.

In this chapter the tuning of an acoustic band structure by application of a nonlinear elastic pre-stress is discussed. The phononic crystal is a two-dimensional periodic array of annular cylinders embedded in a homogeneous elastic host. Each cylinder may

be inflated by altering its internal pressure. Inspiration for using this deformation has been drawn from previous work on cloaking. Similar deformations have been used to create infinite [67, 66] and finite [68] elastic cloaks.

The theory of small-on-large is used to determine the equation governing incremental antiplane shear waves propagating through the pre-stressed medium. For further reading about the theory of small-on-large and the derivation of the incremental equations of motion see [61], [20] and [13]. Subsequently the plane-wave expansion method is used to efficiently determine the band structure. The effect of the pre-stress on this structure and the possibility of switching stop bands on and off is investigated.

5.2 Cylinder inflation

The basic phononic crystal structure is made up of a periodic array of incompressible hyperelastic annular cylinders embedded in an incompressible homogeneous host material. We consider the initial deformation discussed in some detail in the background section 2.4.2. In particular, each of the cylinders is inflated and an axial stretch (given by β) applied such that the outer radius of the cylinders remains unchanged.

Attention is restricted to the antiplane mode of propagation so that waves are polarised along the axes of the cylinders but propagate in the plane orthogonal to these axes. It is assumed that the interior of the annular cylinder is filled with an inviscid gas such that no shear waves can propagate inside this cavity. This gives traction-free conditions on the cavity boundary since no antiplane traction is imposed in the initial pre-stress. The wave field due to a single pre-stressed cavity has been found previously. It has been discovered that this pre-stressed annular cylinder creates a cloaking effect [66][68].

A diagram of the unit cell is given in figure 5.1. Within the unit cell, the cavity region is defined as $r < r_0$, the pre-stressed region is $r_0 < r < r_1$ and the stress-free, homogeneous region is $r > r_1$. We remind the reader that upper case letters refer to the undeformed configuration (R_0,R_1) and lower case letters refer to the deformed configuration (r_0,r_1). For the remainder of this chapter, the outer radius of the pre-stressed region remains unchanged by the deformation and is always given by $R_1 = r_1 = 0.45$. This unit cell is repeated in both the x and y directions as shown in figure

5.1(c).

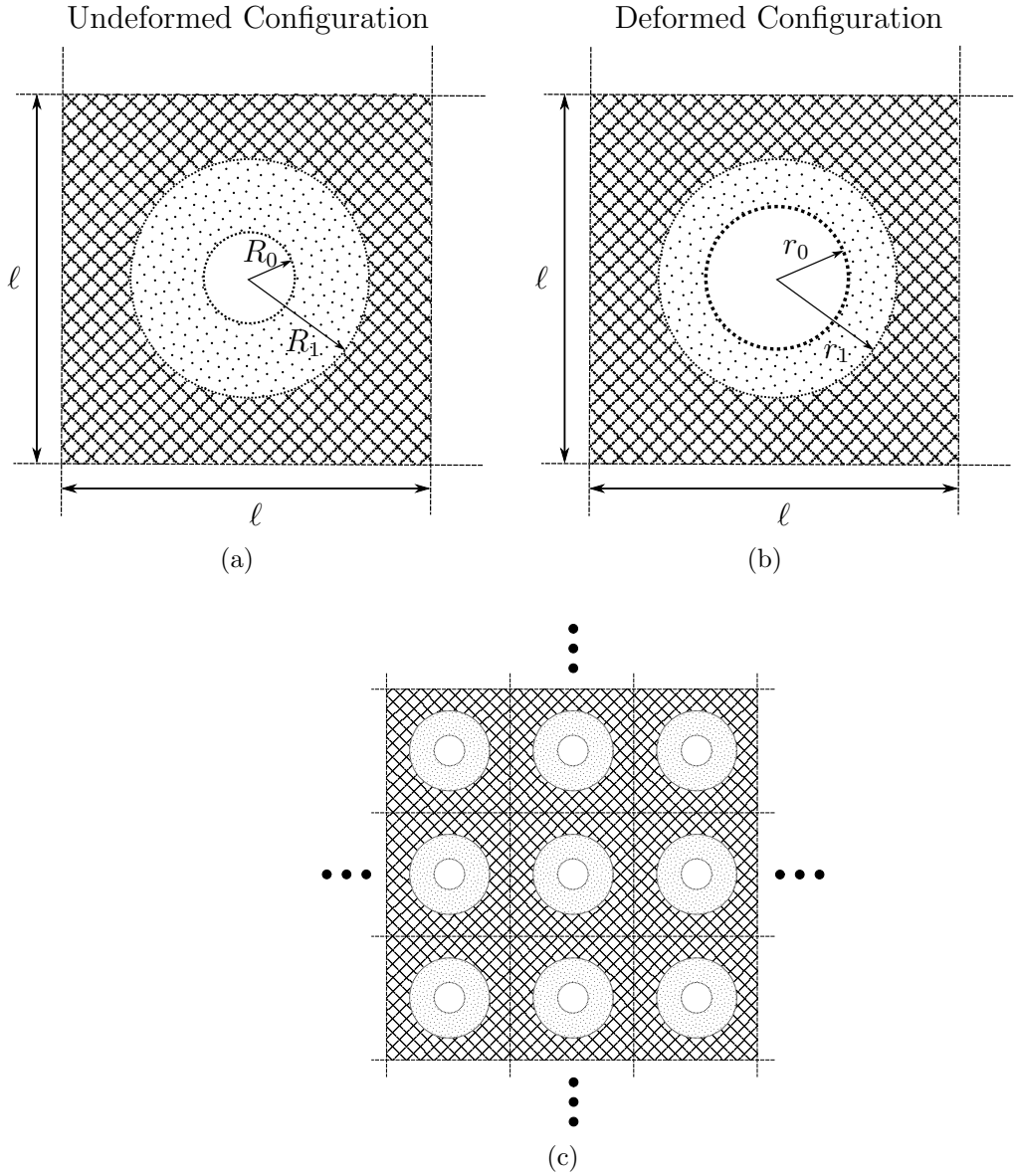

Figure 5.1: Illustration of the unit cell for (a) the undeformed configuration and (b) the deformed configuration. The cylindrical annuli are embedded in a square periodic lattice with period ℓ in a stress-free, homogeneous medium shown by the hashed pattern. The periodic medium is illustrated in (c).

In section 2.4.2 of the background chapter we discussed the principal stretches of the initial deformation. By applying the incompressibility constraint ($J = \lambda_r\lambda_\theta\lambda_z = 1$), we find that the configuration is related to the deformed radial configuration through

$$R(r) = \sqrt{\beta(r^2 + D)}, \tag{5.1}$$

where $D = (1/\beta - 1)R_1^2$. Since we are seeking a time-harmonic solution, the full

displacement, $\mathbf{u}(\mathbf{x}, t)$ is given by

$$\mathbf{u}(\mathbf{x}, t) = \Re[w(\mathbf{x})e^{-i\omega t}]\,\hat{\mathbf{k}}, \tag{5.2}$$

where $w(\mathbf{x}) = w(r, \theta)$ gives the spatial dependence of the z displacement. With this in mind, the equation governing incremental waves in the pre-stressed cylinder may be found from equation (2.187) to be

$$\frac{1}{r}\frac{\partial}{\partial r}\left(r\mu_r(r)\frac{\partial w}{\partial r}\right) + \frac{1}{r^2}\frac{\partial}{\partial \theta}\left(\mu_\theta(r)\frac{\partial w}{\partial \theta}\right) + \rho(r)\omega^2 w = 0. \tag{5.3}$$

In this equation we have used a similar scaling to equation (2.8) where the radial coordinate is scaled on the period ℓ. The shear moduli and density are scaled on the values in the host and frequency is given in the nondimensionalised form of equation (2.11). Once again, the radial and azimuthal shear moduli, $\mu_r(r)$ and $\mu_\theta(r)$ (scaled on the host moduli) and are given in the pre-stressed region by

$$\mu_r = \frac{1}{\mu_0}\frac{\lambda_r^2}{\lambda_r^2 - \lambda_z^2}\left(\lambda_r\frac{\partial W}{\partial \lambda_r} - \lambda_z\frac{\partial W}{\partial \lambda_z}\right), \tag{5.4}$$

$$\mu_\theta = \frac{1}{\mu_0}\frac{\lambda_\theta^2}{\lambda_\theta^2 - \lambda_z^2}\left(\lambda_\theta\frac{\partial W}{\partial \lambda_\theta} - \lambda_z\frac{\partial W}{\partial \lambda_z}\right). \tag{5.5}$$

For a more detailed derivation of equations (5.3)-(5.5), see [66].

5.2.1 Strain energy functions

Recall from the discussion of the strain energy functions in the background, section 2.4.3, that there are three forms of strain energy function considered in this text for incompressible materials. These are the neo-Hookean, Mooney-Rivlin and Fung.

Neo-Hookean strain energy function

For an incompressible neo-Hookean material, the strain energy function is given by [61]

$$W = \frac{\mu}{2}(\lambda_r^2 + \lambda_\theta^2 + \lambda_z^2 - 3), \tag{5.6}$$

where λ_i are the principal stretches. In this case, we can show from equations (5.4)-(5.5) that the shear moduli $\mu_r(r)$ and $\mu_\theta(r)$ are given (in the cell centred on the origin)

by

$$\mu_r(r) = \begin{cases} 0 & \text{for} \quad r < r_0, \\ \dfrac{\mu_1}{\mu_0\,\beta}\left(\dfrac{r^2+D}{r^2}\right) & \text{for} \quad r_0 < r < r_1, \\ 1 & \text{for} \quad r > r_1, \end{cases} \tag{5.7}$$

$$\mu_\theta(r) = \begin{cases} 0 & \text{for} \quad r < r_0, \\ \dfrac{\mu_1}{\mu_0\,\beta}\left(\dfrac{r^2}{r^2+D}\right) & \text{for} \quad r_0 < r < r_1, \\ 1 & \text{for} \quad r > r_1, \end{cases} \tag{5.8}$$

where μ_0 and μ_1 are the shear moduli in the host material and annulus respectively and β is the stretch along the axis. The parameter D characterises the deformation and is given by $D = (\beta^{-1} - 1)R_1^2$. The density in each region is defined by

$$\rho(r) = \begin{cases} \dfrac{\rho_{\text{Air}}}{\rho_0} & \text{for} \quad r < r_0, \\ \dfrac{\rho_1}{\rho_0} & \text{for} \quad r_0 < r < r_1, \\ 1 & \text{for} \quad r > r_1, \end{cases} \tag{5.9}$$

where similarly, ρ_0, ρ_1 and ρ_{Air} are the densities in the host material, annulus and cavity respectively.

Note that this specific deformation gives anisotropic shear moduli resulting in the differences between μ_r and μ_θ inside the annular region. If these quantities were isotropic, the problem could easily be converted back to Cartesian coordinates, giving the equivalent example discussed in the background section 2.3.3.

It is noted in [68] that in order to achieve a perfect cloaking effect, where the deformed configuration exhibits the same scattering behaviour as the undeformed, specific values for the material properties must be chosen in the annular region. In particular, one could impose that $\mu_1 = \mu_0\,\beta$ and $\rho_1 = \rho_0\,\beta$. Since we wish to observe a change in the band structure, and we are not considering cloaking effects, we do not impose these values. We will however use the cloaking values to ensure the solution technique is working as it should.

Mooney-Rivlin strain energy function

The next level of complexity in strain energy function is the Mooney-Rivlin material. This model is typically used to describe rubber like materials and is accepted as being more realistic than the neo-Hookean model. The strain energy function for a Mooney-Rivlin material is given by [61]

$$W = \frac{\mu}{2}\left(S_1(\lambda_r^2+\lambda_\theta^2+\lambda_z^2-3)+S_2(\lambda_r^2\lambda_\theta^2+\lambda_r^2\lambda_z^2+\lambda_\theta^2\lambda_z^2-3)\right), \tag{5.10}$$

where S_1 and S_2 are material constants, typically chosen empirically. In order to be consistent with linear elasticity, the constraint $S_1+S_2=1$ must hold. Note that when $S_1=1$ ($S_2=0$), the neo-Hookean case is recovered.

Again, from equations (5.4)-(5.5), we can show that for a Mooney-Rivlin material, the shear moduli $\mu_r(r)$ and $\mu_\theta(r)$ are given by

$$\mu_r(r) = \begin{cases} 0 & \text{for} \quad r<r_0, \\ \dfrac{\mu_1 T}{\mu_0\,\beta^2}\left(\dfrac{r^2+d}{r^2}\right) & \text{for} \quad r_0<r<r_1, \\ 1 & \text{for} \quad r>r_1, \end{cases} \tag{5.11}$$

$$\mu_\theta(r) = \begin{cases} 0 & \text{for} \quad r<r_0, \\ \dfrac{\mu_1 T}{\mu_0\,\beta^2}\left(\dfrac{r^2+D-d}{r^2+D}\right) & \text{for} \quad r_0<r<r_1, \\ 1 & \text{for} \quad r>r_1, \end{cases} \tag{5.12}$$

where

$$d = \frac{D\beta S_1}{T} \tag{5.13}$$

and

$$T = 1+(\beta-1)S_1. \tag{5.14}$$

Unlike neo-Hookean solids, Mooney-Rivlin materials are not able to act as perfect cloaks. For values of S_1 that are close to 1, a near cloak is achieved. We wish to investigate this material in order to see how the difference in choice of strain energy function affects the band structure.

Fung strain energy function

Since the Mooney-Rivlin strain energy function is essentially an extension of the neo-Hookean, we choose to look at a completely different form all together. The chosen form is a simplified version of the Fung strain energy function given by [21]

$$W = \frac{\mu_1}{2}\left(e^Q - 1\right), \tag{5.15}$$

where

$$Q = E_r^2 + E_\theta^2 + E_z^2, \tag{5.16}$$

$$E_k = \frac{1}{2}\left(\lambda_k^2 - 1\right) \qquad \text{for} \quad k = r, \theta, z. \tag{5.17}$$

This strain energy function is usually used to model biological tissues such as arteries.

From equations (5.4)-(5.5), the shear moduli in each region for this case are given by

$$\mu_r(r) = \begin{cases} 0 & \text{for} \quad r < r_0, \\ \dfrac{\mu_1(r^2+D)}{2\mu_0\beta r^2}\left(\dfrac{r^2+D}{\beta r^2} + \beta - 1\right)e^Q & \text{for} \quad r_0 < r < r_1, \\ 1 & \text{for} \quad r > r_1, \end{cases} \tag{5.18}$$

$$\mu_\theta(r) = \begin{cases} 0 & \text{for} \quad r < r_0, \\ \dfrac{\mu_1\beta(r^2+D)}{2\mu_0 r^2}\left(\dfrac{\beta(r^2+D)}{r^2} + \beta - 1\right)e^Q & \text{for} \quad r_0 < r < r_1, \\ 1 & \text{for} \quad r > r_1. \end{cases} \tag{5.19}$$

By investigating this material, we shall see how big differences in the nature of the strain energy function manifest in the materials response to incremental waves.

5.2.2 Conversion to Cartesian coordinates

As outlined in the background chapter, the displacement will be represented as a sum of plane waves modulated by a Bloch exponent term. In this case $w(\mathbf{x})$ in (5.3) is given by

$$w(\mathbf{x}) = e^{i\mathbf{K}\cdot\mathbf{x}} \sum_{\mathbf{G}} w_{\mathbf{G}}(\mathbf{G})\, e^{i\mathbf{G}\cdot\mathbf{x}}, \tag{5.20}$$

where $\mathbf{K}$ is the Bloch wavevector, $\mathbf{G}$ are the reciprocal lattice vectors and $w_{\mathbf{G}}$ are the Fourier coefficients of the displacement. The Fourier coefficients are the unknowns of

the problem and ultimately describe the displacement field. The sum in (5.20) is over all possible reciprocal lattice vectors given by

$$\mathbf{G} = 2\pi \left(m\,\hat{\mathbf{i}} + n\,\hat{\mathbf{j}} \right). \tag{5.21}$$

Note in equation (5.20) we have implicitly a double sum since the sum is taken over both m and n.

Since the structure of the material is periodic in Cartesian coordinates and so are the plane waves, the derivatives in equation (5.3) must first be converted into Cartesian coordinates by using

$$r\frac{\partial}{\partial r} = x\frac{\partial}{\partial x} + y\frac{\partial}{\partial y}, \tag{5.22}$$

$$\frac{\partial}{\partial \theta} = -y\frac{\partial}{\partial x} + x\frac{\partial}{\partial y}. \tag{5.23}$$

It is convenient to multiply equation (5.3) by $r^2 = x^2 + y^2$ to convert it into the following form

$$r\frac{\partial}{\partial r}\left(r\mu_r(r)\frac{\partial w}{\partial r} \right) + \mu_\theta(r)\frac{\partial^2 w}{\partial \theta^2} + r^2\rho(r)\omega^2 w = 0. \tag{5.24}$$

Replacing the polar derivatives with Cartesian, we get

$$\begin{aligned}
&\left(x^2\mu_r + y^2\mu_\theta\right)\frac{\partial^2 w}{\partial x^2} + \left(y^2\mu_r + x^2\mu_\theta\right)\frac{\partial^2 w}{\partial y^2} + \left(2xy\,\mu_r - 2xy\,\mu_\theta\right)\frac{\partial^2 w}{\partial x \partial y} \\
&\quad + \left(x^2\frac{\partial \mu_r}{\partial x} + x\mu_r + xy\frac{\partial \mu_r}{\partial y} - x\mu_\theta \right)\frac{\partial w}{\partial x} \\
&\quad + \left(y^2\frac{\partial \mu_r}{\partial y} + y\mu_r + xy\frac{\partial \mu_r}{\partial x} - y\mu_\theta \right)\frac{\partial w}{\partial y} \\
&\quad + (x^2 + y^2)\rho\omega^2 w = 0.
\end{aligned} \tag{5.25}$$

5.2.3 Recovering the isotropic case

As a brief aside, we show how the isotropic case may be retrieved by assuming that there is no difference in the shear modulus in the radial and azimuthal directions. By

setting $\mu_r = \mu_\theta = \mu$ in equation (5.25), we obtain

$$\begin{aligned}
&\left(x^2+y^2\right)\mu\frac{\partial^2 w}{\partial x^2} + \left(y^2+x^2\right)\mu\frac{\partial^2 w}{\partial y^2} + \cancel{(2xy-2xy)\mu\frac{\partial^2 w}{\partial x\partial y}} \\
&+\left(x^2\frac{\partial \mu}{\partial x} + \cancel{xy\mu} + xy\frac{\partial \mu}{\partial y} - \cancel{xy\mu}\right)\frac{\partial w}{\partial x} \\
&+\left(y^2\frac{\partial \mu}{\partial y} + \cancel{xy\mu} + xy\frac{\partial \mu}{\partial x} - \cancel{xy\mu}\right)\frac{\partial w}{\partial y} \\
&+(x^2+y^2)\rho\omega^2 w = 0.
\end{aligned} \tag{5.26}$$

Use the chain rule on the derivatives in the third and fourth terms to give

$$\begin{aligned}
&\cancel{\left(x^2+y^2\right)}\mu\frac{\partial^2 w}{\partial x^2} + \cancel{\left(y^2+x^2\right)}\mu\frac{\partial^2 w}{\partial y^2} \\
&+\cancel{\left(x^2+y^2\right)}\frac{\partial \mu}{\partial x}\frac{\partial w}{\partial x} + \cancel{\left(x^2+y^2\right)}\frac{\partial \mu}{\partial y}\frac{\partial w}{\partial y} \\
&+\cancel{\left(x^2+y^2\right)}\rho\omega^2 w = 0,
\end{aligned} \tag{5.27}$$

which may be written as

$$\frac{\partial}{\partial x}\left(\mu\frac{\partial w}{\partial x}\right) + \frac{\partial}{\partial y}\left(\mu\frac{\partial w}{\partial y}\right) + \rho\omega^2 w = 0$$

or

$$\nabla\cdot(\mu\nabla w) + \rho\omega^2 w = 0. \tag{5.28}$$

The form of equation (5.28) is the time-harmonic equivalent of equation (2.104) used previously in the background section 2.3.3. There it was shown how to solve this by finding an analytic shape function for the Fourier coefficients of μ and ρ. In the anisotropic case, an analytic shape function is not obtainable, so Fourier coefficients must be found numerically. Furthermore, since in equation (5.25) each derivative has been expanded by the chain rule, we no longer seek the Fourier coefficients of the material properties themselves, rather the Fourier coefficients for each term multiplying the w derivatives are to be found instead.

5.3 Implementation of the plane-wave expansion method

In order to tidy up the equation of motion, let us define functions $a(\mathbf{x}), \ldots, e(\mathbf{x})$ such that (5.25) is given by

$$a(\mathbf{x})\frac{\partial^2 w}{\partial x^2} + b(\mathbf{x})\frac{\partial^2 w}{\partial y^2} + c(\mathbf{x})\frac{\partial^2 w}{\partial x \partial y} + d(\mathbf{x})\frac{\partial w}{\partial x} + e(\mathbf{x})\frac{\partial w}{\partial y} + \rho\,\omega^2(x^2+y^2)w = 0. \quad (5.29)$$

Since all is known except for the displacement field and the frequency, this equation may be converted into a generalised eigenvalue problem by using the plane-wave expansion method as described in the background chapter.

We proceed by assuming the form of $w(\mathbf{x})$ is given by (5.20). Note that this satisfies the Bloch condition of being periodic across the unit cell except for the phase shift given by the Bloch term, $e^{i\mathbf{K}\cdot\mathbf{x}}$. The functions $a(\mathbf{x}), b(\mathbf{x}), \ldots, e(\mathbf{x})$ are also written as Fourier series, for example,

$$a(\mathbf{x}) = \sum_{\mathbf{G}} a_{\mathbf{G}}(\mathbf{G}) e^{i\mathbf{G}\cdot\mathbf{x}}, \quad (5.30)$$

where the coefficient $a_{\mathbf{G}}(\mathbf{G})$ is given by

$$a_{\mathbf{G}} = \int_{Cell} a(\mathbf{x}) e^{-i\mathbf{G}\cdot\mathbf{x}}\, d\mathbf{x}. \quad (5.31)$$

The functions $b(\mathbf{x}), \ldots, e(\mathbf{x})$ are represented by analogous expansions. The term involving the density is written as the Fourier series

$$\rho(\mathbf{x})(x^2+y^2) = \sum_{\mathbf{G}} \rho_{\mathbf{G}}(\mathbf{G}) e^{i\mathbf{G}\cdot\mathbf{x}}, \quad (5.32)$$

where

$$\rho_{\mathbf{G}} = \int_{Cell} \rho(\mathbf{x})(x^2+y^2) e^{-i\mathbf{G}\cdot\mathbf{x}}\, d\mathbf{x}. \quad (5.33)$$

For each of the coefficients $a_{\mathbf{G}}(\mathbf{G}), \ldots, e_{\mathbf{G}}(\mathbf{G})$, the integral given by (5.31) is performed over the central unit cell. Since this cell is centred on the origin, its boundaries run from $-1/2$ to $1/2$ in both the x and y directions. Integrals are computed by discretising the unit cell and using the `trapz` function in Matlab, performing a simple trapezoidal integration. The output of the `trapz` function was compared to others such as `dblquad`, which performs adaptive Simpson quadrature over the rectangular region. The result from `trapz` was found to be sufficiently accurate whilst taking a fraction

of the time of other options. In the case of $d_{\mathbf{G}}(\mathbf{G}), \ldots, e_{\mathbf{G}}(\mathbf{G})$ where the derivatives of the moduli are required, we have used the `gradient` function to find the slope. The reason for using the numerical gradient function, despite the prestressed shear modulus being known analytically, is because the analytic derivative involves delta functions on the boundaries of the prestressed regions. Numerous tests have been carried out comparing the numerical graient to the analytic case (where possible) and it has been concluded that the use of the `gradient` function is acceptable.

Before substituting the plane-wave expansions into (5.29), note that the derivatives of the displacement are given in series form as

$$\frac{\partial^2 w}{\partial x^2} = -e^{i\,\mathbf{K}\cdot\mathbf{x}} \sum_{\mathbf{G}} w_{\mathbf{G}}(\mathbf{G})(K_x + G_x)^2\, e^{i\,\mathbf{G}\cdot\mathbf{x}}, \tag{5.34}$$

$$\frac{\partial^2 w}{\partial y^2} = -e^{i\,\mathbf{K}\cdot\mathbf{x}} \sum_{\mathbf{G}} w_{\mathbf{G}}(\mathbf{G})(K_y + G_y)^2\, e^{i\,\mathbf{G}\cdot\mathbf{x}}, \tag{5.35}$$

$$\frac{\partial^2 w}{\partial x \partial y} = -e^{i\,\mathbf{K}\cdot\mathbf{x}} \sum_{\mathbf{G}} w_{\mathbf{G}}(\mathbf{G})(K_x + G_x)(K_y + G_y)\, e^{i\,\mathbf{G}\cdot\mathbf{x}}, \tag{5.36}$$

$$\frac{\partial w}{\partial x} = ie^{i\,\mathbf{K}\cdot\mathbf{x}} \sum_{\mathbf{G}} w_{\mathbf{G}}(\mathbf{G})(K_x + G_x)\, e^{i\,\mathbf{G}\cdot\mathbf{x}}, \tag{5.37}$$

$$\frac{\partial w}{\partial y} = ie^{i\,\mathbf{K}\cdot\mathbf{x}} \sum_{\mathbf{G}} w_{\mathbf{G}}(\mathbf{G})(K_y + G_y)\, e^{i\,\mathbf{G}\cdot\mathbf{x}} \quad . \tag{5.38}$$

Substituting the relevant form of equation (5.30) for functions $a(\mathbf{x}), \ldots, e(\mathbf{x})$ along with (5.32) and (5.34)-(5.38) into the incremental wave equation, (5.29), we get

$$\sum_{\mathbf{H}} \sum_{\mathbf{G}} \Big[a_{\mathbf{H}}(K_x + G_x)^2 + b_{\mathbf{H}}(K_y + G_y)^2 + c_{\mathbf{H}}(K_x + G_x)(K_y + G_y) - id_{\mathbf{H}}(K_x + G_x) - ie_{\mathbf{H}}(K_y + G_y) - \rho_{\mathbf{H}}\,\omega^2 \Big] w_{\mathbf{G}}\, e^{i(\mathbf{K}+\mathbf{G}+\mathbf{H})\cdot\mathbf{x}} = 0, \tag{5.39}$$

where as before $\mathbf{H}$ is used to denote the reciprocal lattice vectors associated with the material properties and $\mathbf{G}$ for those associated with the displacement. As in the Background chapter, we introduce the new wavenumber $\mathbf{G}' = \mathbf{G} + \mathbf{H}$

$$\sum_{\mathbf{G}'} \sum_{\mathbf{G}} \Big[a_{\mathbf{G}'-\mathbf{G}}(K_x + G_x)^2 + b_{\mathbf{G}'-\mathbf{G}}(K_y + G_y)^2 + c_{\mathbf{G}'-\mathbf{G}}(K_x + G_x)(K_y + G_y) - id_{\mathbf{G}'-\mathbf{G}}(K_x + G_x) - ie_{\mathbf{G}'-\mathbf{G}}(K_y + G_y) - \rho_{\mathbf{G}'-\mathbf{G}}\,\omega^2 \Big] w_{\mathbf{G}}\, e^{i(\mathbf{K}+\mathbf{G}')\cdot\mathbf{x}} = 0. \tag{5.40}$$

By introducing the change of variable, the exponential term has been separated from the sum over $\mathbf{G}$. Since this equation is true for all $\mathbf{x}$, for each $\mathbf{G}'$ the sum over $\mathbf{G}$ must

equal zero

$$\sum_{\mathbf{G}}\Big[a_{\mathbf{G}'-\mathbf{G}}(K_x+G_x)^2+b_{\mathbf{G}'-\mathbf{G}}(K_y+G_y)^2+c_{\mathbf{G}'-\mathbf{G}}(K_x+G_x)(K_y+G_y) - id_{\mathbf{G}'-\mathbf{G}}(K_x+G_x)-ie_{\mathbf{G}'-\mathbf{G}}(K_y+G_y)-\rho_{\mathbf{G}'-\mathbf{G}}\,\omega^2\Big]w_{\mathbf{G}}=0. \tag{5.41}$$

This is in the form of a generalised eigenvalue problem as before.

Equation (5.41) may now be solved for the eigenvalues ω by truncating the system and using the Matlab function `eig`. Each eigenvalue gives a different frequency mode at a given Bloch wavenumber. We typically scan around the outside edge of the irreducible Brillouin zone (as discussed in sections 2.3.3 and 2.3.4) and pick out the lowest modes. As mentioned previously, a stop band on the edge implies a stop band for all wavenumbers [86]. In the results section we follow this procedure for a number of different pre-stressed cases.

5.4 Results

5.4.1 Fourier coefficient convergence testing

The accuracy of the approximate frequencies is reliant on the convergence of the Fourier coefficients given by (5.31) and (5.33). In order for the numerical evaluation to be efficient we require that the coefficients converge quickly. That is, they must converge for a relatively low value of $|\mathbf{G}| = 2\pi\sqrt{(m^2+n^2)}$. In these calculations, it is typical to take values of m and n up to $N_{\max} = 10$. In this case, the solution is approximated using 441 plane waves, resulting in matrices of size 441×441. The size of the matrix we need to calculate and solve grows like $(2N_{\max}+1)^2$ so it is desirable to keep $N_{\max}$ low.

In this section, we briefly take a look at the convergence of the Fourier integrals. The six integrals which are of interest are the coefficients $a_{\mathbf{G}}, \ldots, e_{\mathbf{G}}$ as well as $\rho_{\mathbf{G}}$. The absolute values of these are plotted in figure 5.2. Note that each plot is given on its own scale to give more impression of the detail.

Firstly let us note that all coefficients decay as $|\mathbf{G}|$ increases. This is essential if the sums are to converge. It is observed that for the coefficients $a_{\mathbf{G}}$, $b_{\mathbf{G}}$ and $\rho_{\mathbf{G}}$ the contribution comes largely from $\mathbf{G} = \mathbf{0}$ with the absolute value decaying rapidly as

$|\mathbf{G}|$ increases. It is also noted that these coefficients play a more significant role than the coefficients $c_{\mathbf{G}}$, $d_{\mathbf{G}}$ and $e_{\mathbf{G}}$ as can be seen when considering the scale of each plot. Although the coefficients $c_{\mathbf{G}}$, $d_{\mathbf{G}}$ and $e_{\mathbf{G}}$ have less influence, they do not decay as rapidly as the others and display a more interesting structure. This implies that the value of $N_{\max}$ must be chosen to be sufficiently large in order to pick up the detail from these coefficients.

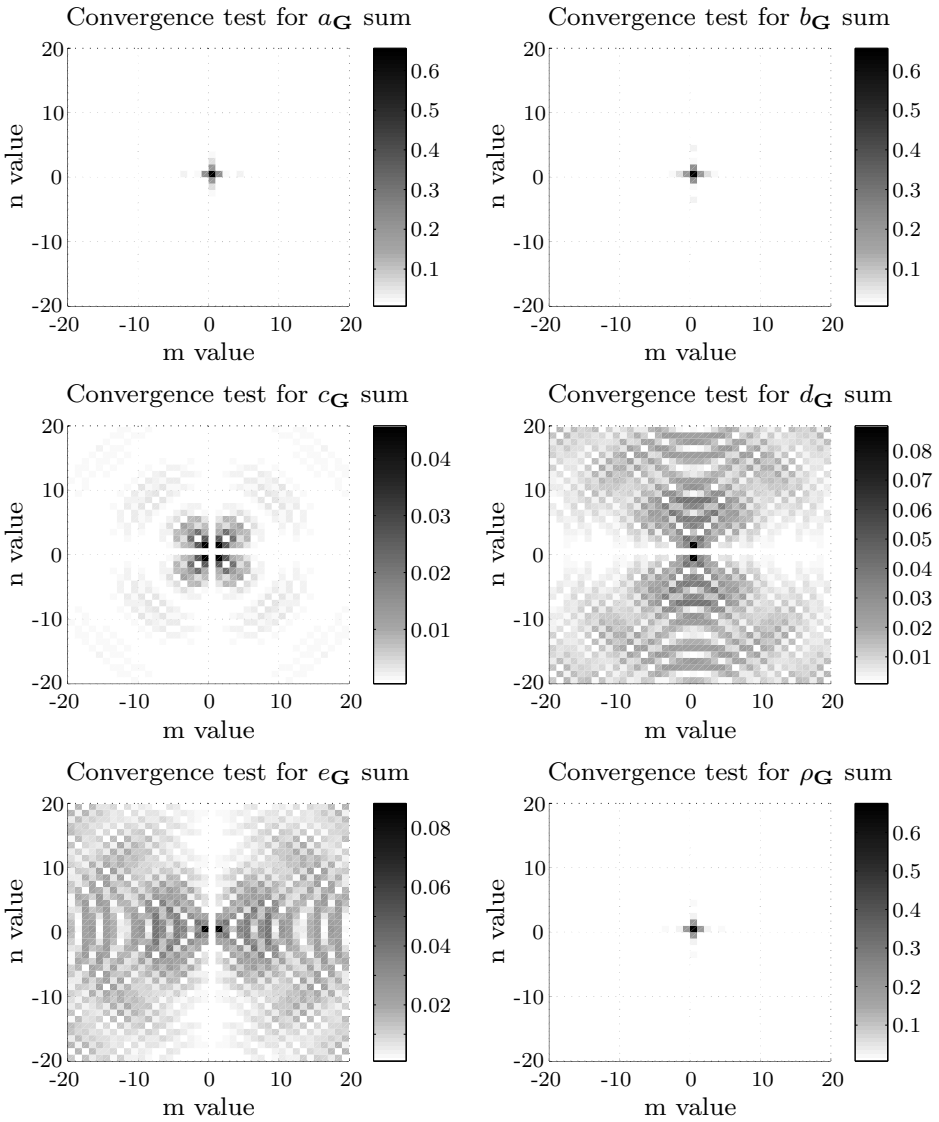

Figure 5.2: The absolute value of the six different Fourier coefficients $a_{\mathbf{G}}$ up to $\rho_{\mathbf{G}}$. The point on the axes gives the value of $\mathbf{G}$ with darker points corresponding to a greater absolute value. The axes are centred on $\mathbf{G} = \mathbf{0}$. All plots are on individual scales.

In figure 5.3 the coefficient $c_{\mathbf{G}}$ is shown for a value of $N_{\max} = 100$. For such a

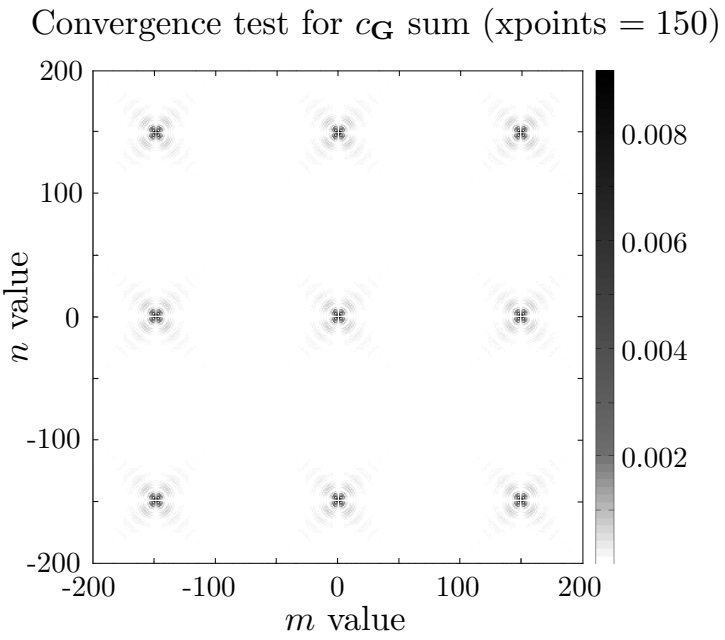

(a)

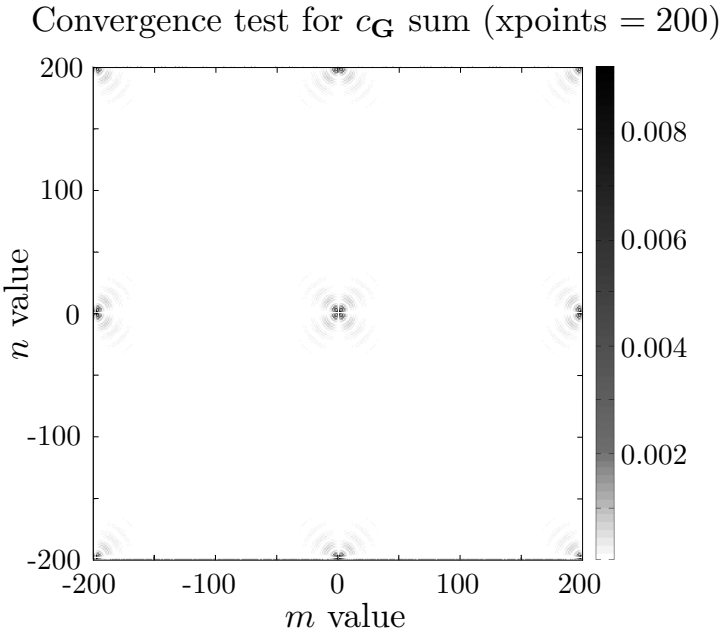

(b)

Figure 5.3: The coefficient $c_{\mathbf{G}}$ for a large value of $N_{\max} = 100$ and the number of discretisation points being (a) 150 (b) 200.

large value of $N_{\max}$, a periodic structure in the Fourier coefficient is observed. It has been discovered that this periodic structure is a numerical artefact and is a result of discretising the integration. In figure 5.3(a) 22500 discrete points have been taken to integrate over whereas in figure 5.3(b) 40000 are used. It is clear that in both cases, the value of $c_{\mathbf{G}}$ around $\mathbf{G} = \mathbf{0}$ is identical but the period at which the coefficient is

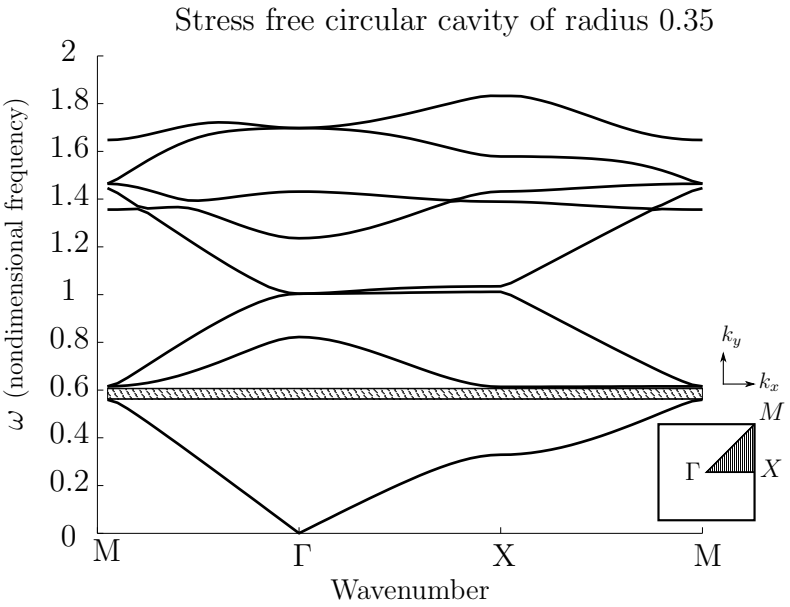

Figure 5.4: The band structure for the stress-free configuration. The lowest eight modes are shown. The irreducible Brillouin zone is shown in the bottom right of this plot. A stop band is indicated by the shaded region. The inner radius is $R_0 = 0.35$.

repeated is greater. For this reason we must ensure that the integration discretisation is taken to be fine enough with relation to $N_{\max}$ to not experience this periodic structure. This is easy done by enforcing the condition $N_{\max} < N_x/2$ where N_x is the number of discretisation points in each direction.

5.4.2 Neo-Hookean model

We begin by plotting the band structure for the stress-free configuration. For all of the results presented here we have taken the outer radii to be fixed at $R_1 = r_1 = 0.45$ and the shear modulus in the pre-stressed region to be equal to the host ($\mu_1/\mu_0 = 1$). In figure 5.4 the lowest 8 modes of the band diagram are shown. At very low frequency (on the lowest branch), the system exhibits nondispersive behaviour characterised by a constant gradient. This is to be expected since at low frequency, long waves are unable to resolve the detail of the periodic structure and an effective homogeneous medium is observed. Another interesting point to note is that all branches exhibit zero gradient on the corners of the Brillouin zone (X, Γ and M). These points of zero gradient correspond to zero group velocity and thus standing waves of the system. A naturally occurring stop band occurs for $\omega \in [0.560, 0.66]$.

Figure 5.5 shows the case of a stop band being switched on by applying an internal

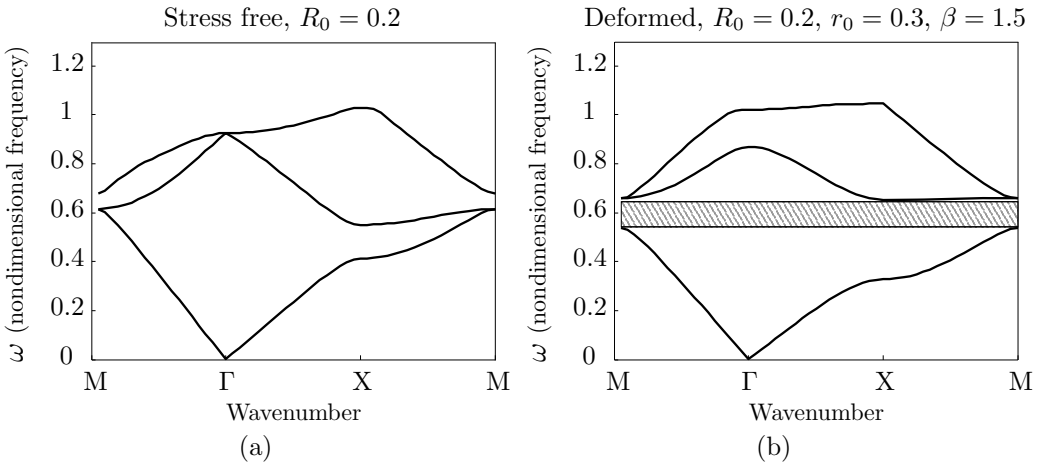

Figure 5.5: The first three modes for an initial inner radius of $R_0 = 0.2$. Figure (a) shows the stress-free configuration and (b) shows the deformed configuration corresponding to an axial stretch of $\beta = 1.5$ and deformed cavity radius $r_0 = 0.3$. A stop band is indicated by the shaded region.

pressure (accompanied by an axial stretch) and increasing the inner radius. The first three modes are plotted for an initial inner radius of $R_0 = 0.2$ in the stress-free configuration and the pre-stressed configuration corresponding to axial stretch $\beta = 1.5$ (for which the deformed inner radius is $r_0 = 0.3$). As observed, a stop band has been switched on by inflating the cavities of the material.

In figure 5.6, the opposite is shown. A naturally occurring stop band in the material is switched off by decreasing the internal pressure (accompanied by an axial contraction) and decreasing the inner radius. In this case, the first three bands are plotted for an initial radius of $R_0 = 0.35$ in the stress-free configuration alongside the first three bands for the pre-stressed configuration corresponding to axial stretch $\beta = 0.75$ (for which the deformed inner radius is $r_0 = 0.3$). In this case, an existing stop band is switched off by deflating the cavities of the material.

To investigate how the deformation affects the shape of the band structure, the pre-stressed and stress-free band diagrams are plotted together. Figure 5.7 shows the first three branches of the band diagram for the pre-stressed configuration with axial stretch $\beta = 1.5$, initial radius $R_0 = 0.2$ and deformed radius $r_0 = 0.3$ (dashed line), the stress-free configuration with cavity radius $R_0 = 0.2$ (solid line) and the stress-free configuration with cavity radius $R_0 = 0.3$ (dotted line). A similar plot is shown in figure 5.8 for the case where pre-stress switches a band gap off. In this case, the

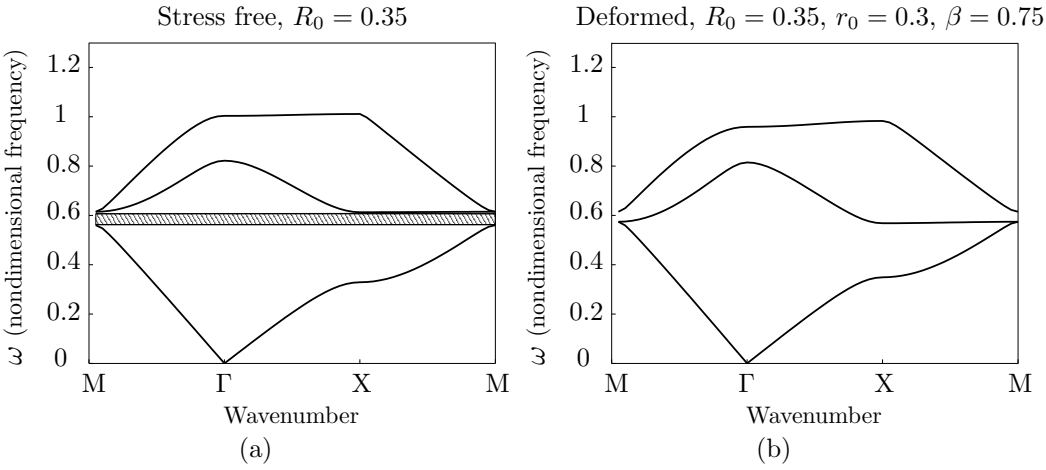

Figure 5.6: The first three modes for an initial inner radius of $R_0 = 0.35$. Figure (a) shows the stress-free configuration and (b) shows the deformed configuration corresponding to an axial stretch of $\beta = 0.75$ and deformed cavity radius $r_0 = 0.3$. A stop band is indicated by the shaded region.

band diagrams shown are the pre-stressed configuration with axial stretch $\beta = 0.5$, initial radius $R_0 = 0.35$ and deformed radius $r_0 = 0.2$ (dashed line), the stress-free configuration with cavity radius $R_0 = 0.35$ (solid line) and the stress-free configuration with cavity radius $R_0 = 0.2$ (dotted line).

From figure 5.7, a significant difference in the shape of the three band diagrams can be seen. That said, there are some regions for which the bands overlap. For example, at low frequency, the pre-stressed configuration with deformed radius $r_0 = 0.3$ (undeformed $R_0 = 0.2$) overlaps with the stress-free configuration with inner radius $R_0 = 0.3$ whilst the stress-free configuration with inner radius $R_0 = 0.2$ has a greater slope. Interestingly, although the effect of inflating the inner radius to $r_0 = 0.3$ switches on a stop band, that stop band is not existent in the stress-free solid with inner radius $R_0 = 0.3$.

Figure 5.8 shows the effect of deflating the cylinders. Once again a notable effect on the shape of the band diagram is observed. What is interesting to note here is that for low frequencies, the pre-stressed mode with deformed radius $r_0 = 0.2$ (undeformed $R_0 = 0.35$) overlaps the stress-free mode with inner radius $R_0 = 0.35$ whilst the stress-free mode with inner radius $r_0 = 0.2$ has a greater slope. This is contrary to that observed in the inflation case. The naturally occurring stop band found at inner radius $R_0 = 0.35$ is switched off both by applying the pre-stress and considering a

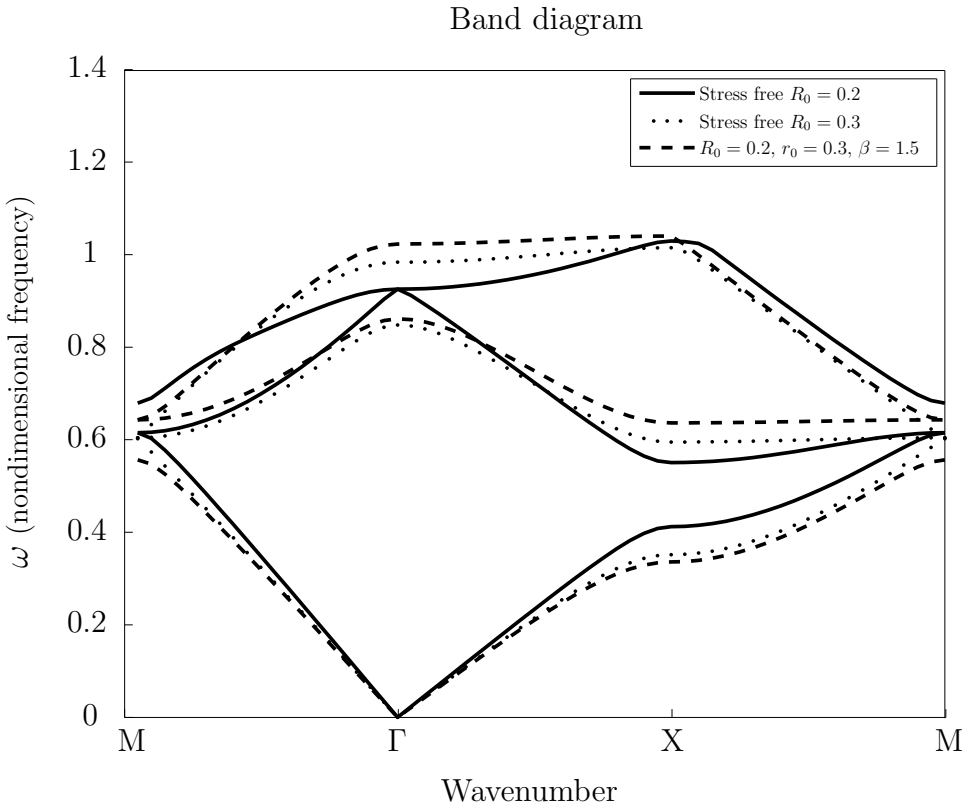

Figure 5.7: Comparison of the deformed configuration with the stress-free configuration of the same inner radius. Pre-stress is characterised by an axial stretch of $\beta = 1.5$.

stress-free material with inner radius $R_0 = 0.2$. It is concluded that the nonlinear deformation of the solid has an effect on the band diagram that more than just the result of altering the inner radius.

In figure 5.9 the width of the band gap against the cavity radius is plotted. Figure 5.9(a) shows how the band gap width changes with respect to the *undeformed* inner radius. It is observed that the onset of the band gap occurs at a smaller undeformed radius when an axial stretch (inflation) is applied. For the stress-free case, the band gap opens up at a radius of $R_0 = 0.31$ whereas for a pre-stress with axial stretch $\beta = 1.2$, the band gap opens up for an undeformed inner radius of $R_0 = 0.23$. For very large deformations (e.g. $\beta = 1.4$) a stop band is experienced for all undeformed radii.

Figure 5.9(b), shows how the band gap width varies with respect to the *deformed* inner radius. It is observed that for large initial radii ($r_0 \to R_1$), the act of applying a pre-stress has little effect when compared to the equivalent stress-free material. The line corresponding to $\beta = 1.4$ stops at $r_0 = 0.24$. This is because, from (5.1), a deformed radius less than 0.24 requires the undeformed radius to be less than zero and is therefore nonphysical. This helps to explain why for a deformation of $\beta = 1.4$,

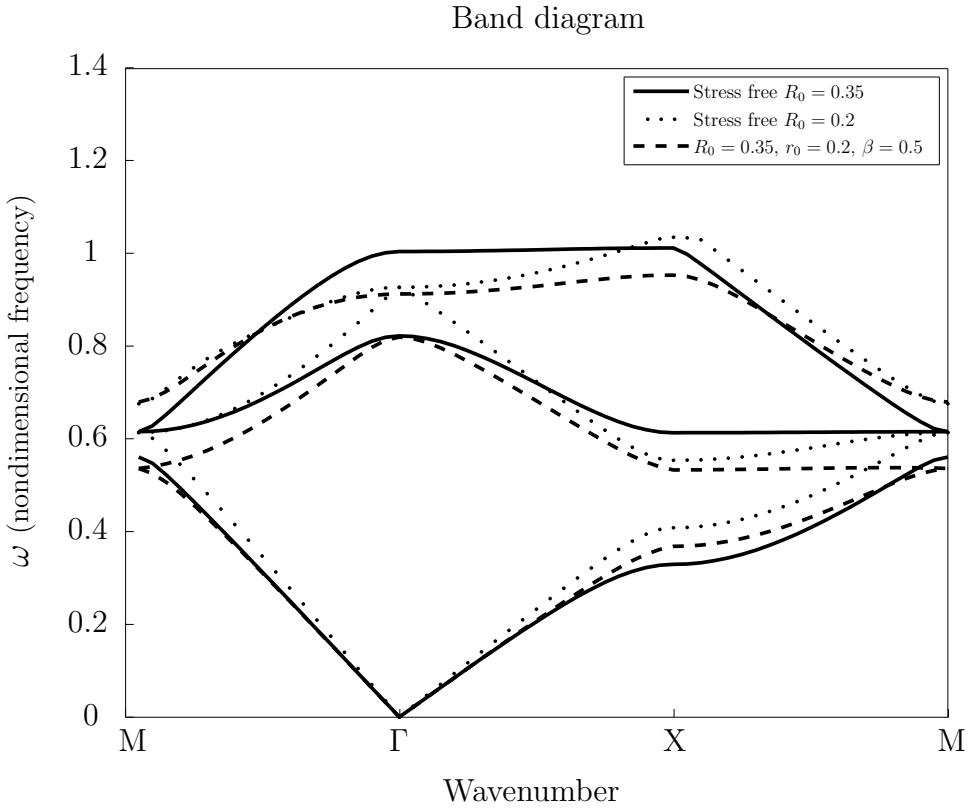

Figure 5.8: Comparison of the deformed configuration with the stress-free configuration of the same inner radius. Pre-stress is characterised by an axial stretch of $\beta = 0.5$.

a stop band is experienced for all undeformed radii. What is also interesting to note is that an additional stop band opens up when we apply an axial compression (deflation). This stop band opens up when the deformed inner radius gets close to zero but it is as yet unclear why it appears.

5.4.3 Mooney-Rivlin model

Taking a look at the effect of a Mooney-Rivlin material, figure 5.10 shows the band structure resulting from a stress-free material with radius $R_0 = 0.1$ alongside that of an inflated material, with an axial stretch of $\beta = 1.35$. The strain energy functions used are neo-Hookean, Mooney-Rivlin ($S_1 = 0.6$) and Fung. It can be seen that the Mooney-Rivlin strain energy function causes little difference in the band structure, although the stop band occurring in the neo-Hookean case is not present in the Mooney-Rivlin.

In figure 5.11 the band structure for a stress-free material with radius $R_0 = 0.36$ is plotted alongside the deformed configuration using neo-Hookean, Mooney-Rivlin ($S_1 = 0.6$) and Fung materials. In this case the deformation is given by the axial

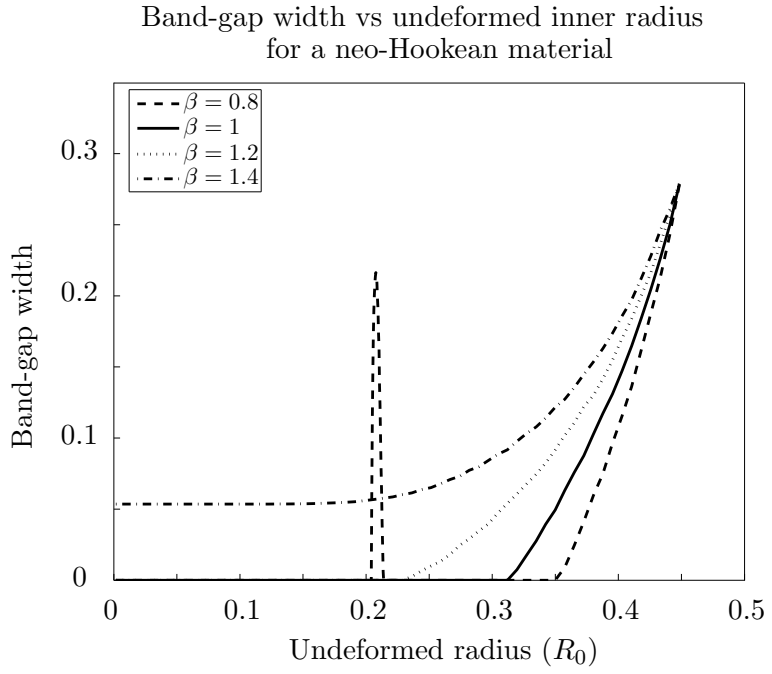

(a)

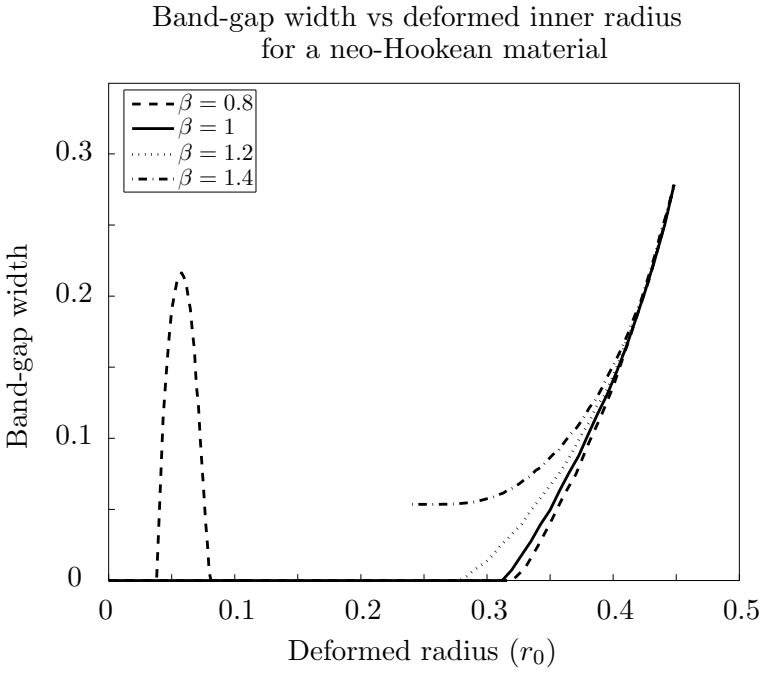

(b)

Figure 5.9: The band gap width for the stress-free and deformed configurations for a neo-Hookean solid. In figure (a) the width is plotted against the undeformed inner radius and in figure (b) the width is plotted against the deformed inner radius.

stretch $\beta = 0.8$. Again, there is little difference in the shape of the band diagram. Despite this, the Mooney-Rivlin material has switched off the stop band that was present for a neo-Hookean material.

The band gap widths for the Mooney-Rivlin material are plotted in figure 5.12 for comparison with the neo-Hookean. In agreement with the observation from the band diagrams, for a given deformation the existence of a Mooney-Rivlin material reduces the widths of the band-gaps when compared to the neo-Hookean material. Aside from that, the figures exhibit very similar behaviours.

In figure 5.13 the band gap width for a Mooney-Rivlin material for an axial stretch of $\beta = 1.4$ and various values of S_1 are plotted. The neo-Hookean case ($S_1 = 1$) is included for comparison. It is clear to see that as the parameter S_1 decreases, the effect of the pre-stress on the width is diminished. The difference is only noticeable for small radii. For initial radii above $R_0 = 0.3$ there is almost no difference between having a neo-Hookean or Mooney-Rivlin material. This is not too surprising because the smaller the initial radius, the greater deformation.

5.4.4 Fung model

From figures 5.10 and 5.11 it is observed that the Existence of a Fung material significantly alters the band diagram. In the case of axial stretch (inflation), the Fung band diagram (including the stop band) is pushed up to higher frequencies. For axial compression (deflation), the Fung band diagram (including the stop band) is pushed down to lower frequencies. In these examples, the use of a Fung material does not affect the existence or otherwise of the stop band when compared with the neo-Hookean material.

Figure 5.14 gives the band gap width for the Fung material as a function of undeformed radius. For small deformations ($\beta = 0.8$ and $\beta = 1.2$) there seems to be little effect compared to the neo-Hookean material. For larger stretches ($\beta = 1.4$) the use of a Fung material noticeably decreases the band gap width but not quite to the same extent as for the Mooney-Rivlin material.

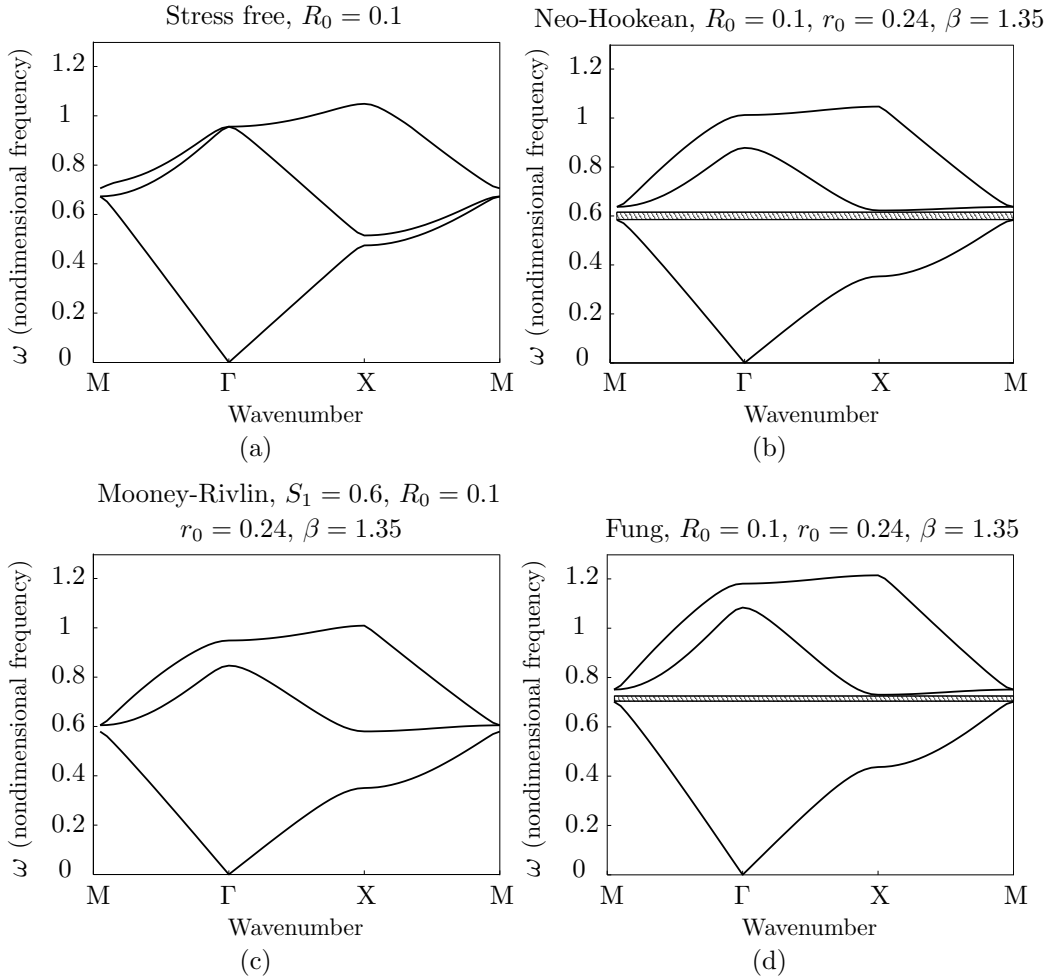

Figure 5.10: The first three modes for an initial inner radius of $R_0 = 0.1$. Pictured are the band diagrams for (a) the stress-free configuration and the deformed configuration of a (b) neo-Hookean, (c) Mooney-Rivlin ($S_1 = 0.6$) and (d) Fung material. In the deformed configuration the material experiences an axial stretch of $\beta = 1.35$ and deformed cavity radius $r_0 = 0.24$. Stop bands are indicated by the shaded regions.

5.5 Conclusion

In this chapter we have utilised the plane-wave expansion method to find the band structure of a pre-stressed hyperelastic material with a cavity. The applied pre-stress involved stretching and inflating or deflating cylindrical cavities to alter the inner cavity radius. The outer radius remained fixed throughout. The incremental wave equation was found using the small-on-large technique for a finite initial deformation. Subsequently, the plane-wave expansion method was used to efficiently determine the band gap structure of this material.

It was found that it is possible to switch on and switch off stop bands by applying

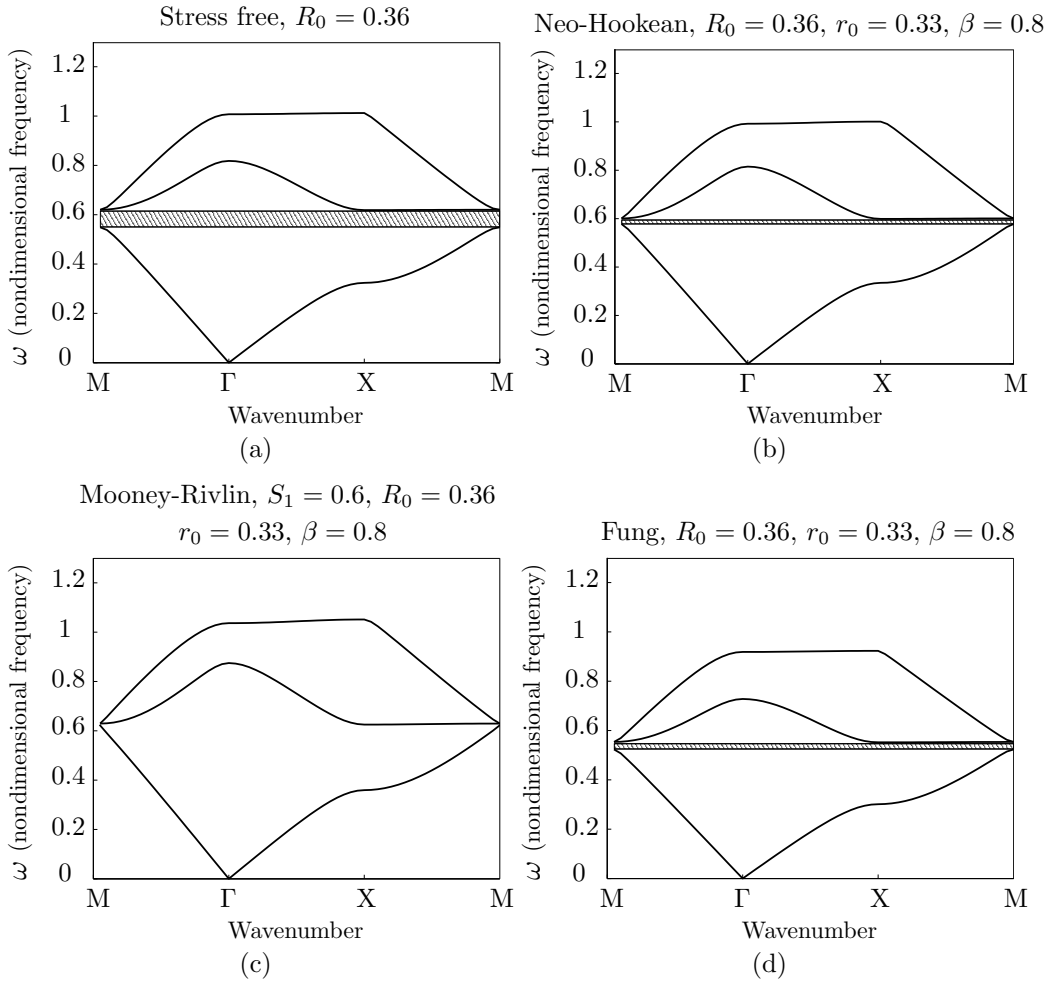

Figure 5.11: The first three modes for an initial inner radius of $R_0 = 0.36$. Pictured are the band diagrams for (a) the stress-free configuration and the deformed configuration of a (b) neo-Hookean, (c) Mooney-Rivlin ($S_1 = 0.6$) and (d) Fung material. In the deformed configuration the material experiences an axial stretch of $\beta = 0.8$ and deformed cavity radius $r_0 = 0.33$. Stop bands are indicated by the shaded regions.

a pre-stress to the material. Further, it was shown that a pre-stressed material has, in general, significantly different band structure to a stress-free material with cavity radius equal to the deformed inner radius. This reveals that the pre-stress has an effect which is more than simply changing the cavity radius. The anisotropic shear moduli induced by the deformation have a significant influence on the band structure.

The width of the band gap was studied in order to reveal how this depends on the inner radius. It was shown that an inflation of the cavity resulted in an increase of the band gap width as well as decreasing of the onset inner radius. For large deformations, a stop band was shown to be present for all possible radii.

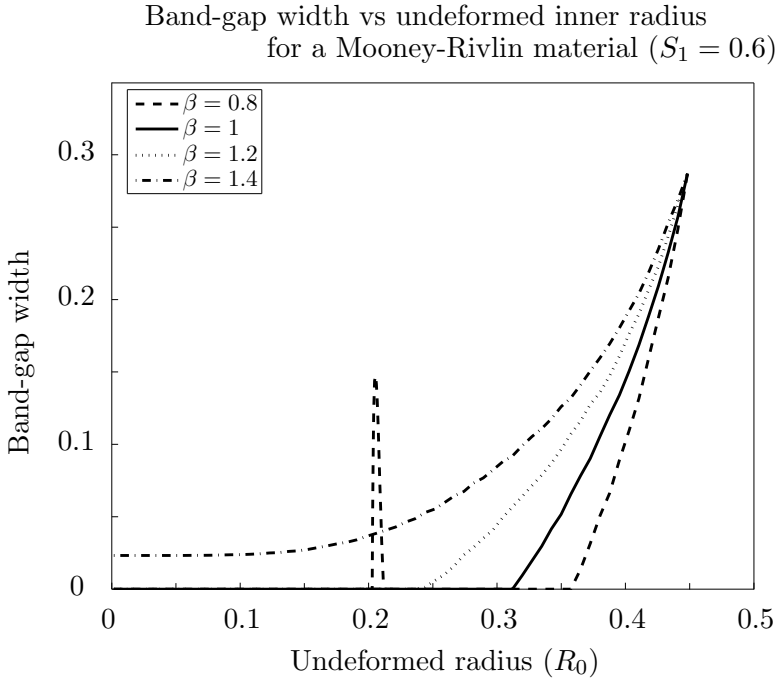

Figure 5.12: The band gap widths vs the undeformed inner radius for a Mooney-Rivlin solid with $S_1 = 0.6$.

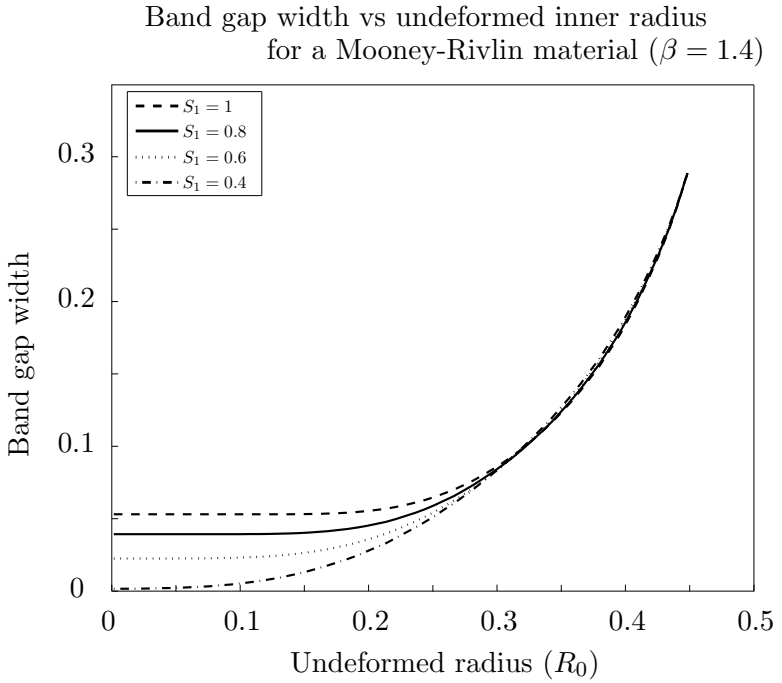

Figure 5.13: The band gap widths vs the undeformed inner radius for a Mooney-Rivlin solid with $\beta = 1.4$.

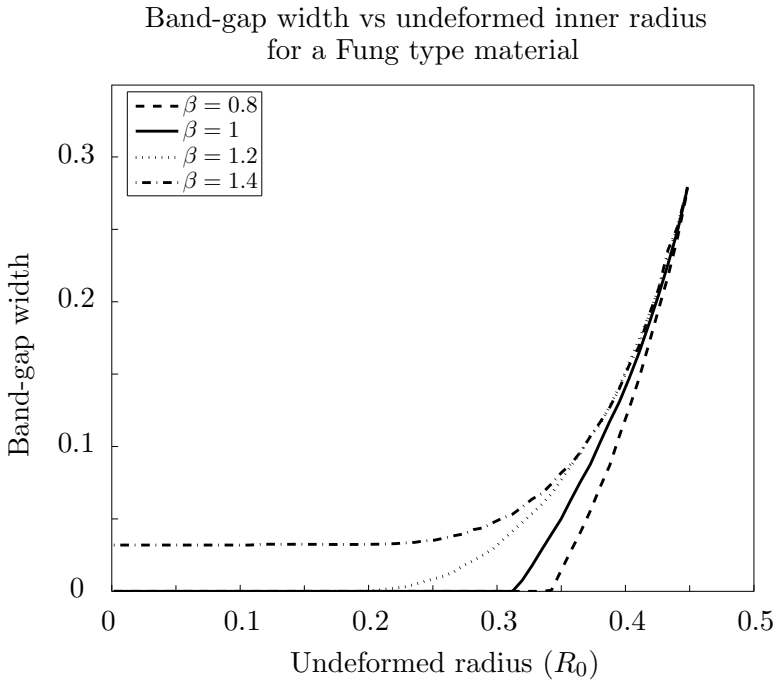

Figure 5.14: The band gap widths vs the undeformed inner radius for a Fung material.

The strain energy functions studied were neo-Hookean, Mooney-Rivlin and a specific form of Fung model. The Mooney-Rivlin material caused almost no change in the shape of the band structure but did alter the existence of a band gap. The effect on the band gap width is felt most at smaller initial radii. The Fung strain energy function has a big effect on the shape of the band diagram but does not appear to significantly change the existence or otherwise of a stop band.

In the next chapter we look at a compressible elastic material. This has the advantage of allowing longitudinal waves so the compressional and in-plane shear wave modes can be studied. At the same time, the initial (static large amplitude) deformation is more challenging to find and only possible analytically for a limited number of strain energy functions. For this reason, the initial nonlinear deformation will be found numerically. By using numerical methods to find the initial deformation, we are unrestricted in both the nature of the deformation and the strain energy function used in this method.

Chapter 6

Tuning phononic crystals using a nonlinear elastic pre-stress - compressible materials

6.1 Introduction

In chapter 5, we discussed the tuning of band diagrams for horizontally polarised shear waves by applying a nonlinear, incompressible pre-stress. In the current chapter we will discuss the related problem but in a compressible material. The presence of a compressible material not only means that we now lose the incompressibility constraint in the initial deformation but also that we are able to investigate the coupled pressure and in-plane shear wave. We remind the reader that we refer to this as the P-SV mode.

Early work looking at the coupled elastic modes was carried out by Sigalas and Economou [81], finding the band diagrams of the full elastic equations using the plane-wave expansion method. Sigalas later followed up on this work [80] and extended it by looking at defect states by changing the radius of one cylinder. Suzuki and Yu [82] found the band diagrams for more complex three-dimensional geometries. More recently Hussein [34] developed an efficient method to find the full elastic band diagrams which was demonstrated using a two-dimensional crystal with square inclusions.

In this chapter we will discuss how we get the incremental equation for a pre-stressed phononic crystal using the small-on-large technique. The band diagrams for

the SH mode are discussed in order to draw comparisons with the previous chapter. Once this is done we will investigate the band diagrams for the coupled P-SV modes.

6.2 Cylinder inflation

We choose to induce the same form of initial deformation as in the background section 2.4.2. Recall that this deformation is described as the inflation of an annular cylinder from initial radius R_0 to final radius r_0 along with an axial stretch β. The outer radius R_1 remains unchanged so $R_1 = r_1$. This deformed cylinder is embedded in a homogeneous stress-free host material as before. Waves are polarised perpendicular to the axis of the cylinders. Since our material is compressible, we allow both pressure (compressional) and shear waves, with mode conversion occurring at boundaries.

When considering compressible materials, we have additional freedom in choosing a strain energy function since $I_3 \neq 1$. It is known that there are six classes of strain energy functions for which we can find the deformation field analytically [20]. The issue with these classes is that they are not always physically realistic. We choose to use a more realistic strain energy function, for which the deformation must unfortunately be found numerically.

We shall illustrate the method with the strain energy function presented by Levinson and Burgess [49]

$$W = \frac{\mu}{2}(I_1 - 3) + \frac{\lambda + \mu}{2}(I_3 - 1) - (\lambda + 2\mu)(I_3^{1/2} - 1). \tag{6.1}$$

This strain energy function was chosen as it is a compressible extension to the neo-Hookean strain energy function. We first find the deformation (R(r)) numerically and then proceed with finding the equation governing the incremental waves. The plane-wave expansion method is then used on the incremental equation to find the band diagram. It is worth noting that this method can work for any choice of strain energy function.

We recall from the background section 2.4.2 that in cylindrical polar coordinates the deformation gradient tensor is given by the principal stretches

$$\mathbf{F} = \begin{pmatrix} \lambda_1 & 0 & 0 \\ 0 & \lambda_2 & 0 \\ 0 & 0 & \lambda_3 \end{pmatrix}, \tag{6.2}$$

$$\lambda_1 = \lambda_r = \frac{1}{R'(r)}, \quad \lambda_2 = \lambda_\theta = \frac{r}{R}, \quad \lambda_3 = \lambda_z = \beta. \tag{6.3}$$

The subscripts r, θ and z are there to remind the reader that the three principal directions align with the radial, azimuthal and axial directions. As before, we seek the function $R(r)$ which describes the deformation.

In order to find the initial deformation, we use the static equation of equilibrium defined by (2.158) as

$$\operatorname{div}(\mathbf{T}) = \mathbf{0}, \tag{6.4}$$

where $\mathbf{T}$ is the Cauchy stress tensor. Written in full, this gives the three equations

$$\frac{\partial T_{rr}}{\partial r} + \frac{1}{r}\left(\frac{\partial T_{\theta r}}{\partial \theta} + T_{rr} - T_{\theta\theta}\right) + \frac{\partial T_{zr}}{\partial z} = 0, \tag{6.5}$$

$$\frac{\partial T_{r\theta}}{\partial r} + \frac{1}{r}\left(\frac{\partial T_{\theta\theta}}{\partial \theta} + T_{r\theta} + T_{\theta r}\right) + \frac{\partial T_{z\theta}}{\partial z} = 0, \tag{6.6}$$

$$\frac{\partial T_{rz}}{\partial r} + \frac{1}{r}\left(\frac{\partial T_{\theta z}}{\partial \theta} + T_{rz}\right) + \frac{\partial T_{zz}}{\partial z} = 0, \tag{6.7}$$

where T_{ij} are the components of the Cauchy stress tensor. By the nature of our deformation, we have no shear (eliminating all T_{ij} terms when $i \neq j$) and we have no variation with θ and z (eliminating all derivatives with respect to these variables). The remaining non-zero component of $\operatorname{div}(\mathbf{T})$ gives

$$\frac{\partial T_{rr}}{\partial r} + \frac{1}{r}\left(T_{rr} - T_{\theta\theta}\right) = 0, \tag{6.8}$$

where the Cauchy stress components are given by (2.152)

$$T_{rr} = \frac{\lambda_r}{J}\frac{\partial W}{\partial \lambda_r}, \quad T_{\theta\theta} = \frac{\lambda_\theta}{J}\frac{\partial W}{\partial \lambda_\theta}. \tag{6.9}$$

Substituting the Levinson and Burgess strain energy function and the principal stretches into equation (6.8), we obtain an ordinary differential equation for $R(r)$

$$\begin{aligned}\frac{d^2R}{dr^2} &= \frac{\mu R(R')^2 + (\lambda+\mu)r\beta^2R' - \frac{(\lambda+\mu)r^2\beta^2(R')^2}{R} - \mu r(R')^3}{\mu R^2 + (\lambda+\mu)r^2\beta^2} \\ &= \frac{\left(\mu R^2 + \frac{R(\lambda+\mu)r^2\beta^2)}{R'}\right)\left(\frac{(R')^2}{R} - \frac{r(R')^3}{R^2}\right)}{\mu R^2 + (\lambda+\mu)r^2\beta^2}.\end{aligned} \tag{6.10}$$

This differential equation is accompanied by the boundary conditions that the undeformed inner and outer radii correspond to the deformed, that is

$$R(r_0) = R_0, \quad R(r_1) = R_1 = r_1. \tag{6.11}$$

Because the material considered is compressible, the inner radius is no longer defined by the axial stretch and fixed outer radius. The deformation will now be characterised not only by the axial stretch, but also by the volume change given by

$$\Delta V = \frac{V_f}{V_i} = \frac{\beta(r_1^2 - r_0^2)}{R_1^2 - R_0^2}, \tag{6.12}$$

where V_i and V_f are the initial and final volumes of the annular section. The deformed inner radius is therefore given by

$$r_0 = \sqrt{R_1^2 - \frac{\Delta V}{\beta}(R_1^2 - R_0^2)}. \tag{6.13}$$

For each example, we apply the necessary radial pressure on the inner and outer surface, and radial stretch, to maintain the chosen deformation. We choose the annular region to be significantly more compliant than the host region and assume that the host material remains stress-free.

To solve the second order ODE given by equation (6.10) we first convert it into a set of two coupled first order ordinary differential equations by defining

$$y_1(r) = R(r), \tag{6.14}$$

$$y_2(r) = R'(r). \tag{6.15}$$

In this case, the two ODEs become

$$\frac{dy_1}{dr} = y_2, \tag{6.16}$$

$$\frac{dy_2}{dr} = \frac{\left(\mu y_1^2 + \frac{y_1(\lambda+\mu)r^2\beta^2)}{y_2}\right)\left(\frac{(y_2)^2}{y_1} - \frac{r(y_2)^3}{y_1^2}\right)}{\mu y_1^2 + (\lambda+\mu)r^2\beta^2}. \tag{6.17}$$

This equation is solved to find $R(r)$ using the MATLAB function `bvp4c`. To ensure that the deformation is correct we compare the solution of the ODE to the incompressible case in figure 6.2. As observed, the solution exhibits the expected behaviour, and approaches the neo-Hookean case in the incompressible limit.

6.2.1 Incremental waves

We now proceed to find the governing equation for the incremental waves superposed on this initial finite deformation. We will use the method of small-on-large as discussed in the background section 2.4.4. We consider waves that are polarised in the r-θ plane.

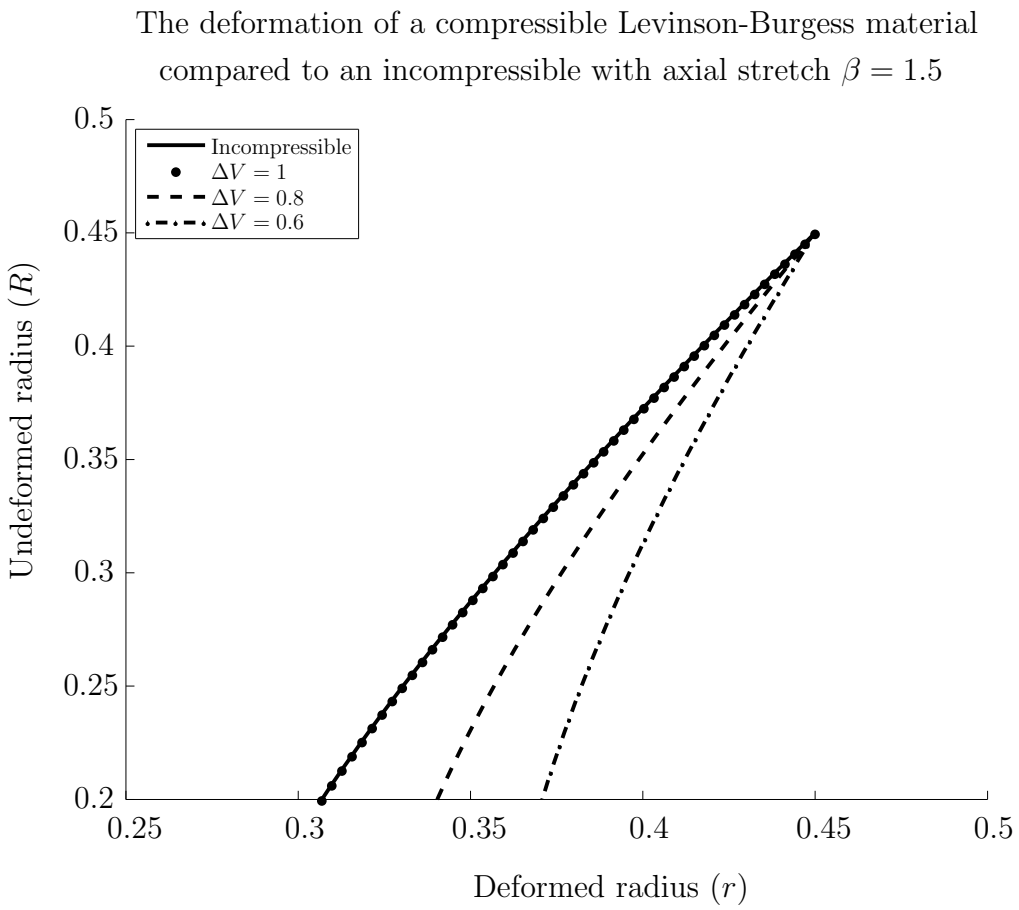

Figure 6.1: The deformation of a Levinson-Burgess material compared to the incompressible deformation given by equation (5.1). The initial inner radius is $R_0 = 0.2$, the outer radius is $R_1 = 0.45$ and the axial stretch is $\beta = 1.5$. Different volumetric changes are shown for the compressible material.

Since there is no z dependence in the deformation, we do not expect the waves to vary in the z direction. In this case, the incremental displacement from the deformed configuration is given by

$$\mathbf{u} = \Big(u_r(r,\theta),\, u_\theta(r,\theta),\, 0\Big). \tag{6.18}$$

A harmonic time dependence is assumed, so the time-dependent displacement is $\mathbf{u}\, e^{-i\omega t}$.

Recall from the discussion of the small-on-large theory that the equation of motion is given by (2.187)

$$\mathrm{div}\boldsymbol{\zeta} = -\rho\,\omega^2\mathbf{u}, \tag{6.19}$$

where $\boldsymbol{\zeta}$ is the push forward of the incremental nominal stress and is given by

$$\boldsymbol{\zeta} = \mathbf{M} : \boldsymbol{\gamma}, \tag{6.20}$$

in which

$$\boldsymbol{\gamma} = \operatorname{grad} \mathbf{u} = \begin{pmatrix} \dfrac{\partial u_r}{\partial r} & \dfrac{1}{r}\left(\dfrac{\partial u_r}{\partial \theta} - u_\theta\right) & 0 \\ \dfrac{\partial u_\theta}{\partial r} & \dfrac{1}{r}\left(\dfrac{\partial u_\theta}{\partial \theta} + u_r\right) & 0 \\ 0 & 0 & 0 \end{pmatrix} \tag{6.21}$$

and

$$M_{ijkl} = J^{-1} \frac{\partial^2 W}{\partial F_{jm} \partial F_{ln}} F_{im} F_{kn}. \tag{6.22}$$

It can be shown that (see [13])

$$M_{iijj} = \frac{\lambda_i \lambda_j}{J} \frac{\partial^2 W}{\partial \lambda_i \partial \lambda_j}, \tag{6.23}$$

with no sum over repeated indices. Provided that $i \neq j$ and $\lambda_i \neq \lambda_j$ we also have

$$M_{ijij} = \frac{\lambda_i^2}{J(\lambda_i^2 - \lambda_j^2)} \left(\lambda_i \frac{\partial W}{\partial \lambda_i} - \lambda_j \frac{\partial W}{\partial \lambda_j} \right), \tag{6.24}$$

$$M_{ijji} = \frac{\lambda_i \lambda_j}{J(\lambda_i^2 - \lambda_j^2)} \left(\lambda_j \frac{\partial W}{\partial \lambda_i} - \lambda_i \frac{\partial W}{\partial \lambda_j} \right). \tag{6.25}$$

All other combinations give $M_{ijkl} = 0$.

We now have the tools to find the elements of $\boldsymbol{\zeta}$. As it turns out, there are only five non-zero elements. These are

$$\begin{aligned} \zeta_{11} &= M_{1111}\gamma_{11} + M_{1122}\gamma_{22}, \\ \zeta_{12} &= M_{1212}\gamma_{21} + M_{1221}\gamma_{12}, \\ \zeta_{21} &= M_{2121}\gamma_{12} + M_{2112}\gamma_{21}, \\ \zeta_{22} &= M_{2211}\gamma_{11} + M_{2222}\gamma_{22}, \\ \zeta_{33} &= M_{3311}\gamma_{11} + M_{3322}\gamma_{22}. \end{aligned} \tag{6.26}$$

With this in mind, taking div$\boldsymbol{\zeta}$ gives

$$\operatorname{div}\boldsymbol{\zeta} = \begin{pmatrix} \dfrac{\partial \zeta_{11}}{\partial r} + \dfrac{1}{r}\left(\dfrac{\partial \zeta_{21}}{\partial \theta} + \zeta_{11} - \zeta_{22}\right) \\ \dfrac{\partial \zeta_{12}}{\partial r} + \dfrac{1}{r}\left(\dfrac{\partial \zeta_{22}}{\partial \theta} + \zeta_{12} + \zeta_{21}\right) \\ \dfrac{\partial \zeta_{33}}{\partial z} \end{pmatrix}. \tag{6.27}$$

Since we impose no variation in z, the last element becomes zero. All that remains is to express $\boldsymbol{\zeta}$ in terms of the principal stretches and substitute this into the equation of motion (6.19).

Substituting the expressions for ζ_{ij} from (6.26) into the divergence gives the r and θ components of the equation of motion

$$\begin{aligned}&\frac{\partial}{\partial r}\left(M_{1111}\frac{\partial u_r}{\partial r}+M_{1122}\frac{1}{r}\left(\frac{\partial u_\theta}{\partial\theta}+u_r\right)\right)\\&\quad+\frac{1}{r}\left[\frac{\partial}{\partial\theta}\left(M_{2121}\frac{1}{r}\left(\frac{\partial u_r}{\partial\theta}-u_\theta\right)+M_{2112}\frac{\partial u_\theta}{\partial r}\right)\right.\\&\quad\left.+(M_{1111}-M_{2211})\frac{\partial u_r}{\partial r}+(M_{1122}-M_{2222})\frac{1}{r}\left(\frac{\partial u_\theta}{\partial\theta}+u_r\right)\right]+\rho\,\omega^2u_r=0,\end{aligned}\tag{6.28}$$

$$\begin{aligned}&\frac{\partial}{\partial r}\left(M_{1212}\frac{\partial u_\theta}{\partial r}+M_{1221}\frac{1}{r}\left(\frac{\partial u_r}{\partial\theta}-u_\theta\right)\right)\\&\quad+\frac{1}{r}\left[\frac{\partial}{\partial\theta}\left(M_{2211}\frac{\partial u_r}{\partial r}+M_{2222}\frac{1}{r}\left(\frac{\partial u_\theta}{\partial\theta}+u_r\right)\right)\right.\\&\quad\left.+(M_{1212}+M_{2112})\frac{\partial u_\theta}{\partial r}+(M_{2121}+M_{1221})\frac{1}{r}\left(\frac{\partial u_r}{\partial\theta}-u_\theta\right)\right]+\rho\,\omega^2u_\theta=0,\end{aligned}\tag{6.29}$$

where M_{ijkl} are given by

$$M_{1111}=\frac{\mu\lambda_1}{\lambda_2\lambda_3}+(\lambda+\mu)\lambda_1\lambda_2\lambda_3,\quad M_{2222}=\frac{\mu\lambda_2}{\lambda_1\lambda_3}+(\lambda+\mu)\lambda_1\lambda_2\lambda_3,$$

$$M_{1212}=\frac{\mu\lambda_1}{\lambda_2\lambda_3},\quad M_{2121}=\frac{\mu\lambda_2}{\lambda_1\lambda_3},\tag{6.30}$$

$$M_{1122}=M_{2211}=2(\lambda+\mu)\lambda_1\lambda_2\lambda_3-(\lambda+2\mu),$$

$$M_{1221}=M_{2112}=(\lambda+2\mu)-(\lambda+\mu)\lambda_1\lambda_2\lambda_3.\tag{6.31}$$

6.2.2 Conversion to Cartesian coordinates

As before in section 5.2.2, we must convert equations (6.28) and (6.29) into Cartesian coordinates since these are the coordinates in which the system is periodic. This is done by multiplying both equations by r^2 and changing the derivatives according to

$$r\frac{\partial}{\partial r}=x\frac{\partial}{\partial x}+y\frac{\partial}{\partial y},\tag{6.32}$$

$$\frac{\partial}{\partial\theta}=-y\frac{\partial}{\partial x}+x\frac{\partial}{\partial y}.\tag{6.33}$$

In doing this, we obtain the equations

$$\begin{aligned}&M_1\frac{\partial^2u_r}{\partial x^2}+M_2\frac{\partial^2u_r}{\partial x\partial y}+M_3\frac{\partial^2u_r}{\partial y^2}+M_4\frac{\partial u_r}{\partial x}+M_5\frac{\partial u_r}{\partial y}\\&+N_1\frac{\partial^2u_\theta}{\partial x\partial y}+N_2\frac{\partial u_\theta}{\partial x}+N_3\frac{\partial u_\theta}{\partial y}+\rho\omega^2u_r=0,\end{aligned}\tag{6.34}$$

$$O_1\frac{\partial^2 u_r}{\partial x\partial y}+O_2\frac{\partial u_r}{\partial x}+O_3\frac{\partial u_r}{\partial y}$$
$$+P_1\frac{\partial^2 u_\theta}{\partial x^2}+P_2\frac{\partial^2 u_\theta}{\partial x\partial y}+P_3\frac{\partial^2 u_\theta}{\partial y^2}+P_4\frac{\partial u_\theta}{\partial x}+P_5\frac{\partial u_\theta}{\partial y}+\rho\omega^2 u_\theta=0, \tag{6.35}$$

where $M_1, M_2 \ldots, P_5$ are given by

$$M_1 = x^2M_{1111}+y^2M_{2222}, \qquad M_2 = 2xy(M_{1212}-M_{2121}),$$
$$M_3 = x^2M_{2121}+y^2M_{1212}, \qquad M_4 = x\left(r\frac{\partial M_{1111}}{\partial r}+M_{1212}-M_{2121}\right),$$
$$M_5 = y\left(r\frac{\partial M_{1212}}{\partial r}+M_{1212}-M_{2121}\right), \qquad N_1 = (x^2+y^2)(M_{1122}+M_{1221}),$$
$$N_2 = y\left(r\frac{\partial M_{1221}}{\partial r}\right), \qquad N_3 = x\left(r\frac{\partial M_{1122}}{\partial r}\right),$$
$$O_1 = (x^2+y^2)(M_{1122}+M_{1221}), \qquad O_2 = y\left(r\frac{\partial M_{1122}}{\partial r}\right),$$
$$O_3 = x\left(r\frac{\partial M_{1221}}{\partial r}\right), \qquad P_1 = x^2M_{1212}+y^2M_{2121},$$
$$P_2 = 2xy(M_{1212}-M_{2121}), \qquad P_3 = x^2M_{2222}+y^2M_{1111},$$
$$P_4 = x\left(r\frac{\partial M_{1212}}{\partial r}+M_{1212}-M_{2121}\right), \qquad P_5 = y\left(r\frac{\partial M_{1111}}{\partial r}+M_{1212}-M_{2121}\right).$$

6.3 Implementation of the plane-wave expansion

The implementation of the plane-wave expansion method is carried out in much the same way as described in the background section 2.3.3. The main difference now is that we have a pair of coupled equations governing the shear and pressure waves. We begin by writing the displacements in the form

$$u_r(\mathbf{x}) = e^{i\mathbf{K}\cdot\mathbf{x}}\sum_{\mathbf{G}} u_{r\mathbf{G}}\, e^{i\mathbf{G}\cdot\mathbf{x}}, \qquad u_\theta(\mathbf{x}) = e^{i\mathbf{K}\cdot\mathbf{x}}\sum_{\mathbf{G}} u_{\theta\mathbf{G}}\, e^{i\mathbf{G}\cdot\mathbf{x}}, \tag{6.36}$$

with derivatives of these functions simply bringing down a factor of $i(K_i+G_i)$, for example

$$\frac{\partial u_r}{\partial x} = ie^{i\mathbf{K}\cdot\mathbf{x}}\sum_{\mathbf{G}} u_{r\mathbf{G}}(K_x+G_x)\, e^{i\mathbf{G}\cdot\mathbf{x}}, \tag{6.37}$$

$$\frac{\partial^2 u_\theta}{\partial x\partial y} = ie^{i\mathbf{K}\cdot\mathbf{x}}\sum_{\mathbf{G}} u_{\theta\mathbf{G}}(K_x+G_x)(K_y+G_y)\, e^{i\mathbf{G}\cdot\mathbf{x}}. \tag{6.38}$$

The functions $M_1, M_2 \ldots, P_5$ are all written as Fourier series, for example

$$M_1(\mathbf{x}) = \sum_{\mathbf{G}} M_{1\mathbf{G}}\, e^{i\mathbf{G}\cdot\mathbf{x}}, \tag{6.39}$$

with the Fourier coefficient being given by

$$M_{1\mathbf{G}} = \frac{1}{A}\int_{Cell} M_1(\mathbf{X})e^{-i\mathbf{G}\cdot\mathbf{x}}d\mathbf{X}. \tag{6.40}$$

By applying the same technique outlined in section 2.3.3, we find the coupled equations in matrix form

$$\begin{aligned}
&\sum_{\mathbf{G}}\Big(\big[M_{1\mathbf{H}}(K_x+G_x)^2 + M_{2\mathbf{H}}(K_x+G_x)(K_y+G_y) + M_{3\mathbf{H}}(K_y+G_y)^2 \\
&\quad - iM_{4\mathbf{H}}(K_x+G_x) - iM_{5\mathbf{H}}(K_y+G_y) - \rho_{\mathbf{H}}\omega^2\big]u_{r\mathbf{G}} \\
&\quad + \big[N_{1\mathbf{H}}(K_x+G_x)(K_y+G_y) - iN_{2\mathbf{H}}(K_x+G_x) - iN_{3\mathbf{H}}(K_y+G_y)\big]u_{\theta\mathbf{G}}\Big) = 0, \\
&\sum_{\mathbf{G}}\Big(\big[O_{1\mathbf{H}}(K_x+G_x)(K_y+G_y) - iO_{2\mathbf{H}}(K_x+G_x) - iO_{3\mathbf{H}}(K_y+G_y)\big]u_{r\mathbf{G}} \\
&\quad + \big[P_{1\mathbf{H}}(K_x+G_x)^2 + P_{2\mathbf{H}}(K_x+G_x)(K_y+G_y) + P_{3\mathbf{H}}(K_y+G_y)^2 \\
&\quad - iP_{4\mathbf{H}}(K_x+G_x) - iP_{5\mathbf{H}}(K_y+G_y) - \rho_{\mathbf{H}}\omega^2\big]u_{\theta\mathbf{G}}\Big) = 0,
\end{aligned}$$

where

$$\mathbf{H} = \mathbf{G}' - \mathbf{G} \tag{6.41}$$

for all $\mathbf{G}'$. This system of equations is written in matrix form as

$$\mathbf{A}\mathbf{u}_{\mathbf{G}} = \omega^2\mathbf{B}\mathbf{u}_{\mathbf{G}}, \tag{6.42}$$

where the vector $\mathbf{u}$ incorporates both the radial and azimuthal displacements. When truncating the system at $N_{\max}$, the vector $\mathbf{u}_{\mathbf{G}}$ has the form

$$\mathbf{u}_{\mathbf{G}} = \begin{pmatrix} u_{r(-N_{\max})} \\ u_{r(-N_{\max}+1)} \\ \vdots \\ u_{r(N_{\max})} \\ u_{\theta(-N_{\max})} \\ \vdots \\ u_{\theta(N_{\max})} \end{pmatrix}. \tag{6.43}$$

The matrix $\mathbf{A}$ includes the functions $M_{1\mathbf{H}}, M_{2\mathbf{H}}, \ldots, P_{5\mathbf{H}}$ and is ordered in the following form

$$\mathbf{A} = \begin{pmatrix} M & N \\ O & P \end{pmatrix}, \tag{6.44}$$

and the matrix $\mathbf{B}$ holds only the density information

$$\mathbf{B} = \begin{pmatrix} \rho_{\mathbf{H}} & 0 \\ 0 & \rho_{\mathbf{H}} \end{pmatrix}, \tag{6.45}$$

where ρ_H is the $(2N_{\max}+1) \times (2N_{\max}+1)$ matrix of density coefficients. This matrix eigenvalue problem is solved using the MATLAB `eig` function.

6.4 Results

Here we will present some results for the compressible pre-stress. We first consider the SH mode in the compressible case in order to compare to the previous chapter. In doing this we may investigate the effect that the compressible material has when compared to that with the neo-Hookean strain energy function. After that, we take a look at the P-SV mode in order to study band-gaps of the coupled mode case.

6.4.1 SH mode

In the incompressible limit ($I_3 \to 1$), the Levinson-Burgess strain energy function reduces to the neo-Hookean. For this reason, we begin by looking at the SH mode to see how the compressibility affects the band structure. We have done this by using equations (5.3)-(5.5) with the Levinson-Burgess strain energy function and deformation given by the solution of (6.10).

In figure 6.2 we have plotted the first three modes for the incompressible neo-Hookean material alongside the compressible Levinson-Burgess material. In both cases we apply an axial stretch $\beta = 1.2$. For the compressible material the Poisson ratio is $\nu = 0.25$ and we impose a volume change $\Delta V = 0.8$. It is clear from this band diagram that the compressibility of the Levinson-Burgess strain energy function opens up a stop band that does not exist in the neo-Hookean case.

In figure 6.3 we plot the band-gap width verses inner radius for a given stretch ($\beta = 1.2$) and a number of different volume changes. We show the incompressible case ($\Delta V = 1$) for comparison with the compressible material. In the compressible case, the Poisson ratio is chosen to be $\nu = 0.25$.

We can see from figure 6.3(a) that the ability for the material to compress has a

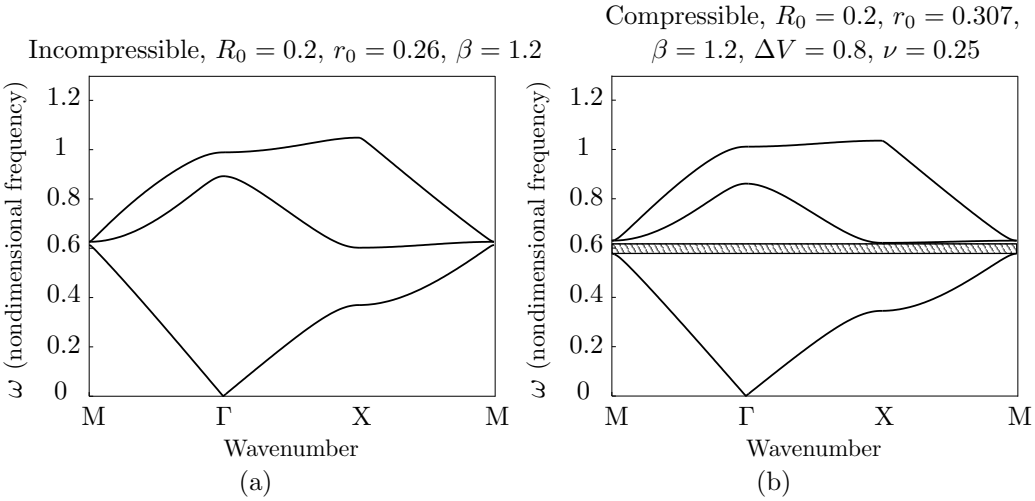

Figure 6.2: The first three SH modes for an initial radius of $R_0 = 0.2$ and axial stretch $\beta = 1.2$. Figure (a) shows the results for an incompressible neo-Hookean material and (b) shows the results for a compressible Levinson-Burgess material with volume change $\Delta V = 0.8$. A stop band is indicated by the shaded region.

significant effect on the width of the band-gap. A decrease in volume always corresponds to an increase in the band-gap width. This is to be expected because, as the volume decreases the inner radius must increase. The effect is felt most significantly for smaller radii.

By considering the deformed radius in figure 6.3(b), we can see that the compressibility has a much less significant effect relative to the final radius. In fact, for some values of the deformed radius, the compressibility actually decreases the band-gap width.

6.4.2 P-SV mode

We now look at the mixed pressure and in-plane shear wave mode where the displacements are perpendicular to the axes of the cylinder and in the same plane as the propagation direction. In this case, the coupled governing equations are given by (6.34) and (6.35).

In figure 6.4 we see the effect on the band diagram of applying a pre-stress corresponding to $\beta = 1.2$ and volume change $\Delta V = 0.8$. A significant change in the band diagram is observed including the appearance of an absolute band-gap for the coupled mode. In addition to this, all of the bands appear to be moved down to lower

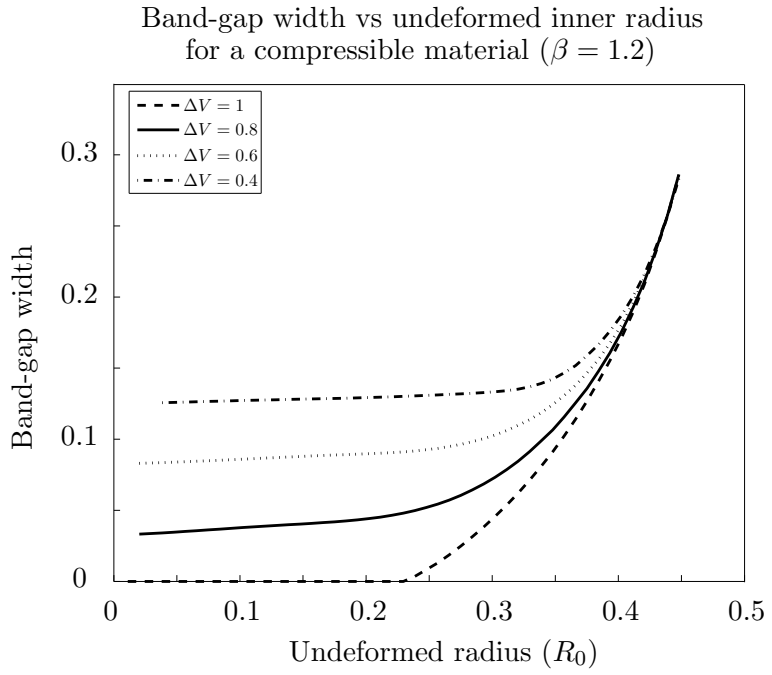

(a)

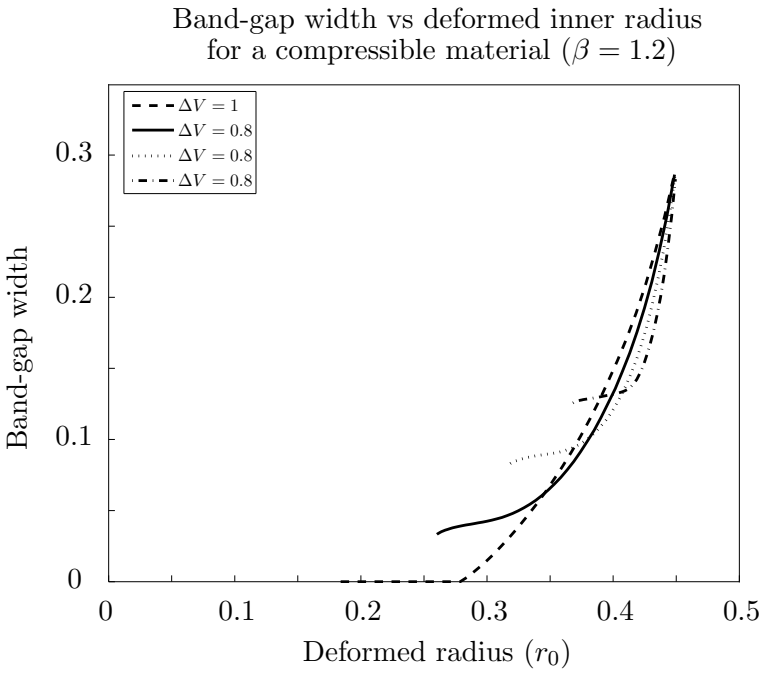

(b)

Figure 6.3: The band-gap width for the deformed configuration with axial stretch $\beta = 1.2$ for the SH mode in a compressible Levinson-Burgess material. Different amounts of volume change are shown and the incompressible Neo-Hookean ($\Delta V = 1$) is given for comparison. In figure (a) the width is plotted against the undeformed radius and in figure (b) the width is plotted against the deformed radius.

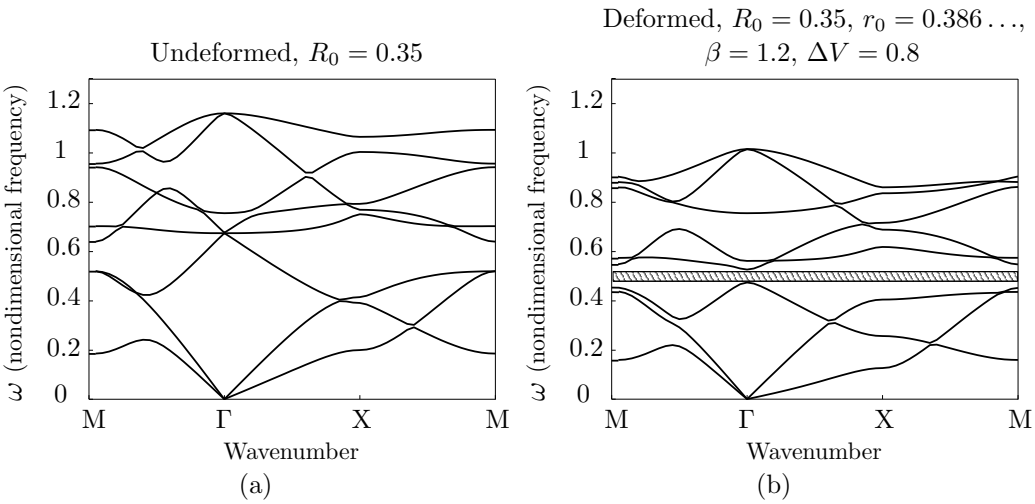

Figure 6.4: The first eight P-SV modes for an initial radius of $R_0 = 0.35$. Figure (a) shows the stress-free material and (b) shows the compressible Levinson-Burgess material with axial stretch $\beta = 1.2$, volume change $\Delta V = 0.8$ and deformed radius $r_0 = 0.386\ldots$. A stop band is shown by the shaded region.

frequencies. It is interesting to note that the wave speed of the lowest mode is heavily reduced.

In figure 6.5 we plot the width of the band-gap against the undeformed radius. The stress-free case is given along with the pre-stressed case with $\beta = 1.2$ and volume change $\Delta V = 0.8$. Clearly the two configurations give very different results. In the stress-free case a stop band switches on around $R_0 = 0.36$ and its width steadily increases as the radius increases. For the pre-stressed case, the stop band switches on earlier and begins to increase but then shortly afterwards drops off and the stop band switches off again. As expected, both stress-free and pre-stressed cases tend to the same band-gap width as $R_0 \to R_1 = 0.45$.

The results given for the P-SV mode are in preliminary stages. Although the method outlined here is complete, there is more work to be done on the precise deformation induced and further investigation of the validity of these results.

6.5 Conclusion

In this chapter we have investigated a pre-stressed phononic crystal made from a compressible elastic material. The incremental equation of motion for the coupled P-SV mode was derived using the small-on-large technique. For the SH mode, the

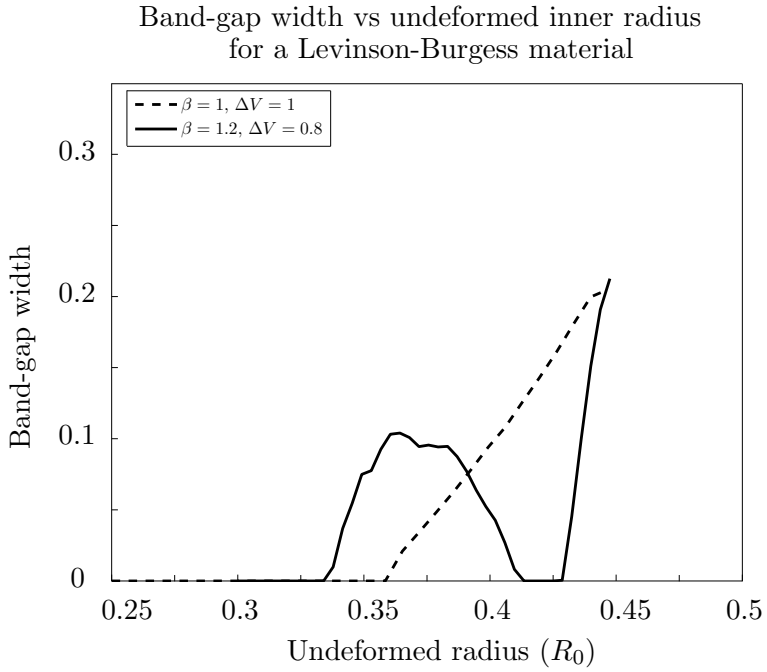

Figure 6.5: The band-gap width for the deformed configuration with axial stretch $\beta = 1.2$ for the P-SV mode in a compressible Levinson-Burgess material. The deformed configuration with volume change $\Delta V = 0.8$ (solid line) is compared to the stress-free case (dashed line).

effect of compressibility was compared to the neo-Hookean case. Preliminary results were obtained for the coupled P-SV mode.

For the horizontally polarised shear mode, we have compared the compressible Levinson-Burgess strain energy function with the neo-Hookean, showing that the compressibility further increases the width of the band-gap and decreases the onset radius. It was shown that the compressibility has a relatively small effect when considering the deformed radius. This implies that the widening of the band-gap is caused more by the increase of the deformed radius than the change in deformation itself. More work needs to be done to test this hypothesis fully.

For the coupled pressure and shear mode we have shown that pre-stress can switch on a stop band. In investigating the width of the band-gap, it is found that the pre-stressed P-SV mode behaves differently from the SH mode. Although the stop band switches on earlier than in the stress-free case, in the pre-stressed material the band-gap width drops off shortly afterwards, switching the band-gap off for higher radii.

There is a large scope for future work influenced by the examples given here. Firstly,

it would be interesting to see if it is possible to obtain a stop band in both the SH and P-SV mode for the same deformation. Similarly, it would be interesting to find out if it is possible to get a stop band in the pressure mode but allow the same frequencies to propagate in the shear mode. In doing this, by building a finite specimen it may be possible to take pressure waves in a fluid and convert them into shear waves in a solid thus making efficient soundproofing at specific frequencies.

The work presented here lays out the groundwork for the construction and testing of phononic crystal devices. The next step is to carry out a study into which specific materials and deformations are most convenient for production. One additional initial deformation under consideration is a twist of each unit cell.

Chapter 7

Conclusion

The main aim of this thesis has been to study the behaviour of waves in heterogeneous materials. Focus has been given to the stop and pass band properties of periodic structures. In particular, we have studied how wave envelopes of particular frequencies interact with stop bands and investigated the possibility of band-gap tuning through the application of a nonlinear elastic pre-stress.

The transient behaviour of waves was studied by considering a one-dimensional string with point masses (beads). This geometry allows for the exact derivation of the reflection of a prescribed incoming pulse. The exact reflection coefficient was compared to the homogenised result. For the transient forcing of an infinite string with periodically spaced beads, the exact solution was derived in integral form. Both the exact finite time and asymptotic long-time behaviour of this system were studied. New results regarding the energy input into the system in stop and pass bands are presented.

For studying the effect of nonlinear elastic pre-stress on the band-gap properties of small amplitude elastic waves we used a two-dimensional periodic lattice. Pre-stress was applied to an annular region of nonlinear material that was inserted into a stress-free host region. Band diagrams were found for this novel material and the possibility of band-gap tuning was demonstrated.

7.1 Summary of results

In chapter 3 we studied the reflection of a pulse from an infinite set of periodically spaced beads. The reflected pulse was given in terms of an inverse Fourier transform, dependent on the (frequency dependent) reflection coefficient of a time-harmonic wave. An effective reflection coefficient was obtained by using the dispersion relation for an infinite string, and an exact reflection coefficient was derived using the Wiener-Hopf technique. Using the exact reflection coefficient, the pulse solution was given at any time by evaluation of the residue contributions from a finite series of poles.

We drew comparisons between the exact and effective reflection coefficients. Despite being constructed using the exact wavenumber for a periodic beaded string, the effective reflection coefficient was found to be valid only in the very low frequency regime. This has implications on the conclusions drawn from finding effective properties of an infinite material. Knowledge of the effective wavenumber does not give us the complete story and more must be done to find out how pulses are reflected from a finite or semi-infinite periodic structure.

To investigate in more depth how waves are excited in periodic structures, chapter 4 focused on an infinite string with beads spaced periodically along the entire length. This inhomogeneous string is initially at rest. A prescribed force, switched on at a specified time, was applied to the bead at the origin. The exact solution was found in integral form by using both Fourier and z transforms. This solution was analysed by converting the infinite number of branch points into a sum of poles. Using Cauchy's residue theorem, the residues at these poles were determined to give the value of the integral. In so doing, we were able to obtain an exact solution at any finite point in time by summing the residues of a finite number of poles. This gives a clear picture of how waves of different frequencies enter the system. As expected we get travelling waves forming in the pass bands and evanescent modes forming in stop bands.

We investigated how the solution reached a steady-state by taking a long-time approximation of the integral solution. It was found that the bead displacements remain bounded in all cases except on the lower edge of the stop band where the displacements grow slowly with time ($O(t^{1/2})$). This fact led to the discovery that the system behaves differently on the lower and upper edges of the stop band. This was

not expected and there is still no clear explanation as to why this is so.

In order to understand how the solution remains bounded in a stop band despite the fact that energy is not propagated away by travelling waves, we calculated the work done on the bead at the origin. As expected, when forcing in a pass band, a finite amount of work done was done per cycle. The amount of energy input corresponds to the energy transported out to infinity by the travelling waves. When forcing in a stop band, it was found that in the long-time limit no energy is input per forcing cycle. This implies that the energy put into the system exactly balances the energy given back by the system.

The effect of a nonlinear pre-stress on the stop band structure of a two-dimensional phononic crystal was investigated in chapters 5 and 6. In chapter 5 we restricted our study to incompressible materials and horizontally polarised shear waves. The strain energy functions studied were the neo-Hookean, Mooney-Rivlin and Fung.

For all three strain energy functions it was shown how it is possible to switch on and off band-gaps by applying either an inflation or deflation of the cylinder. The widths of the band-gap for different radii and amounts of pre-stress were investigated. The effect of the pre-stress on the width of the band-gap was found to be most significant in the neo-Hookean solid, with the presence of the I_2 invariant in the Mooney-Rivlin material diminishing the effect. The Fung material induced a significant change in the shape of the band diagram and the frequency at which the stop band appeared.

In chapter 6 the study of pre-stressed elastic composites was extended to the case of compressible materials. The strain energy function used was a compressible extension of the neo-Hookean material that was suggested by Levinson and Burgess. The small-on-large technique was used to derive the incremental equations for the coupled pressure and shear modes.

The antiplane shear mode in the compressible material was compared to the neo-Hookean case. It was shown that the compressibility increased the width of the stop band but had little effect on the shape of the band diagram. In the compressible case, the deformed material has almost the same stop band width as the incompressible material with equivalent deformed radius. Band-gap switching was also shown for the coupled P-SV modes and preliminary results for the band-gap width were presented.

7.2 Future work

There is much future work to be done surrounding the problems discussed here. In particular surrounding transient waves in heterogeneous media and reflection from complex materials. In order to truly understand how periodic materials behave in the real world we need to move away from the infinite, time-harmonic systems and move towards the finite geometry transient problems.

For the reflection problem it is still not clear if it is possible to find a reasonable effective reflection coefficient for general periodic structures. An approximate form of the reflection coefficient is highly desirable in order to be able to find the reflected pulses to reasonable accuracy.

The work from this thesis can be extended to ask other questions that still remain. Firstly, how does the long-time approximate solution for the reflected pulse behave? Can we construct a reflection coefficient for a periodic string with changing density, representing a layered medium (rather than a pointwise discontinuous system)? By using similar analysis in two dimensions, is it possible to find the exact reflection coefficient and determine the propagation and reflection of pulse along a membrane with point masses periodically spaced on a half plane?

An area of interest in both the reflection problem and the forcing of a semi-infinite bead is the propagation of finite pulses of different forms. It would be interesting to find out what happens to finite sinusoidal pulses and chirps that exhibit a large range of frequencies.

In the area of phononic crystals there is still a lot of work to be done in investigating the tuning effects of nonlinear elastic pre-stress. For example, how do different deformations affect the band-gap structure? Which of these deformations is most realistically achievable in the real world?

A key goal to achieve in order to move towards practical applications of tunable band-gap materials is to build and experiment on real samples. Before this is achievable, a substantial feasibility study must be carried out to find which materials are best suited and which deformation is most ideal. The tools developed in this thesis lay out the groundwork for this study to take place.

Bibliography

[1] D. Abrahams. *Advanced analytical methods for continuum modelling: Complex variable methods, the Wiener-Hopf technique and one-dimensional dynamic homogenization.* Magical Books for Industry Lecture Series, 2012. (http://oldwww.ma.man.ac.uk/magicalbooks/continuumindex.html).

[2] M. Abramowitz and I. Stegun. *Handbook of Mathematical Functions.* Dover Publications, 1968.

[3] T. Antonakakis, R. V. Craster, and S. Guenneau. Asymptotics for metamaterials and photonic crystals. *Proceedings of the Royal Society A: Mathematical, Physical and Engineering Science*, 469(2152), 2013.

[4] K. Bertoldi and M. C. Boyce. Wave propagation and instabilities in monolithic and periodically structured elastomeric materials undergoing large deformations. *Physical Review B: Condensed Matter and Materials Physics*, 78(18):4107–4122, 2008.

[5] D. Bland. *Wave theory and applications.* Oxford, 1988.

[6] F. Bloch. Über die quantenmechanik der elektronen in kristallgittern. *Zeitschrift für Physik*, 52(7-8):555–600, 1929.

[7] A. F. Bower. *Applied mechanics of solids.* CRC press, 2011.

[8] L. Brillouin. *Wave propagation in periodic structures: Electric filters and crystal lattices.* McGraw-Hill, 1946.

[9] F. Casadei, T. Delpero, A. Bergamini, P. Ermanni, and M. Ruzzene. Piezoelectric resonator arrays for tunable acoustic waveguides and metamaterials. *Journal of Applied Physics*, 112(6):4902–4906, 2012.

[10] C. Coulson and A. Jeffrey. *Waves: A mathematical approach to the common types of wave motion 2nd edition*. Longman, 1977.

[11] R. Craster and S. Guenneau. *Acoustic metamaterials: negative refraction, imaging, lensing and cloaking*. Springer, 2013.

[12] R. V. Craster, T. Antonakakis, M. Makwana, and S. Guenneau. Dangers of using the edges of the Brillouin zone. *Physical Review B: Condensed Matter and Materials Physics*, 86(11):5130–5135, 2012.

[13] M. Destrade and G. Saccomandi. *Waves in nonlinear pre-stressed materials*. New York: Springer, 2007.

[14] P. Deymier. *Acoustic metamaterials and phononic crystals*. Springer, 2013.

[15] A. Evgrafov, C. J. Rupp, M. L. Dunn, and K. Maute. Optimal synthesis of tunable elastic wave-guides. *Computer Methods in Applied Mechanics and Engineering*, 198(2):292–301, 2008.

[16] M. Farhat, S. Enoch, S. Guenneau, and A. B. Movchan. Broadband cylindrical acoustic cloak for linear surface waves in a fluid. *Physical Review Letters*, 101(13):4501–4504, 2008.

[17] R. Feng and K. Liu. Tuning the band-gap of phononic crystals with an initial stress. *Physica B: Condensed Matter*, 407(12):2032–2036, 2012.

[18] G. Floquet. Sur les équations différentielles linéaires à coefficients périodiques. *Annales scientifiques de l'École Normale Supérieure*, 1:181–238, 1883.

[19] J. Fouque, J. Garnier, G. Papanicolaou, and K. Solna. *Wave propagation and time reversal in randomly layered media*. Springer, 2007.

[20] Y. Fu and R. Ogden. *Nonlinear elasticity: Theory and applications*. Cambirdge university press, 2001.

[21] Y. C. Fung. *Biomechanics: Mechanical Properties of Living Tissues*. Springer-Verlag, 1993.

[22] J. Gazalet, S. Dupont, J. Kastelik, Q. Rolland, and B. Djafari-Rouhani. A tutorial survey on waves propagating in periodic media: Electronic, photonic and phononic crystals. perception of the Bloch theorem in both real and fourier domains. *Wave Motion*, 50(3):613–654, 2013.

[23] M. Gei. Wave propagation in quasiperiodic structures: stop/pass band distribution and prestress effects. *International Journal of Solids and Structures*, 47(22):3067–3075, 2010.

[24] M. Gei, A. B. Movchan, and D. Bigoni. Band-gap shift and defect induced annihilation in prestressed elastic structures. *Journal of Applied Physics*, 105(6):3507–3513, 2009.

[25] M. Gei, S. Roccabianca, and M. Bacca. Controlling bandgap in electroactive polymer-based structures. *Mechatronics*, 16(1):102–107, 2011.

[26] C. Goffaux and J. P. Vigneron. Theoretical study of a tunable phononic band gap system. *Physical Review B: Condensed Matter and Materials Physics*, 64(7):5118–5122, 2001.

[27] B. J. Gomez, C. E. Repetto, C. R. Stia, and R. Welti. Oscillations of a string with concentrated masses. *European Journal of Physics*, 28(5):961–975, 2007.

[28] K. Graff. *Wave motion in elastic solids*. Dover, 1975.

[29] A. E. Green and W. Zerna. *Theoretical elasticity*. Dover, New York, 1992.

[30] D. J. Griffiths and C. A. Steinke. Waves in locally periodic media. *American Journal of Physics*, 69(2):137–154, 2001.

[31] K. M. Ho, C. T. Chan, and C. M. Soukoulis. Existence of a photonic gap in periodic dielectric structures. *Physical Review Letters*, 65(25):3152–3155, 1990.

[32] Z. Hou, F. Wu, and Y. Liu. Phononic crystals containing piezoelectric material. *Solid State Communications*, 130(11):745–749, 2004.

[33] Z. G. Huang and T. T. Wu. Temperature effect on bandgaps of surface and bulk acoustic waves in two-dimensional phononic crystals. *Ultrasonics, Ferroelectrics and Frequency Control, IEEE Transactions on*, 52(3):365–370, 2005.

[34] M. I. Hussein. Reduced Bloch mode expansion for periodic media band structure calculations. *Proceedings of the Royal Society A: Mathematical, Physical and Engineering Science*, 465(2109):2825–2848, 2009.

[35] J. H. Jang, C. Y. Koh, K. Bertoldi, M. C. Boyce, and E. L. Thomas. Combining pattern instability and shape-memory hysteresis for phononic switching. *Nano Letters*, 9(5):2113–2119, 2009.

[36] K. L. Jim, C. W. Leung, S. T. Lau, S. H. Choy, and H. L. W. Chan. Thermal tuning of phononic bandstructure in ferroelectric ceramic/epoxy phononic crystal. *Applied Physics Letters*, 94(19):3501–3503, 2009.

[37] J. Joannopoulos, S. Johnson, J. Winn, and R. Meade. *Photonic crystals: Molding the flow of light*. Princeton University Press, 2008.

[38] E. I. Jury. *Theory and application of the z-transform method*. New York: Wiley, 1964.

[39] A. Karlsson and K. Kreider. Transient electromagnetic wave propagation in transverse periodic media. *Wave Motion*, 23(3):259–277, 1996.

[40] A. Karlsson and R. Stewart. Wave propagators for transient waves in periodic media. *Journal of the Optical Society of America A: Optics Image Science and Vision*, 12(7):1513–1521, 1995.

[41] P. Kayestha. Time-harmonic wave propagation in pre-stressed compressible elastic bi-material laminate. *European Journal of Mechanics A: Solids*, 29(2):143–151, 2010.

[42] A. Khelif. Two-dimensional phononic crystal with tunable narrow pass band: Application to a waveguide with selective frequency. *Journal of Applied Physics*, 94(3):1308–1311, 2003.

[43] H. Kitzerow. Tunable photonic crystals. *Liquid Crystals Today*, 11(4):3–7, 2002.

[44] D. Krishnan and H. T. Johnson. Optical properties of two-dimensional polymer photonic crystals after deformation-induced pattern transformations. *Journal of the Mechanics and Physics of Solids*, 57(9):1500–1513, 2009.

[45] R. de L. Kronig and W. G. Penney. Quantum mechanics of electrons in crystal lattices. *Proceedings of the Royal Society A: Mathematical, Physical and Engineering Science*, 130(814):499–513, 1931.

[46] M. S. Kushwaha. Classic band structure of periodic elastic composites. *International Journal of Modern Physics B*, 10(9):977–1094, 1996.

[47] M. S. Kushwaha, P. Halevi, and G. Martinez. Theory of acoustic band structure of periodic elastic composites. *Physical Review B: Condensed Matter and Materials Physics*, 49(4):2313–2322, 1994.

[48] H. Levine. Reflection and transmission by layered periodic structures. *Quarlterly Journal of Mechanics and Applied Mathematics*, 14(1):107–122, 1966.

[49] M. Levinson and I. Burgess. A comparison of some simple constitutive relations for slightly compressible rubber-like materials. *International Journal of Mechanical Sciences*, 13(6):563–572, 1971.

[50] X. Li, F. Wu, H. Hu, S. Zhong, and Y. Liu. Large acoustic band gaps created by rotating square rods in two-dimensional periodic composites. *Journal of Physics D: Applied Physics*, 36(1):15–17, 2003.

[51] Z. Li and J. Lambros. Determination of the dynamic response of brittle composites by the use of the split hopkinson pressure bar. *Composites Science and Technology*, 59(7):1097–1107, 1999.

[52] S. C. S. Lin and T. J. Huang. Tunable phononic crystals with anisotropic inclusions. *Physical Review B: Condensed Matter and Materials Physics*, 83(17):4303–4312, 2011.

[53] M. Maldovan and E. L. Thomas. Simultaneous complete elastic and electromagnetic band gaps in periodic structures. *Applied Physics B: Lasers and Optics*, 83:595–600, 2006.

[54] P. Martin. N masses on an infinite string and related one-dimensional scattering problems. *Wave Motion*, 51(2):296–307, 2014.

[55] O. B. Matar, J. F. Robillard, J. O. Vasseur, A. C. Hladky-Hennion, P. A. Deymier, P. Pernod, and V. Preobrazhensky. Band gap tunability of magneto-elastic phononic crystal. *Journal of Applied Physics*, 111(5):4901–4915, 2012.

[56] A. Maurel, P. Martin, and V. Pagneux. Effective propagation in a one-dimensional perturbed periodic structure: comparison of several approaches. *Waves in Random and Complex Media*, 20(4):634–655, 2010.

[57] J. Miklowitz. *The theory of elastic waves and waveguides*. Elsevier, 1984.

[58] A. B. Movchan, N. V. Movchan, and R. C. McPhedran. Blochfloquet bending waves in perforated thin plates. *Proceedings of the Royal Society A: Mathematical, Physical and Engineering Science*, 463(2086):2505–2518, 2007.

[59] T. Mullin, S. Deschanel, K. Bertoldi, and M. C. Boyce. Pattern transformation triggered by deformation. *Physical Review Letters*, 99(8):4301–4304, 2007.

[60] B. Noble. *Methods based on the Wiener-Hopf technique for the solution of partial differential equations*. Chelsea, 1988.

[61] R. W. Ogden. *Non-linear elastic deformations*. Dover, 1998.

[62] C. Oh and M. J. Escuti. Time-domain analysis of periodic anisotropic media at oblique incidence: an efficient FDTD implementation. *Optics Express*, 14(24):11870–11884, 2006.

[63] U. Oseguera. Classical Kronig-Penney model. *American Journal of Physics*, 60(2):127–130, 1992.

[64] G. Ottarsson and P. Christophe. Vibration and wave localization in a nearly periodic beaded string. *The Journal of the Acoustical Society of America*, 101(6):3430–3442, 1997.

[65] W. J. Parnell. Effective wave propagation in a prestressed nonlinear elastic composite bar. *Journal of Applied Maths*, 72(2):223–244, 2007.

[66] W. J. Parnell. Nonlinear pre-stress for cloaking from antiplane elastic waves. *Proceedings of the Royal Society A: Mathematical, Physical and Engineering Science*, 468(2138):563–580, 2012.

[67] W. J. Parnell and I. D. Abrahams. Scattering from a cylindrical void in a pre-stressed incompressible neo-hookean material. *Communications in Computational Physics*, 11(2):367–382, 2012.

[68] W. J. Parnell, A. Norris, and T. Shearer. Employing pre-stress to generate finite cloaks for antiplane elastic waves. *Applied Physics Letters*, 100(17):1907–1907, 2012.

[69] Y. Pennec, B. Djafari-Rouhani, J. O. Vasseur, A. Khelif, and P. A. Deymier. Tunable filtering and demultiplexing in phononic crystals with hollow cylinders. *Physical Review E: Statistical, Nonlinear and Soft Matter Physics*, 69(4):6608–6613, 2004.

[70] O. Richoux, C. Depollier, and J. Hardy. Propagation of mechanical waves in a one-dimensional nonlinear disordered lattice. *Physical Review E: Statistical, Nonlinear and Soft Matter Physics*, 73(2):6611–6621, 2006.

[71] J. F. Robillard, O. Bou Matar, J. O. Vasseur, P. A. Deymier, M. Stippinger, A. C. Hladky-Hennion, Y. Pennec, and B. Djafari-Rouhani. Tunable magnetoelastic phononic crystals. *Applied Physics Letters*, 95(12):4104–4106, 2009.

[72] G. A. Rogerson and K. J. Sandiford. The effect of finite primary deformations on harmonic waves in layered elastic media. *International Journal of Solids and Structures*, 37(14):2059–2087, 2000.

[73] C. Rorres. Transmission coefficients and eigenvalues of a finite one-dimensional crystal. *SIAM Journal on Applied Mathematics*, 27(2):303–321, 1974.

[74] J. Sajeev. Strong localization of photons in certain disordered dielectric superlattices. *Physical Review Letters*, 58(23):2486–2489, 1987.

[75] A. Sato, Y. Pennec, N. Shingne, T. Thurn-Albrecht, W. Knoll, M. Steinhard, B. Djafari-Rouhani, and G. Fytas. Tuning and switching the hypersonic phononic properties of elastic impedance constrast nanocomposites. *ACS Nano*, 4(6):3471–3481, 2010.

[76] T. Shearer. *Waves in nonlinear elastic media with inhomogeneous pre-stress*. PhD thesis, University of Manchester, 2012.

[77] T. Shearer, I. D. Abrahams, W. J. Parnell, and C. H. Darios. Torsional wave propagation in a pre-stressed hyperelastic annular circular cylindere. *The Quarterly Journal of Mechanics and Applied Mathematics*, 66(4):465–487, 2013.

[78] G. Shmuel. Electrostatically tunable band gaps in finitely extensible dielectric elastomer fiber composites. *International Journal of Solids and Structures*, 50(5):680–686, 2013.

[79] G. Shmuel and G. deBotton. Band-gaps in electrostatically controlled dielectric laminates subjected to incremental shear motions. *Journal of the Mechanics and Physics of Solids*, 60(11):1970–1981, 2012.

[80] M. Sigalas. Elastic wave band gaps and defect states in two-dimensional composites. *The Journal of the Acoustical Society of America*, 101(3):1256–1261, 1997.

[81] M. Sigalas and E. N. Economou. Band structure of elastic waves in two dimensional systems. *Solid State Communications*, 86(3):141–143, 1993.

[82] T. Suzuki and P. K. Yu. Complex elastic wave band structures in three-dimensional periodic elastic media. *Journal of the Mechanics and Physics of Solids*, 46(1):115–138, 1998.

[83] E. C. Titchmarsh. *Theory of Functions*. Oxford University Press, 1939.

[84] N. Tymis and I. Thompson. Scattering by a semi-infinite lattice and the excitation of Bloch waves. *The Quarterly Journal of Mechanics and Applied Mathematics*, 67(3):469–503, 2014.

[85] J. O. Vasseur, P. A. Deymier, B. Djafari-Rouhani, Y. Pennec, and A. C. Hladky-Hennion. Absolute forbidden bands and waveguiding in two-dimensional phononic crystal plates. *Physical Review B: Condensed Matter and Materials Physics*, 77(8):5415–5429, 2008.

[86] J. O. Vasseur, B. Djafari-Rouhani, L. Dobrzynski, M. S. Kushwaha, and P. Halevi. Complete acoustic band gaps in periodic fibre reinforced composite materials: the carbon/epoxy composite and some metallic systems. *Journal of physics: condensed matter*, 6(42):8759–8770, 1994.

[87] J. P. Vasseur, O. B. Matar, J. F. Robillard, A. C. Hladky-Hennion, and P. A. Deymier. Band structures tunability of bulk 2D phononic crystals made of magneto-elastic materials. *AIP advances*, 1(4):1904–1916, 2011.

[88] J. O. Vassuer, P. A. Deymier, G. Frantziskonis, F. Hong, B. Djafari-Rouhani, and L. Dobrzynski. Experimental evidence for the existence of absolute acoustic band gaps in two-dimensional periodic composite media. *Journal of Physics: Condensed Matter*, 10(27):6051–6064, 1998.

[89] E. G. Vedenova, L. I. Manevich, and V. N. Pilipchuk. Normal oscillations of a string with concentrated masses on non-linearly elastic supports. *Journal of Applied Mathematics and Mechanics*, 49(2):153–159, 1985.

[90] M. E. Veysoglu, R. T. Shin, and J. A. Kong. A finite-difference time-domain analysis of wave scattering from periodic surfaces: Oblique incidence case. *Journal of Electromagnetic Waves and Applications*, 7(12):1595–1607, 1993.

[91] L. Wang and K. Bertoldi. Mechanically tunable phononic band gaps in three-dimensional periodic elastomer structures. *International Journal of Solids and Structures*, 49(19):2881–2885, 2012.

[92] X. H. Wang, B. Y. Gu, Z. Y. Li, and G. Z. Yang. Large absolute photonic band gaps created by rotating noncircular rods in two-dimensional lattices. *Physical Review B: Condensed Matter and Materials Physics*, 60(16):11417–11421, 1999.

[93] F. Wu, Z. Liu, and Y. Liu. Acoustic band gaps created by rotating square rods in a two-dimensional lattice. *Physical Review E: Statistical, Nonlinear and Soft Matter Physics*, 66(4):6628–4632, 2002.

[94] L. Y. Wu, M. L. Wu, and L. W. Chen. The narrow pass band filter of tunable 1D phononic crystals with a dielectric elastomer layer. *Smart Materials and Structures*, 18(1):5011–5019, 2009.

[95] L. Y. Wu, W. P. Yang, and L. W. Chen. The thermal effects on the negative refraction of sonic crystals. *Physics letters A*, 372(15):2701–2705, 2008.

[96] E. Yablonovitch. Inhibited spontaneous emission in solid-state physics and electronics. *Physical Review Letters*, 58(20):2059–2062, 1987.

[97] J. Y. Yeh. Control analysis of the tunable phononic crystal with electrorheological material. *Physica B: Condensed Matter*, 400(1):137–144, 2007.

[98] J. Y. Yeh and L. W. Chen. Wave propagations of a periodic sandwich beam by FEM and the transfer matrix method. *Composite Structures*, 73(1):53–60, 2006.

[99] X. Zhou and C. Chen. Tuning the locally resonant phononic band structures of two-dimensional periodic electroactive composites. *Physica B: Condensed Matter*, 431(1):23–31, 2013.

[100] X. Y. Zou, Q. Chen, B. Liang, and J. C. Cheng. Control of the elastic wave bandgaps in two-dimensional piezoelectric periodic structures. *Smart Materials and Structures*, 17(1):5008–5012, 2008.